

NASA-CR-191365

IN-46-CR

134001

P-86

**Meso-Beta Scale Numerical Simulation Studies of Terrain-Induced Jet Streak Mass/Momentum Perturbations**

*FY92 November Semi-Annual Report*

*submitted to the  
Mesoscale Processes Research Program  
Atmospheric Dynamics and Radiation Branch  
Earth Science and Application Division  
Office of Space Science and Applications  
NASA Headquarters  
Washington, D. C. 20546  
Attention: Dr. Ramish Kakar, Program Manager*

N93-13719

Unclas

G3/46 0134001

*by*

***Yuh-Lang Lin and Michael L. Kaplan***  
Department of Marine, Earth and Atmospheric Sciences  
North Carolina State University  
Raleigh, North Carolina 27695-8208  
(919) 515-7977

(NASA-CR-191365) MESO-BETA SCALE  
NUMERICAL SIMULATION STUDIES OF  
TERRAIN-INDUCED JET STREAK  
MASS/MOMENTUM PERTURBATIONS  
Semiannual Report, Nov. 1992  
(North Carolina State Univ.) 86 p

November 1992

## Table of Contents

### Part I. 3-D Numerical Modeling of Terrain-Induced Circulations

a) Simulated Background Synoptic and Meso- $\alpha$ Scale Jet Streak Adjustments Prior to the Development of Meso- $\beta$ Scale Features.....	1
b) Meso- $\beta$ Scale Adjustments Accompanying the Control Simulation During Observed Gravity Wave Episode I.....	4
c) Meso- $\beta$ Scale Adjustments Caused by Orographic Circulation Accompanying the Control Simulation During Observed Gravity Wave Episode II.....	6
d) Characteristics of Internal Gravity Waves in the Control Simulation During the Later Stages of Observed Gravity Wave Episode II.....	7
e) Summary, Conclusions, and FY93 Plans.....	8

### Part II. Linear Theory and Theoretical Modeling

a) Summary of Theoretical and Modeling Work to Date.....	11
b) Proposed Research (FY 1993).....	12

<b>References</b> .....	13
<b>List of Figures</b> .....	15

## Part I. 3-D Numerical Modeling of Terrain-Induced Circulations

The first numerical experiment which was performed on the North Carolina Supercomputer Center's CRAY-YMP machine during the second half of FY92 involved a 36 hour simulation of the CCOPE case study. This first "coarse-mesh" simulation employed the GMASS model (Whitaker et al. 1988) with a 178 x 108 x 32 matrix of grid points spaced approximately 24 km apart. The initial data was comprised of the global 2.5 x 2.5 degree analyses as well as all available North American rawinsonde data valid at 0000 UTC 11 July 1981. Highly-smoothed LFM-derived terrain data were utilized so as to determine the mesoscale response of the three-dimensional atmosphere to weak terrain forcing prior to including the observed highly complex terrain of the northern Rocky Mountain region (note Fig. 1). It was felt that the model should be run with a spectrum of terrain geometries, ranging from observed complex terrain to no terrain at all, to determine how crucial said terrain was in forcing the mesoscale phenomena observed by Koch and Golus (1988), Koch et al. (1988), and Koch and Dorian (1988). Both convection and stratiform (stable) precipitation were not allowed in this simulation so that their relative importance could be determined by inclusion in forth-coming simulations. A full suite of planetary boundary layer forcing was allowed in the simulation, including surface sensible and latent heat fluxes employing the Blakadar PBL formulation.

In the following sections of this report we will describe the details of this simulation, which, in many ways could be considered the *control* simulation, including the important synoptic-scale, meso- $\alpha$  scale, and meso- $\beta$  scale circulations. These results will be compared to the observations diagnosed by Koch and his colleagues as well as hypotheses set forth in the project proposal for terrain-influences upon the jet stream and their role in the generation of mesoscale wave phenomenon. The *fundamental goal* of the analyses *being the discrimination among background geostrophic adjustment, terrain influences, and shearing instability in the initiation and maintainance of mesoscale internal wave phenomena*. Based upon these findings, FY93 plans will be discussed.

### a) Simulated Background Synoptic and Meso- $\alpha$ Scale Jet Streak Adjustments Prior to the Development of Meso- $\beta$ Scale Features

At the initial time, i. e., 0000 UTC 11 July 1981, the 30 kPa and 50 kPa height and wind fields contained a deep low pressure trough oriented northeast-southwest off the west coast of the U. S. with a closed low centered just west of Seattle, Washington, as can be seen depicted in Figure 2. A massive ridge of high pressure exists over the high plains region of the U. S. with a

northeast-southwest oriented jet stream between northern California and Manitoba, Canada. The breakdown of the wind field into its constituent components indicates that there are two u-component maxima, one centered over southern Oregon and a second over eastern Manitoba as well as western Ontario and one v-component maxima over western Idaho. These fields indicate that Montana lies in the right front exit region of the jet streak extending from west of California to western Saskatchewan.

After 12 hours of simulation, i. e., by 1200 UTC 11 July 1981, there are three major changes to the mass and momentum field accompanying the aforementioned jet streak which can be discerned by comparing Figures 2 and 3. First, the height field values have dropped slightly in magnitude over northern Idaho and northeastern Washington while maintaining their magnitude to the south and southeast resulting in an increased northwestward-directed pressure gradient force over most of Idaho and Montana. Second, in response to this change in the height field, the v-component has increased in magnitude north and northeast of its 0000 UTC location, i. e., over most of Idaho, central and western Montana, and northwestern Wyoming. Third, the distinct u-component velocity maximum centered over southern Oregon at 0000 UTC has become absorbed into the maximum over southern Manitoba indicating a general increase in u-component magnitude between central Idaho and Saskatchewan.

These subtle changes in the 30 kPa jet streak clearly indicate that there is not a distinct propagation of the streak northeastwards during this first 12 hour period but a reorganization of its structure as: 1) the increased northwestward-directed pressure gradient force accelerates the v-component west of CCOPE by  $4-8 \text{ ms}^{-1}$  and 2) the Coriolis force changes in response to 1), thus increasing the u-component magnitude by  $2-3 \text{ ms}^{-1}$  over the same region. These adjustments have modified the 30 kPa jet structure in a manner wherein the shears just west of CCOPE are now directed primarily along-stream as opposed to across-stream even though CCOPE lies generally in the jet's right exit region with respect to the v-component and right entrance region with respect to the u-component.

When one compares this *control* simulation to the objective analyses of observations presented in Koch and Dorian (1988), one sees important similarities and important discrepancies. The simulation is similar to the extent that the model produces the localized 30 kPa southerly wind component maximum centered on western Idaho with maximum total wind velocity values  $\sim 50 \text{ ms}^{-1}$ . Furthermore, there is every indication that the simulated wind vectors are oriented across the geostrophic stream with the ageostrophic vector pointing to the northwest as observed, although the magnitude of the cross-stream ageostrophic component is not certain as we have not yet calculated its precise value. This v-component mesoscale maximum decreases over a short distance to the north of CCOPE where the westerly component becomes dominant. Comparison of total wind velocity and direction calculations between the model and the

observations indicates an excellent agreement between both sets of data. However, the simulated height field over northern Idaho and northeastern Washington is 10-30 m too high, and there is little indication of the short wave trough (A) along the spine of the Rocky Mountains between Idaho and Montana as diagnosed from the observations. Interestingly, the simulation does indicate the development of a weak cold trough to the west of this mountain range and warm ridge to its east by 1200 UTC. This thermal feature did become better organized as it propagated from Oregon to Montana. However, it is not clear if its intensification is the result of the larger scale frontogenetical adjustments or local weak terrain-induced forcing between Idaho and Montana. The 30 kPa vertical motions at 1200 UTC, depicted in Figure 4, clearly indicate rising motion within the warm Laplacian configuration indicating a thermally-direct circulation which would be frontolytic, although increasing ageostrophic confluence may be acting to enhance frontogenesis in this region. Below 30 kPa the vertical motion is positive indicating sinking and a thermally-indirect circulation as can be seen in Figure 4.

Given these similarities and differences one could come to the following general conclusions of the upper-tropospheric dynamical processes between 0000 UTC and 1200 UTC based upon the smoothed terrain *control* simulation and the observations. First, the development of the mesoscale southerly ageostrophic wind maximum over Idaho southwest of CCOPE is largely *independent* of a distinct propagating upstream wave or mesoscale terrain influences, as it is well-simulated without the influence of either. This feature is similar to the diagnosed unbalanced region wherein a strong cross-stream ageostrophic wind component was observed by Koch and Dorian (1988). This feature *evolves locally*, i.e., it is not advected into this region. Second, said ageostrophic feature does produce a geostrophic adjustment by forcing a weak acceleration of the u-component downstream to the northwest of CCOPE. However, this adjustment is, *at 30 kPa*, a slow-manifold (Coriolis) response which apparently is incapable of triggering any internal gravity waves at this time. It also is a local adjustment not advected into this region. Third, the existence of a short wave trough (A) (as diagnosed by Koch) lying astride the Rocky Mountains between Idaho and Montana is not likely the result of larger scale frontogenetical processes and *may* be the result of local terrain-induced forcing. The first two conclusions, which are strongly supported by the simulation, indicate jet streak adjustment, not propagation, in spite of the fact that there is no indication of gravity wave formation at this point in the simulation! The third conclusion about the formation of feature "A" and its subsequent importance is considerably less certain and will await additional simulations before we can feel confident about our analyses. Furthermore, it should be reiterated that the sign of the vertical motion changes between 30 kPa and 50 kPa, indicating some vertical variation in the magnitude and pattern of the aforementioned adjustments.

## b) Meso- $\beta$ Scale Adjustments Accompanying the Control Simulation During Observed Gravity Wave Episode I

Koch et al.'s (1988) paper clearly indicates that mesoscale waves R1, R2, RU, and R3 are observed to develop over southwestern Montana during the first episode period prior to 1800 UTC. A close examination of the 30 kPa omega fields in Figure 5 for the period after 1200 UTC extending to 1800 UTC shows continued weak ascent over central and eastern Montana with little indication of the contraction in scale to distinct propagating meso- $\beta$  scale vertical motion maxima typical of internal gravity waves. However, a comparison with the same fields at the 50 kPa level depicted in Figure 5 indicates a definite scale contraction and some indication of multiple propagating maxima. The first 50 kPa ascent feature develops over west-central Montana at hour 13. This feature propagates eastward and then bifurcates into a second feature just west of the CCOPE network by hour 17. The wavelength of these two features ( $\sim 200$  km) and their speed of propagation ( $\sim 20$  ms $^{-1}$ ) are not dissimilar to the primary modes described by Koch et al. However, there is little indication of definite amplification of these modes into distinct pressure perturbations in the simulated model cross sections (note Figure 6) or mean sea level pressure fields (not shown). These features are also evident in the 70 kPa omega fields (not shown) being more numerous and having a somewhat shorter wavelength than at 50 kPa.

While these features are very weak, their genesis, particularly at 50 kPa, is most relevant. There are subtle differences in the geometry of the simulated 30 kPa and 50 kPa wind and height fields during the 1200 UTC - 1800 UTC period. A comparison between Figures 3 and 7 indicates that at the 50 kPa level the amplitude of the height ridge is slightly greater over eastern Montana than at 30 kPa, hence, the spatial variation of the pressure gradient force is larger. Furthermore, the spatial variation of the u-component over this same region at 50 kPa, i. e., the gradient of u-component oriented towards CCOPE *orthogonal* to the southwest-northeast stream, is clearly greater than at 30 kPa. Hence, it is not surprising that the adjustment of the u-component to the increase in the v-component upstream over Idaho and southwestern Montana is stronger at 50 kPa producing a definite velocity convergence maximum dominated by the cross-stream shear (*oriented towards the southeast*) of the u-component velocity over central Montana which propagates downstream over the CCOPE network by 1800 UTC. Another way of expressing this is that as the v-component increased between 0000 UTC and 1200 UTC, the divergence tendencies orthogonal to this component increased within a region of the fluid wherein geostrophic adjustment was maximized, i. e., wherein the Laplacian of pressure, the Jacobian of u and v, as well as the  $f\zeta$  term within the nonlinear balance equation, were all sufficiently different in magnitude so as not to compensate for one another (Kaplan and Paine 1977; Uccellini and Koch 1987; Zack and Kaplan 1987). Expressed in a yet different manner: in

an effort to increase the u-component towards its appropriate geostrophic value as the v-component increases, mass is being transported orthogonal to the larger scale stream; i. e., to the southeast of the jet. There is some indication from the analysis of Koch and Dorian (1988) at 1200 UTC that the 30 kPa wind field over western and central Montana crosses to the right of the height field supporting the concept of a downstream transport of mass during geostrophic adjustment.

It is most interesting, also, that this increased horizontal imbalance at 50 kPa relative to 30 kPa is occurring beneath the level of most significant vertical increase of the horizontal wind velocity and the Brunt-Vaisala frequency, as well as the critical level where the wind velocity in the direction of wave propagation is equivalent to the observed wave propagation velocity as described in Koch and Dorian (1988) (note cross sections in Figure 6). Hence, the weak mesoscale geostrophic adjustment processes simulated by the GMASS model tend to be stronger between the boundary layer, i. e., the layer between 85 kPa and 70 kPa, and 50 kPa than they are at 30 kPa.

It should be cautioned that the above conclusions are predicated upon preliminary "back of the envelope" calculations. Further in-depth diagnostics are still required, which will be performed in the future. However, these preliminary findings indicate that the geostrophic adjustment process is likely stronger near the 50 kPa level than at 30 kPa over west - central Montana. Based upon this single *control* simulation, it is not clear why these mesoscale velocity divergence maxima do not amplify into distinct propagating internal gravity waves as were observed over CCOPE. One could speculate that either mesoscale terrain forcing accompanying the development of disturbance "A" or the development of convection selectively increased the amplitude of the adjustment process. Perhaps the relatively coarse model horizontal resolution inhibited nonlinear wave amplification? Perhaps a combination of these processes is responsible? It should be noted that both Lagrangian Rossby number (Koch and Dorian 1988) and inertial-advective Rossby number (Uccellini et al. 1984) calculations were performed using simulated 50 kPa values over the region just upstream from CCOPE during the 1400 UTC to 1500 UTC period. The Lagrangian and inertial-advective  $Ro$  values of  $\sim .15$  and  $\sim .33$ , respectively, indicate that while the flow may have been unbalanced from the perspective of the divergence equation, the weak accelerations accompanying these low  $Ro$  values would suggest flow that was still not sufficiently close to  $Ro \sim 1.0$ , which is typically used as a criterion for a strongly unbalanced regime. Possible answers to this question of why gravity waves were not simulated in this region may be forthcoming after additional simulations. Nevertheless, there clearly is an indication that a geostrophic adjustment process does occur between 1200 UTC and 1800 UTC just upstream from CCOPE which spatially corresponds to the observed initiation of

mesoscale velocity divergence maxima. These features are most strongly forced within the 50 - 70 kPa layer.

### c) Meso- $\beta$ Scale Adjustments Caused by Orogenic Circulation Accompanying the Control Simulation During Observed Gravity Wave Episode II

Koch et al. (1988) describe the observed gravity waves during CCOPE as being clustered during two episodes with a relatively short lull inbetween. The GMASS *control* simulation indicates that shortly after the aforementioned geostrophic adjustment process, i. e., between 1800 UTC 11 July and 0000 UTC 12 July, an orogenically-forced circulation develops over the smoothed mountains along the Idaho-Montana border. Tripoli and Cotton (1989a,b) define "orogenic" as a "convective weather system that is excited by orographic flow systems but becomes self-sustaining". The driving mechanism for this circulation is similar to that described by Koch (1985) and Tripoli and Cotton (1989a,b) in which the deepening PBL over the elevated terrain produces a solenoidally-forced and thermally-direct circulation wherein heated air over the elevated plateau becomes warmer *at the same elevation* than air directly downstream above the valley as a result of differential surface sensible heat fluxes. One can graphically see in Figure 8 just how much the PBL has expanded over the western sector of the cross section at its apex, i. e., 0000 UTC 12 July, which is 1800 MDT. Here, a deep dry adiabatic layer has been simulated to nearly 50 kPa with the 316 K isentrope extending from near 55 kPa to the surface, ~ 80 kPa. This has the effect of reversing the mountain-valley temperature gradient which was, at 1800 UTC, oriented from valley to mountain. Hence, the elevated plateau becomes a "heat island" and the ensuing thermally-direct circulation is established by 0000 UTC 12 July.

This deepening PBL effectively warms a layer ~ 20 kPa thick by more than 2 K. The effect upon the midtropospheric mass field of this process can be discerned from Figure 9 wherein the 50 kPa height, temperature, omega, u-component, and v-component as well as the 30 kPa u-component and v-component are depicted during the 1900 UTC to 0000 UTC period. Height rises of nearly 10 m above the narrow diabatically-forced warm tongue by 2100 UTC modify the along-stream pressure gradient force resulting in an accelerating wind field in a stream-wise sense. The velocity divergence and convergence patterns forced by the differential accelerations result in a northwest-southeast oriented pattern of rising, sinking, and rising motions extending from above the leeside of the elevated plateau to just west of CCOPE by 2100 UTC. By 0000 UTC, the second downstream rising cell of this thermally-indirect along-stream frontogenetical circulation is positioned over the western part of CCOPE. The structure and amplitude of this feature is analogous to the 50 kPa thermal perturbation observed by Koch and Dorian (1988) at 0000 UTC 12 July. Accompanying this feature are mesoscale u-component



and v-component maxima which slope upstream between 50 kPa and 30 kPa over east-central and west-central Montana, respectively. If this feature is, indeed, analogous to the feature observed by Koch and Dorian (1988), it would explain the mass perturbation which they observe approaching CCOPE as feature "A" at 0000 UTC 12 July and the momentum perturbation accompanying feature "B" over western Montana at the same time. Feature "B" is accompanied by a northeastward "streamwise" extension of the jet at 30 kPa in the observed data which is replicated as a mesoscale maximum of u and v-component wind velocity over west-central Montana.

The orogenically-forced circulations, while being the strongest ageostrophic features simulated at this point, still do not appear to have characteristics similar to the episode II gravity waves observed by Koch et al. (1988). Their wavelength is  $\sim 400$  km and phase velocity  $\sim 10$ - $15$   $\text{ms}^{-1}$  which differs substantially from the primary modes. However, Lagrangian and inertial-advective Rossby number computations indicate larger unbalanced flow regimes than the aforementioned geostrophic adjustment processes discussed in the previous subsections. Calculations performed within the largest acceleration region at 50 kPa over west-central Montana at 2100 UTC indicate Lagrangian  $Ro$  values  $\sim .29$  and inertial-advective  $Ro$  values  $\sim .42$ . These should be compared with values  $\sim .15$  and  $.33$ , respectively, for the weak geostrophic adjustment process described in the previous subsection which was simulated to occur between 1200 UTC and 1800 UTC. Hence, the orogenic circulation is more unbalanced, but during its formative period, still unable to produce internal gravity wave phenomena. In spite of this, during this period between 1800 UTC and 0000 UTC, mid-upper tropospheric vertical motions approach and exceed  $10 \text{ cms}^{-1}$  resulting in substantial adiabatic cooling as was observed over CCOPE at 0000 UTC by Koch and Dorian (1988). Furthermore, there is every indication that the mass and momentum perturbations observed by Koch and Dorian (1988) over CCOPE and the region upstream above the mountains and termed short waves "A" and "B" are really mass and momentum perturbations, respectively, resulting from this orogenic circulation. The streamwise structure of these mesoscale along-stream ageostrophic fronts downstream from the mountains is analogous to the terrain-induced circulations described in Kaplan and Karyampudi (1992a,b).

#### **d) Characteristics of Internal Gravity Waves in the Control Simulation During the Later Stages of Observed Gravity Wave Episode II**

Shortly after 0000 UTC 12 July, an upstream-tilted internal gravity wave develops over west-central Montana within the downstream-propagating orogenic circulation. The wave crests can be seen in Figure 10 at  $\sim 55$  kPa and  $\sim 70$  kPa during the 0100 UTC to 1200 UTC period.

This wave is tilted a large distance upstream with  $\sim 200$  km separating the upper crest from the lower crest. The wavelength of each is  $\sim 300$  km and the average phase velocity of the upper mode is  $\sim 18$   $\text{ms}^{-1}$  and the lower mode  $\sim 16$   $\text{ms}^{-1}$ . The wavelength of each is nearly twice that of the average of the observed primary waves reported during CCOPE while the phase velocities are slightly slower than the averages of both modes. These waves do not propagate at constant phase velocities within the simulation, accelerating and decelerating several times during this 11 hour period. There is every indication that these are gravity waves based upon the deceleration patterns of the wind fields relative to the waves and the velocity convergence/divergence patterns which facilitate ascent ahead of the crests and descent behind the crests, hence, producing a quadrature relationship for the vertical motions as depicted in Koch and Golus (1988). These features propagate over and downstream of the CCOPE network between 0600 UTC and 1200 UTC 12 July. Furthermore, a second lower tropospheric mode develops near or slightly west of the location of the genesis point of the first mode at  $\sim 1000$  UTC. This feature propagates at a slower phase velocity than the first mode for the remaining two hours of the simulation, i. e.,  $\sim 13$   $\text{ms}^{-1}$ .

The genesis location and period of the first simulated wave correspond to the deformed height, temperature, wind, and omega patterns at 50 kPa and 30 kPa over southwest-central Montana at 0100 UTC - 0300 UTC depicted in Figure 11. While detailed divergence equation calculations have not been performed at this time, it is intuitively obvious that the meso- $\beta$  scale Laplacian in the height field in direct juxtaposition to very strong along-stream gradients in the wind field would produce significant total time tendency values of divergence and convergence. Crude 50 kPa Rossby number calculations at 0100 UTC 12 July at a point  $\sim 100$  km northeast of the northwest corner border location among Montana, Idaho, and Wyoming indicate values of  $\sim .42$  and  $\sim .66$  for the Lagrangian and inertial-advective  $R_o$ , respectively. The location of this region of maximum  $R_o$  values is consistent with the location of observed maximum calculated by Koch and Dorian (1988) employing a .75 degree lat/lon grid between northwestern Wyoming and southwest-central Montana. These values are considerably greater, albeit still  $< 1.0$ , than the .15 and .29 as well as the .33 and .42 for the Lagrangian  $R_o$  and inertial-advective  $R_o$ , respectively, at the two aforementioned earlier time periods, i. e.,  $\sim 1500$  UTC and 2100 UTC 11 July. This location is highly consistent with the observed wave genesis region reported by Koch et al. (1988) as well as the observed 30 kPa unbalanced region reported in Koch and Dorian (1988).

#### e) Summary, Conclusions, and FY93 Plans

The first of a series of simulations, which are designed to diagnose the role of terrain in producing observed mesoscale wave phenomena, have been described. The *control* simulation was performed with a 24 km version of the GMASS numerical model employing smoothed LFM terrain and no precipitation processes. This simulation recreated some of the observed meso- $\alpha$  and meso- $\beta$  scale phenomena which were diagnosed over the CCOPE observational network by Koch and Golus (1988), Koch et al. (1988), and Koch and Dorian (1988).

Four sets of key sequential adjustments were simulated. First, during the 0000 UTC - 1200 UTC period, the intensifying southeast-northwestward-directed pressure gradient force at the jet stream level, i. e., 30 kPa, produced an observed acceleration of the v wind velocity component maximum over Idaho, southwestern Montana, and northwestern Wyoming. This resulted in the amplification of the cross-stream component of the ageostrophic v-component which was observed by Koch and Dorian (1988) at 1200 UTC 11 July. In response to said amplification, the u wind velocity component increased over western and central Montana as the Coriolis force nudged the flow towards a slow geostrophic adjustment.

Second, the adjustment process described in the previous paragraph becomes better organized between 1200 UTC and 1800 UTC 11 July below the 30 kPa level, i. e., between 50 kPa and 70 kPa. Here, the variation of the horizontal pressure gradient force and horizontal wind shears are more conducive to the development of an increase in the velocity divergence/convergence patterns at the mesoscale just upstream of and over CCOPE. However, the subsequent scale contraction of divergence maxima and minima over CCOPE is not of sufficient magnitude to produce coherent internal gravity waves as were observed by Koch and Golus (1988). It is speculated that the reason for the model's inability to replicate said waves is probably a combination of the ultrasmoothness of the terrain and the relatively coarse resolution, both of which inhibit the development of the observed short wave trough "A" which aligned itself along the northwest-southeast mountain geometry. This feature may have contributed to the imbalance of forces downstream over Montana, thus resulting in stronger divergence tendencies.

Third, during the 1800 UTC and 0000 UTC period, the differential surface sensible heating between the elevated plateau of western Montana and the lower region of central Montana results in a thermally-direct mesoscale circulation. Accompanying this circulation are zones of vertical motion which slowly propagate downstream towards CCOPE. This feature produces a midtropospheric circulation which is analogous to observations over CCOPE at 0000 UTC 12 July. However, this circulation does not immediately produce distinct internal gravity wave phenomena.

Fourth, shortly after 0000 UTC 12 July, an upstream-tilted internal gravity wave develops over the southwest-central part of Montana in direct proximity to the largest mass and

momentum perturbations accompanying the orogenic circulation described in the previous paragraph. This wave coherently moves downstream over CCOPE and further away from its genesis location during the subsequent 10 hours of the simulation. The structure of the gravity wave indicates dual vertical levels of maximum amplitude, i. e., ~55 kPa and ~ 70 kPa with a large separation distance inbetween these maxima. The vertical structure of the wave is consistent with that dictated by gravity wave theory, and the average phase velocity of both vertical modes are similar to the modes observed over CCOPE. The horizontal wavelength of this feature is nearly twice as long as the primary mode observed over CCOPE, however. This gravity wave is generated within the orogenic circulation which contained highly unbalanced meso- $\beta$  scale mass and momentum perturbations. Later in the simulation, an additional gravity wave develops within the same region of southwestern Montana.

The fundamental conclusions to be derived from this first simulation involve the importance of the orogenic circulation in establishing the conditions for gravity wave genesis. While geostrophic adjustment processes were simulated by the numerical model in a region where observations indicated they probably existed in nature, these adjustments were of insufficient magnitude to induce gravity wave genesis. Only after several hours of continuous decoupling between the midtropospheric mass and momentum field accompanying the orogenic circulation did any distinct gravity wave phenomena develop in the simulation.

Plans for FY 93 are going to be focussed on the problem of how terrain structure acts to produce an environment conducive for gravity wave genesis. Simulations will be designed to diagnose the sensitivity of gravity wave genesis to terrain-induced midtropospheric mass-momentum perturbations. The priority list for additional simulations includes:

- 1) A 24 km simulation with no terrain at all,
- 2) A 24 km simulation with no surface sensible heat fluxes,
- 3) A 24 km simulation with observed mesoscale terrain and surface sensible heat fluxes,
- 4) A full physics nested-grid 8 km simulation which excludes precipitation processes, and
- 5) A full physics nested-grid 8 km simulation which includes precipitation processes.

It will probably require all of FY 93 and FY 94 to complete this effort. However, during FY 93 we can conclusively eliminate *background/nonterrain-induced* geostrophic adjustment as the prime forcing function for wave genesis by performing the first two simulations which are listed above. Furthermore, we can isolate the response of the gravity wave generation processes to higher resolution complex terrain by performing experiment 3). It is important to reiterate one of the major findings of the first year's effort, i.e., *that no gravity wave was triggered during observed wave episode I wherein there was every indication that short wave trough "A" was not simulated. Thus, the inability to simulate "A" at 1200 UTC, which was very likely a terrain-*

*induced mesoscale circulation, likely contributed to the absence of gravity waves during episode I. However, wave "A" and "B" at 0000 UTC, i.e., probably the orogenic circulation, was effective, even with unrealistically-smoothed terrain, in modifying the background atmosphere to produce gravity wave generation mechanisms during wave episode II.*

## **Part II. Linear Theory and Theoretical Modeling**

### **a) Summary of Theoretical and Modeling Work to Date**

To date, the majority of the theoretical work has focused on understanding the basic dynamics of the mechanism of geostrophic adjustment through an investigation of the initial value problem for two- and three-dimensional unbalanced, localized, ageostrophic zonal (east - west) wind perturbations in idealized analytical models of motionless homogeneous, and unbounded continuously stratified rotating planetary atmospheres. Linear theoretical results indicate that while inertia-gravity waves are generated for both types of physical systems, only the three - dimensional fluids are capable of asymptotic adjustment to a non-zero geostrophically balanced equilibrium wherein a significant fraction of the initial zonal ageostrophic wind perturbation is retained, since the introduction of an alongstream or zonal wind perturbation provides a non-zero initial potential vorticity state.

Recently, in a study closely related to our own, Fritts and Luo (1992) have published linear analytical solutions for the inertia-gravity waves generated by an initial ageostrophic zonal wind anomaly which is uniform in the alongstream direction (i.e. no alongstream shear is associated with the perturbation). While the solutions indicated that a non-zero geostrophically balanced initial state is eventually obtained, this model did not address the fundamental differences in the nature of the response due to the scale differences between the ageostrophic perturbation and the Rossby radius of deformation in the horizontal, as well as the scale differences between the perturbation and the deformation depth in the vertical. Both the horizontal and the vertical length scale of the ageostrophic initial state are important in the character of the geostrophic adjustment dynamics of a continuously stratified atmosphere. In addition, the neglect of the alongstream shear associated with the perturbation renders the model incapable of approximating a midlatitude jetstreak.

Luo and Fritts (1992) have considered the initial value problem for a fully three-dimensional localized ageostrophic zonal wind anomaly, which is a better approximation for investigating the inertia-gravity waves generated by midlatitude jetstreaks. While these results have yet to be published, we expect their results to agree well with our independent formulation

and solution of the three-dimensional initial value problem. These results will be published in a forthcoming doctoral dissertation.

The theoretical results to date have been used as sensitivity benchmarks in the development of a simple nonlinear, primitive equation mesoscale numerical model, whose main advantage over preexisting more sophisticated mesoscale models is the certainty with which the contribution from the nonlinear terms in the governing equations to the response can be determined, as well as the wide variability in the specification of idealized external forcings and/or initial states which do not rely on the complexities associated with assimilating real observational data. With the model development accomplished, it is possible to isolate and understand the nonlinear contribution to the geostrophic adjustment mechanism for both unbalanced ageostrophic and balanced geostrophic initial states, and how this mechanism is modified by orographic forcing. In addition, the thermally direct and indirect mesocirculations found in the entrance and exit regions of propagating midlatitude upper tropospheric jet streaks can only exist when the upstream geostrophically balanced jetstream flow passes through and exits the long-lived, quasi-steady slower propagating jet core. The relative importance of the generation and development of this circulation with respect to fundamental jetstreak geostrophic adjustment processes can be addressed within the context of theoretically oriented modeling simulations.

#### **b) Proposed Research (FY 1993)**

- Generalize the classical numerical results of Van Tuyl and Young (1982) by investigating the geostrophic adjustment dynamics associated with the propagation of a quasi-steady, quasi-balanced, upper level jet streak in a layer-sheared *continuously stratified* atmosphere.
- Generalize the character of the fundamental linear theoretical geostrophic adjustment dynamics associated with a fully three-dimensional localized, unbalanced, ageostrophic zonal wind anomaly in a continuously stratified atmosphere by analytically and numerically investigating the response with emphasis on the horizontal and vertical length scales of the jet streak with respect to the Rossby radius of deformation and vertical depth of deformation.
- Investigate the nonlinear contribution to the geostrophic adjustment mechanism for both unbalanced ageostrophic as well as linear geostrophically balanced initial states through theoretically oriented numerical modeling simulations.

- Investigate the effects of quasi-linear and nonlinear orographic forcing on a propagating, localized, three-dimensional, zonal wind anomaly in a continuously stratified atmosphere through theoretically oriented numerical modeling studies.
  
- Investigate the role played by jetstreak upper-level forcing in the initiation and development of both lee and coastal cyclogenesis through theoretically oriented modeling work. Guidelines for this part of the proposed research will be provided by the existing linear theories of Smith (1984, 1986) and Lin (1989, 1990) on lee and coastal cyclogenesis, respectively.

## References

- Fritts, D. C., and Z. Luo, 1992: Gravity wave excitation by geostrophic adjustment of the jet stream. Part I: Two-dimensional forcing. *J. Atmos. Sci.*, 49, 681-697.
- Kaplan, M. L., and D. A. Paine, 1977: The observed divergence of the horizontal velocity field and pressure gradient force at the mesoscale: Its implications for the parameterization of three-dimensional momentum transport in synoptic scale numerical models. *Beitr. Phys. Atmos.*, 50, 321-330.
- , and V. M. Karyampudi, 1992a: Meso-beta scale numerical simulations of terrain drag-induced along-stream circulations. Part I: Midtropospheric frontogenesis. In Press, *Meteor. Atmos. Phys.*
- , and -----, 1992b: Meso-beta scale numerical simulations of terrain drag-induced along-stream circulations. Part II: Concentration of potential vorticity within dryline bulges. In Press, *Meteor. Atmos. Phys.*
- Koch, S. E., W. C. Skillman, P. J. Kocin, P. J. Wetzel, K. F. Brill, D. A. Keyser, and M. C. McCumber, 1985: Synoptic scale forecast skill and systematic errors in the MASS 2.0 model. *Mon. Wea. Rev.*, 113, 1714-1737.

- , and R. E. Golus, 1988: A mesoscale gravity wave event observed during CCOPE. Part I: Multiscale statistical analysis of wave characteristics. *Mon. Wea. Rev.*, 116, 2527-2544.
- , R. E. Golus, and P. B. Dorian, 1988: A mesoscale gravity wave event observed during CCOPE. Part II: Interactions between mesoscale convective systems and the antecedent waves. *Mon. Wea. Rev.*, 116, 2545-2569.
- , and P. B. Dorian, 1988: A mesoscale gravity wave event observed during CCOPE. Part III: Wave environment and probable source mechanisms. *Mon. Wea. Rev.*, 116, 2570-2592.
- Lin, Y.-L., 1989: A theory of cyclogenesis forced by diabatic heating. Part I: A quasi-geostrophic approach. *J. Atmos. Sci.*, 46, 3015-3036.
- Lin, Y.-L., 1990: A theory of cyclogenesis forced by diabatic heating. Part II: A semigeostrophic approach. *J. Atmos. Sci.*, 47, 1755-1777.
- Luo, Z., and D. C. Fritts, 1992: Gravity wave excitation by geostrophic adjustment of the jet stream. Part II: Three-dimensional forcing. *J. Atmos. Sci.*, in press.
- Smith, R. B., 1984: A theory of lee cyclogenesis. *J. Atmos. Sci.*, 41, 1159-1168.
- Smith, R. B., 1986: Further development of a theory of lee cyclogenesis. *J. Atmos. Sci.*, 1582-1602.
- Tripoli, G. J., and W. R. Cotton, 1989a: Numerical study of an observed orogenic mesoscale convective system. Part 1: Simulated genesis and comparisons with observations. *Mon. Wea. Rev.*, 273-304.
- , and -----, 1989b: Numerical study of an observed orogenic mesoscale convective system. Part 2: Analysis of governing dynamics. *Mon. Wea. Rev.*, 305-328.
- Uccellini, L. W., and S. E. Koch, 1987: The synoptic setting and possible energy sources for mesoscale wave disturbances. *Mon. Wea. Rev.*, 115, 721-729.
- , P. J. Kocin, R. A. Petersen, C. H. Wash, and K. F. Brill, 1984: The Presidents' Day cyclone of 18-19 February 1979: Synoptic overview and analysis of subtropical jet streak influencing the pre-cyclogenetic period. *Mon. Wea. Rev.*, 112, 398-412.



- Van Tuyl, A. H. and J. A. Young, 1982: Numerical simulation of nonlinear jetstreak adjustment. *Mon. Wea. Rev.*, 110, 2038-2054.
- Whitaker, J. S., L. W. Uccellini, and K. F. Brill, 1988: A model-based diagnostic study of the rapid development phase of the Presidents' Day cyclone. *Mon. Wea. Rev.*, 116, 2337-2365.
- Zack, J. W., and M. L. Kaplan, 1987: Numerical simulations of the subsynoptic features associated with the AVE-SESAME I case. Part I: The preconvective environment. *Mon. Wea. Rev.*, 115, 2367-2394.

### List of Figures

Fig. 1: (a) Region of model integration with the region of the nested grid matrix and CCOPE highlighted within. (b) High resolution terrain data base (m) over the coarse mesh integration region. (c) Low resolution smoothed LFM terrain data base (m) employed for the *control simulation* over the coarse mesh integration region.

Fig. 2: NMC global analysis fields and rawinsonde observations employed to initialize the GMASS model at 0000 UTC 11 July 1981. (a) Observed u-component isotachs ( $\text{ms}^{-1}$ ) at 30 kPa and 50 kPa, (b) observed v-component isotachs ( $\text{ms}^{-1}$ ) at 30 kPa and 50 kPa. (c) Observed height (solid in m) and temperature (dashed in C) at 30 kPa and 50 kPa. (d) Observed cross sections of u-component isotachs and vectors ( $\text{ms}^{-1}$ ) and v-component isotachs and vectors ( $\text{ms}^{-1}$ ) between 45 N., 112 W. and 48 N. and 98 W.

Fig. 3: Simulated 30 kPa (a) height (solid in m) and temperature (dashed in C), (b) u-component isotachs ( $\text{ms}^{-1}$ ), and (c) v-component isotachs ( $\text{ms}^{-1}$ ) all valid at 1200 UTC 11 July 1981.

Fig. 4: Simulated vertical velocity (upward dashed in  $10^{-5} \text{ kPa s}^{-1}$ ) at (a) 30 kPa, (b) 50 kPa, and (c) 70 kPa all valid at 1200 UTC 11 July 1981.

Fig. 5: Simulated vertical velocity (upward dashed in  $10^{-5} \text{ kPa s}^{-1}$ ) at (a) 30 kPa and (b) 50 kPa and valid from 1300 UTC to 1800 UTC 11 July 1981.

Fig. 6: Cross sections of simulated total wind vectors ( $\text{ms}^{-1}$ ) and potential temperature (K) valid at (a) 1300 UTC, (b) 1400 UTC, (c) 1500 UTC, and (d) 1600 UTC 11 July 1981. Location is the same as in Figure 2d.

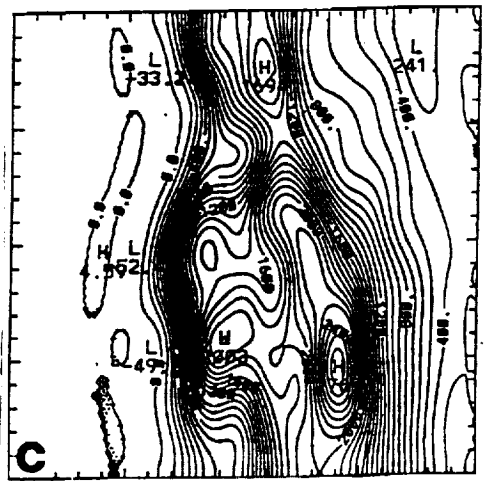
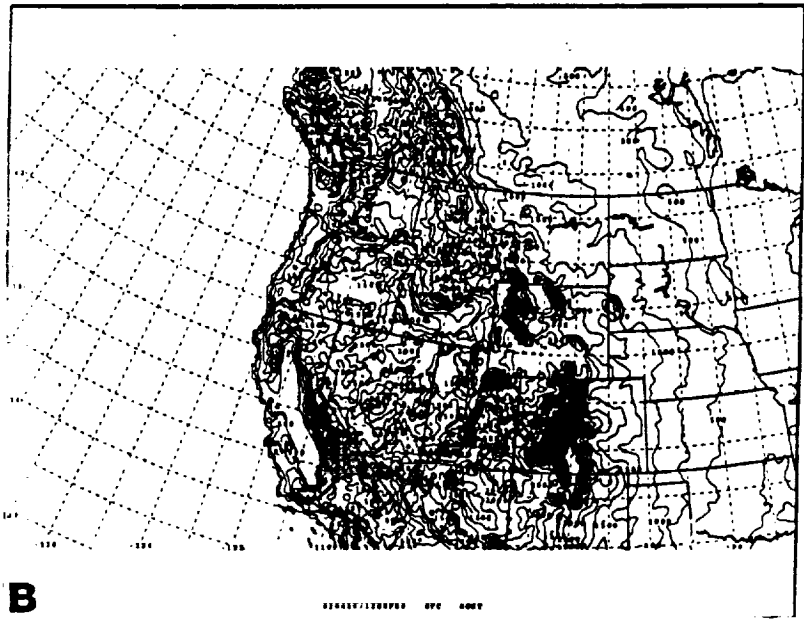
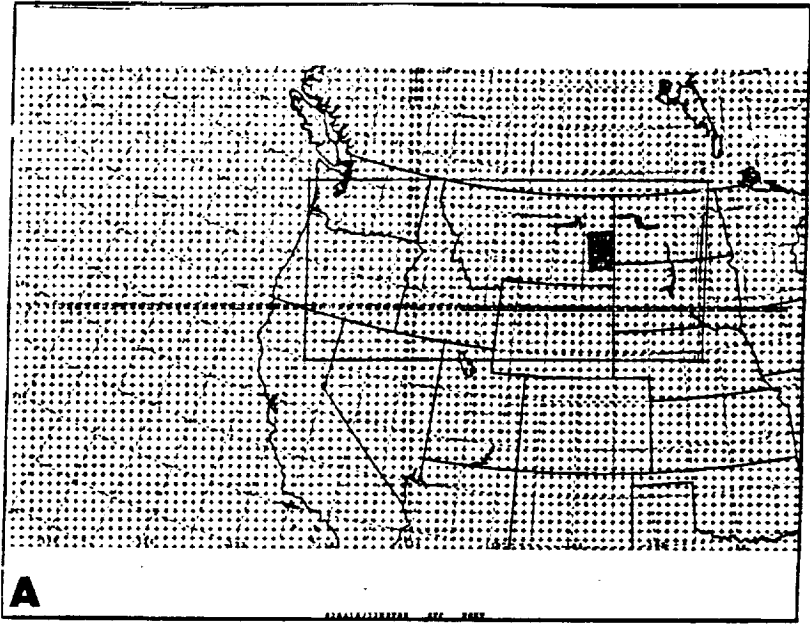
Fig. 7: Simulated (a) 30 kPa height (solid in m) and temperature (dashed in C), (b) 50 kPa height (solid in m) and temperature (dashed in C), (c) 30 kPa u-component isotachs ( $\text{ms}^{-1}$ ), (d) 30 kPa v-component isotachs ( $\text{ms}^{-1}$ ), (e) 50 kPa u-component isotachs ( $\text{ms}^{-1}$ ) and (f) 50 kPa v-component isotachs ( $\text{ms}^{-1}$ ) all valid between 1300 UTC and 1800 UTC 11 July 1981.

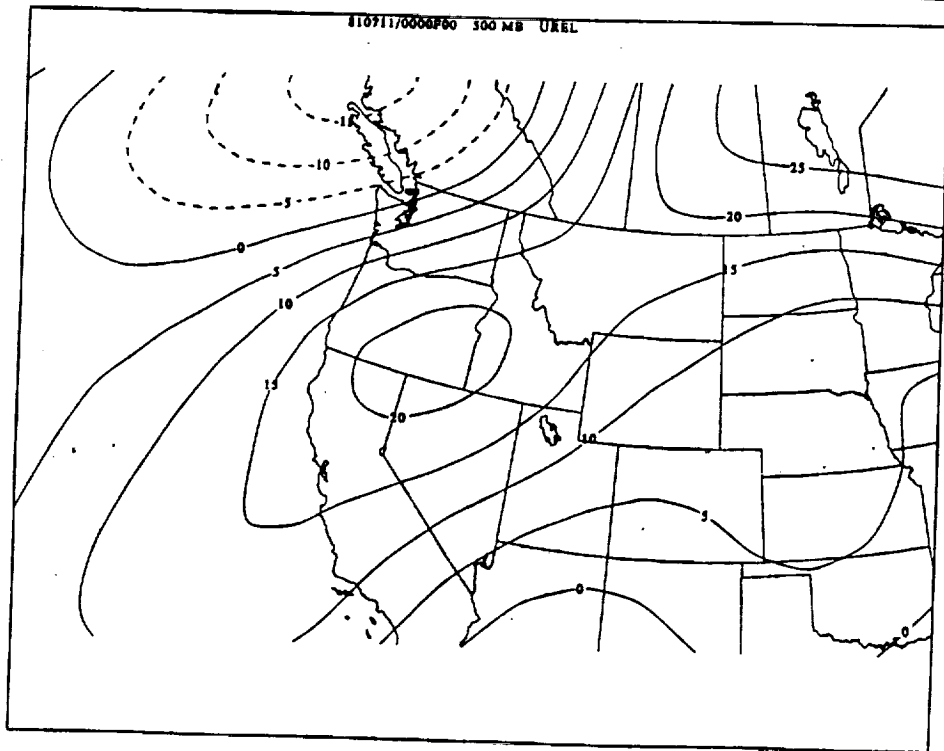
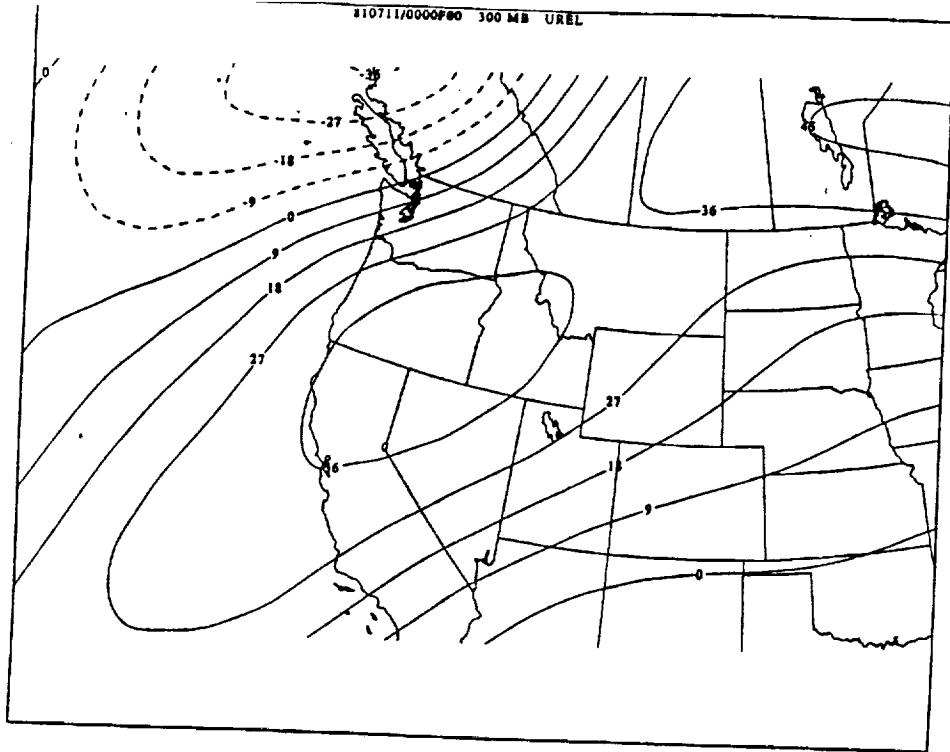
Fig. 8: Cross sections of simulated (a) total wind vectors ( $\text{ms}^{-1}$ ), isotachs ( $\text{ms}^{-1}$ ), and potential temperature (K) valid at 1800 UTC 11 July 1981 and (b) total wind vectors ( $\text{ms}^{-1}$ ) and potential temperature (K) valid at 0000 UTC 12 July 1981. Location is the same as in Figure 2d.

Fig. 9: Simulated (a) 50 kPa vertical velocity (upward dashed in  $10^{-4} \text{ kPa s}^{-1}$ ), (b) 50 kPa height (solid in m) and temperature (dashed in C), (c) 50 kPa u-component isotachs ( $\text{ms}^{-1}$ ), (d) 50 kPa v-component isotachs ( $\text{ms}^{-1}$ ), (e) 30 kPa u-component isotachs ( $\text{ms}^{-1}$ ) and (f) 30 kPa v-component isotachs ( $\text{ms}^{-1}$ ) all valid between 1900 UTC 11 July and 0000 UTC 12 July 1981.

Fig. 10: Cross sections of simulated total wind vectors ( $\text{ms}^{-1}$ ) and potential temperature (K) valid between 0100 UTC 12 July and 1200 UTC 12 July 1981. Location is the same as in Figure 2d.

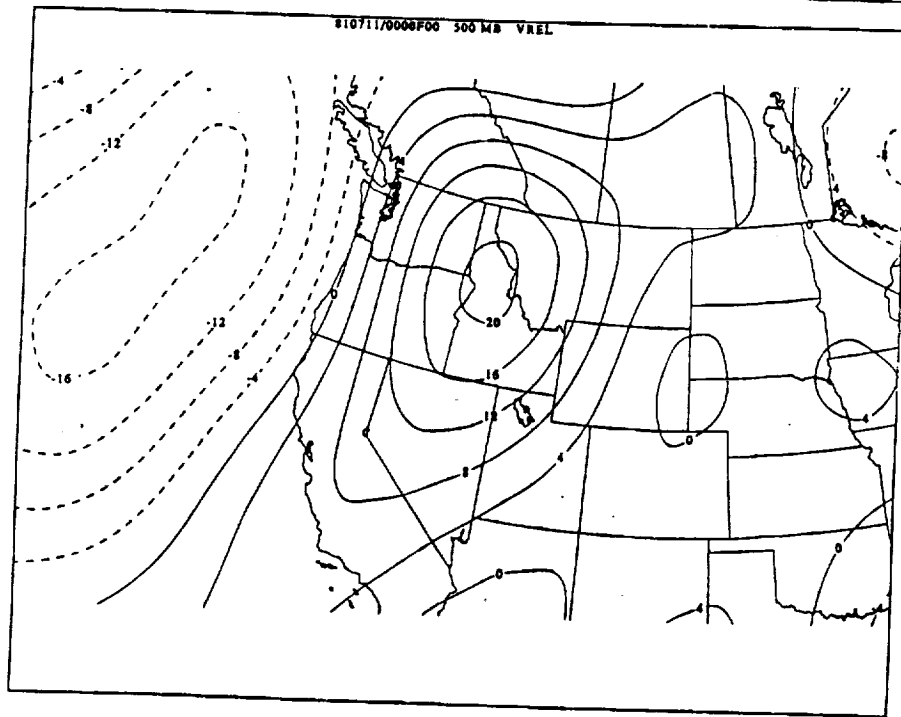
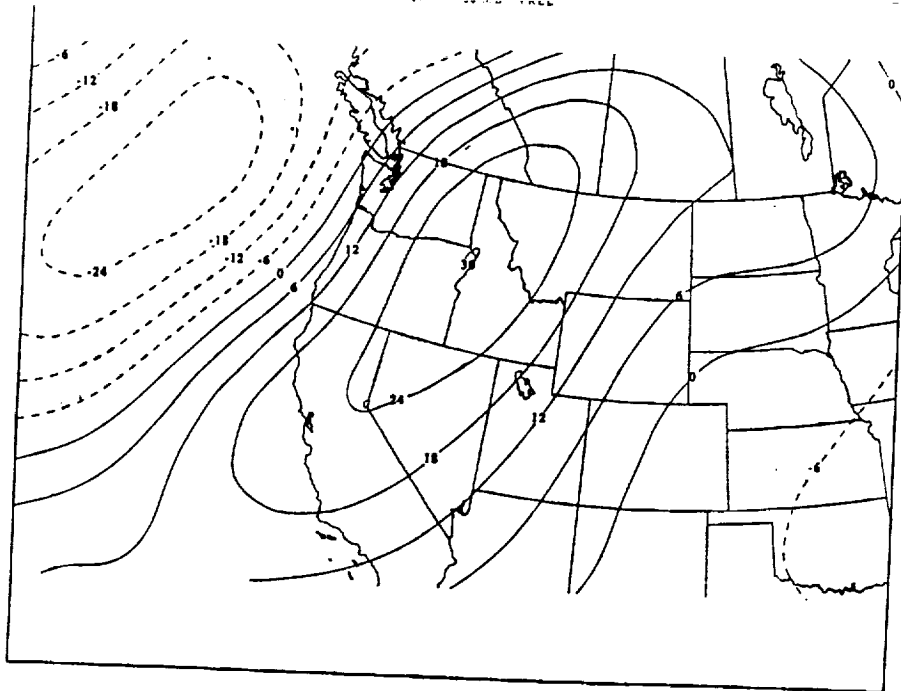
Fig. 11: Simulated (a) 50 kPa height (solid in m) and temperature (dashed in C), (b) 50 kPa u-component isotachs ( $\text{ms}^{-1}$ ), (c) 50 kPa v-component isotachs ( $\text{ms}^{-1}$ ), (d) 50 kPa vertical velocity (upward dashed in  $10^{-4} \text{ kPa s}^{-1}$ ), (e) 30 kPa u-component isotachs ( $\text{ms}^{-1}$ ) and (f) 30 kPa v-component isotachs ( $\text{ms}^{-1}$ ) all valid between 0100 UTC and 0300 UTC 12 July 1981.





**2A**

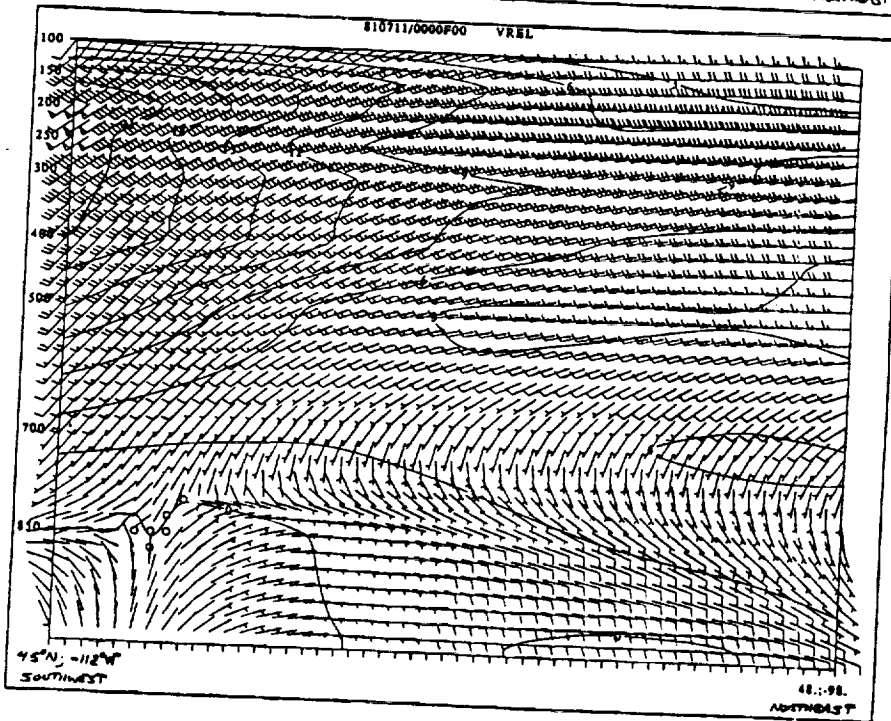
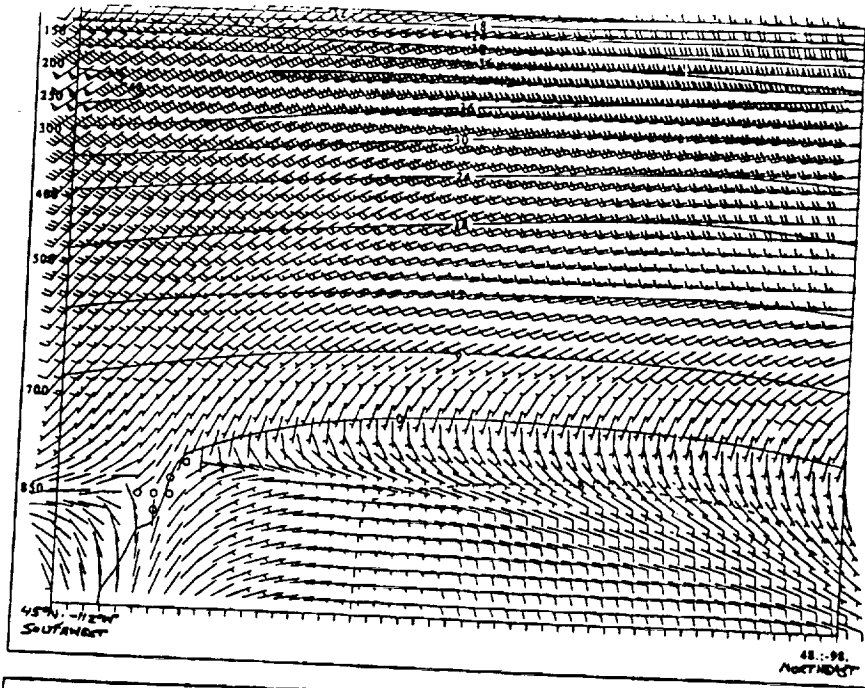
1B



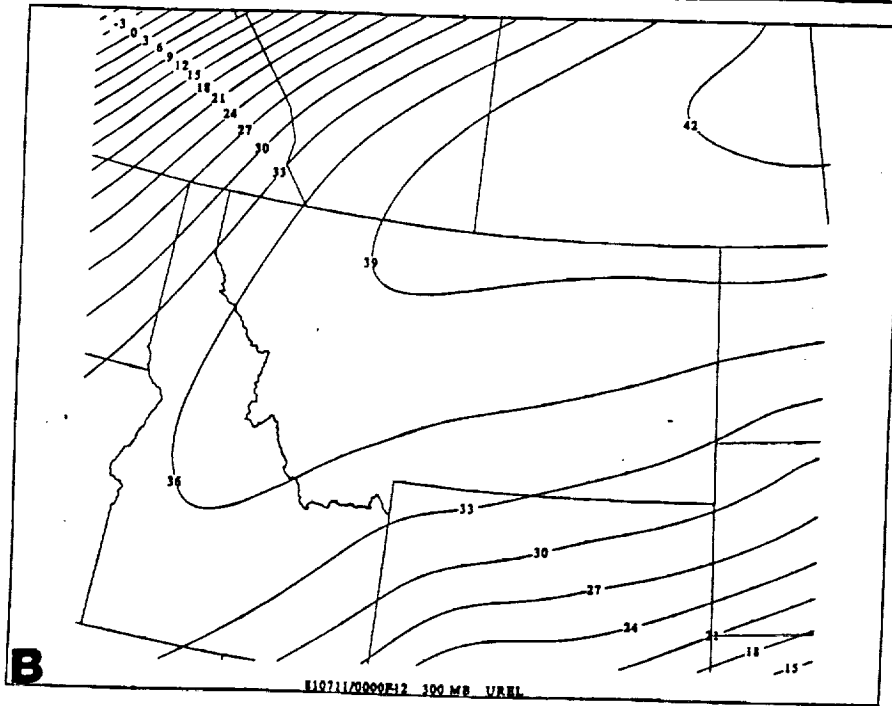
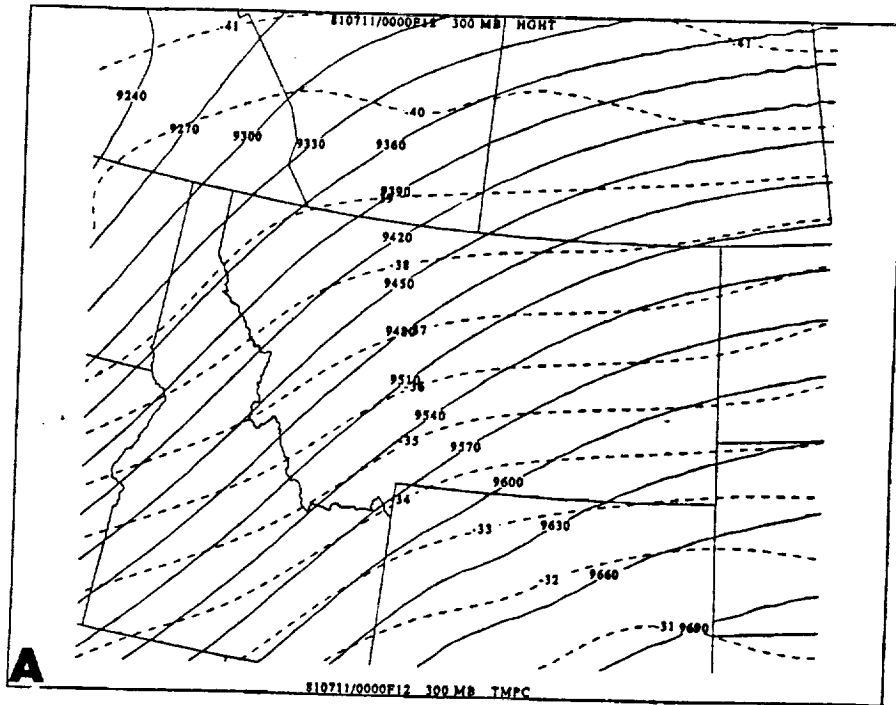
2B



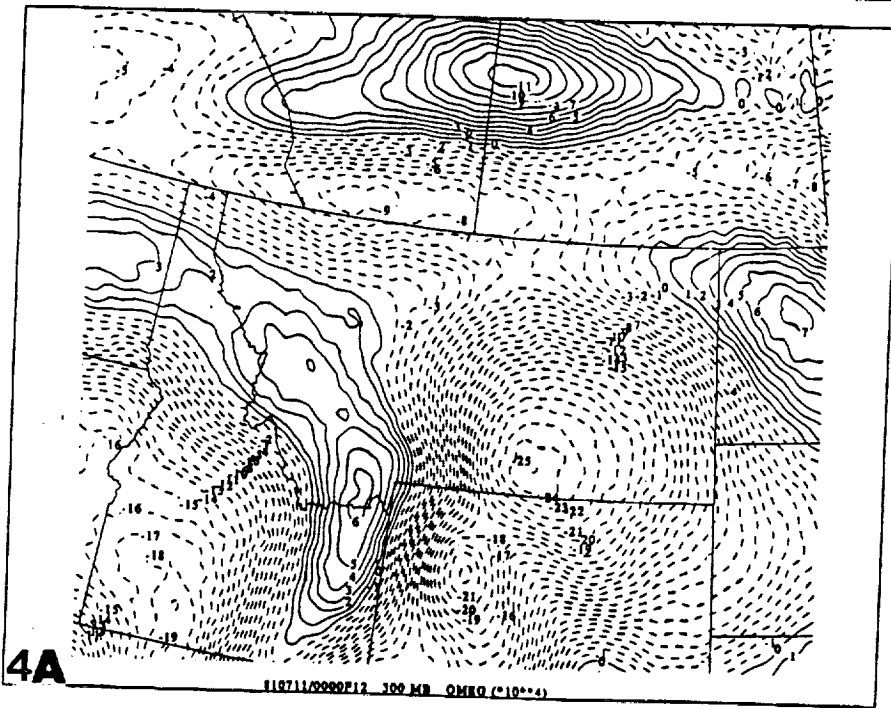
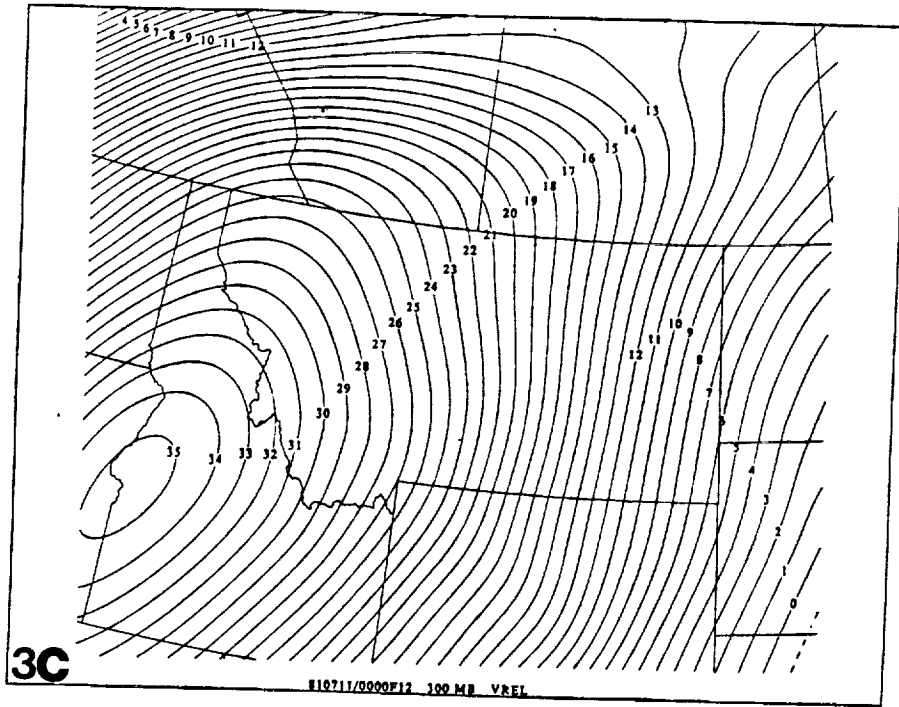
1D  
①



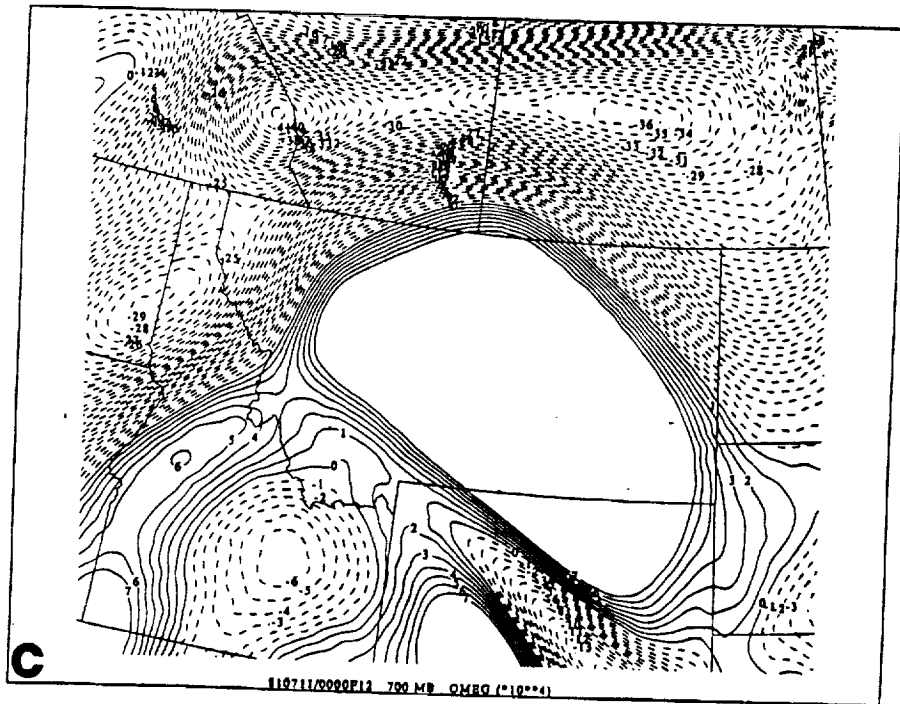
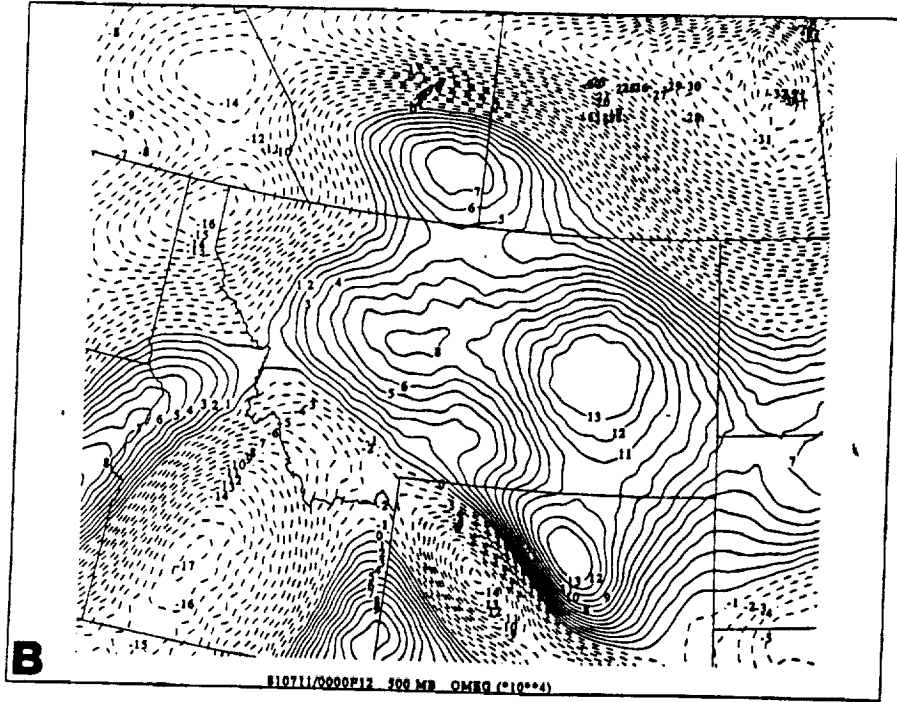
2D

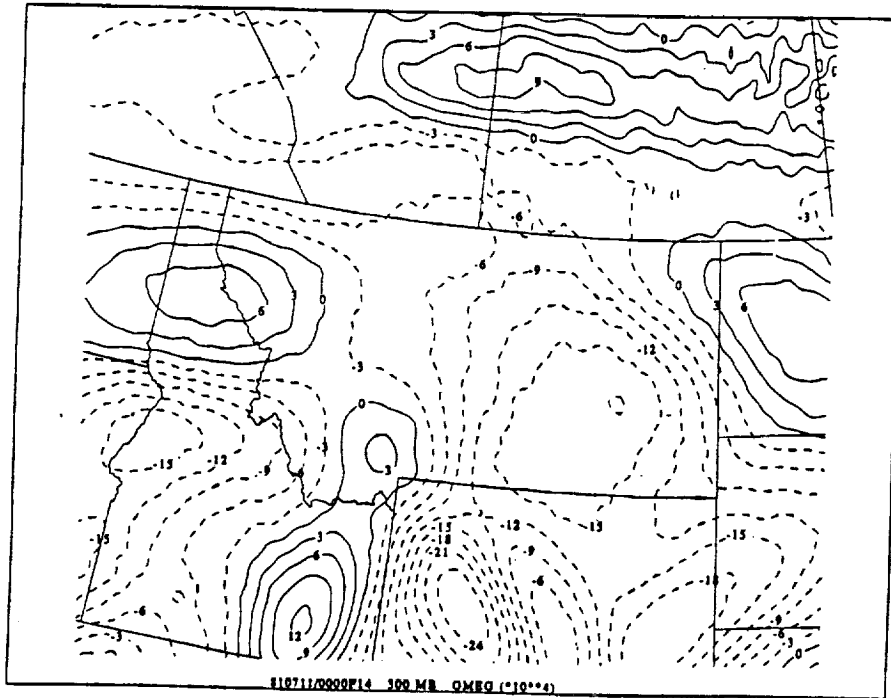
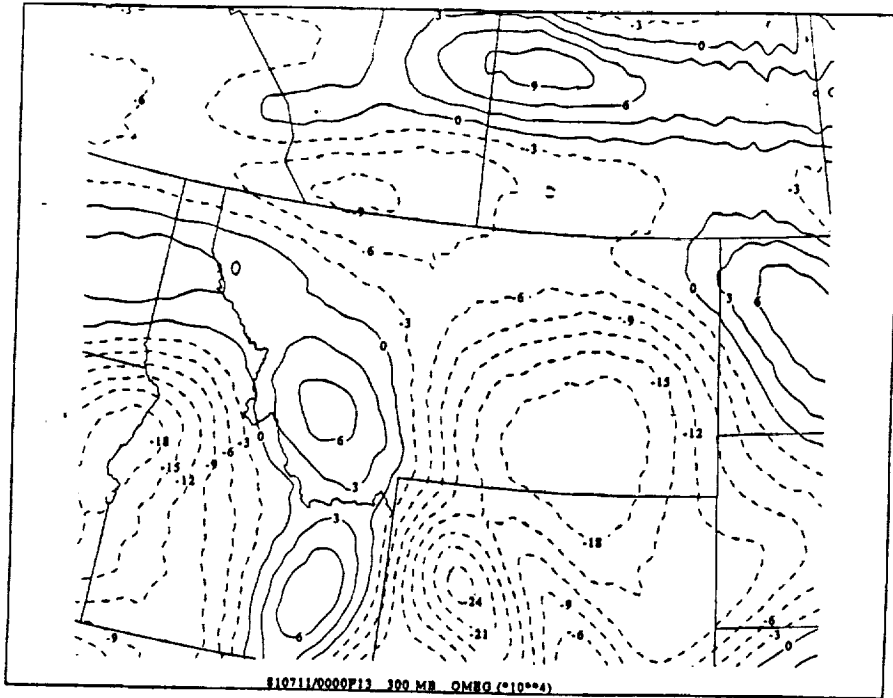




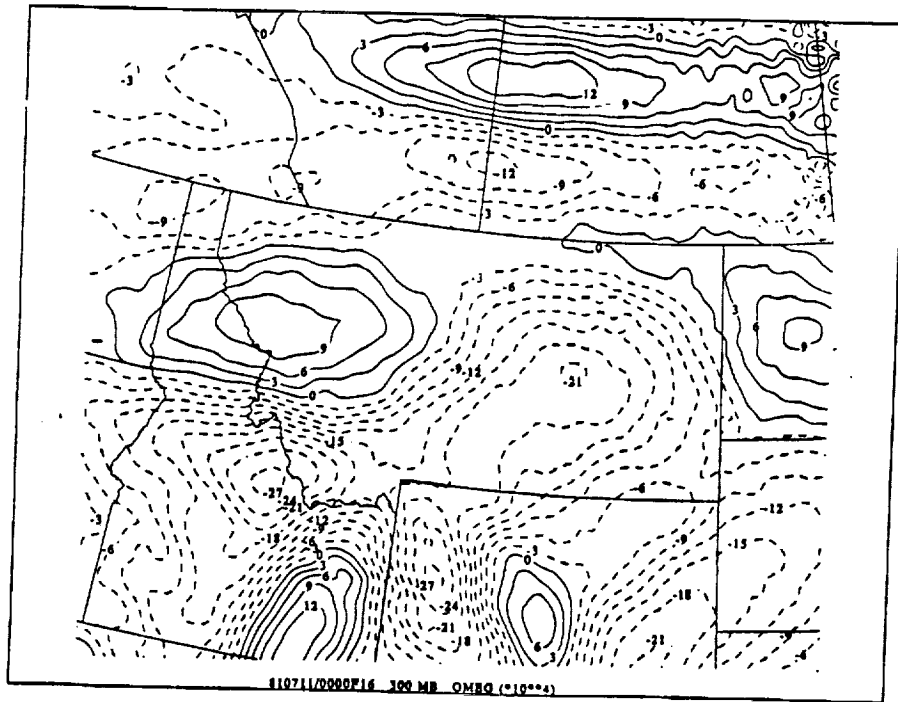
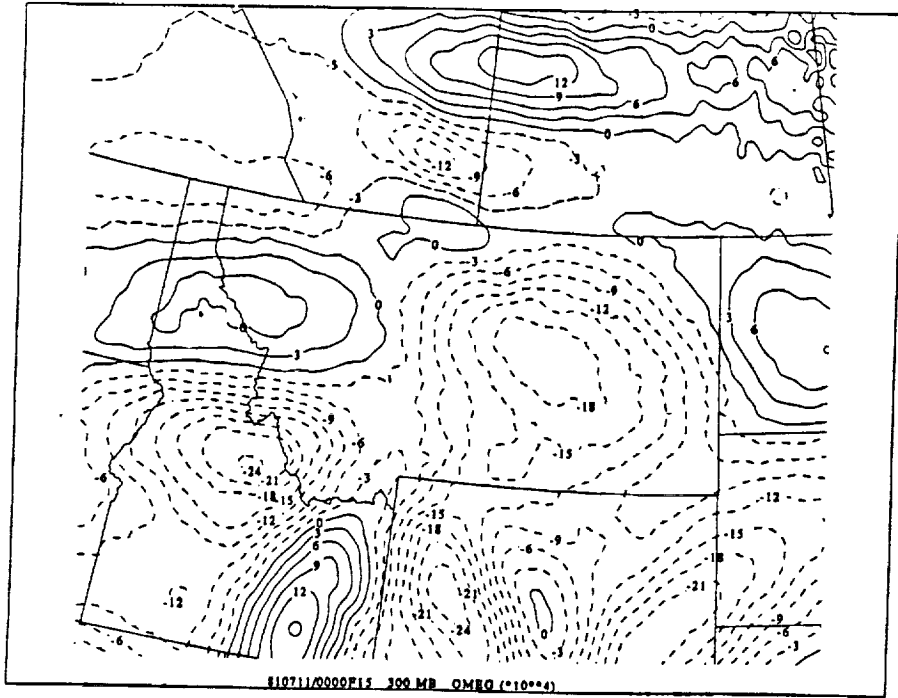


PRECEDING PAGE BLANK NOT FILMED

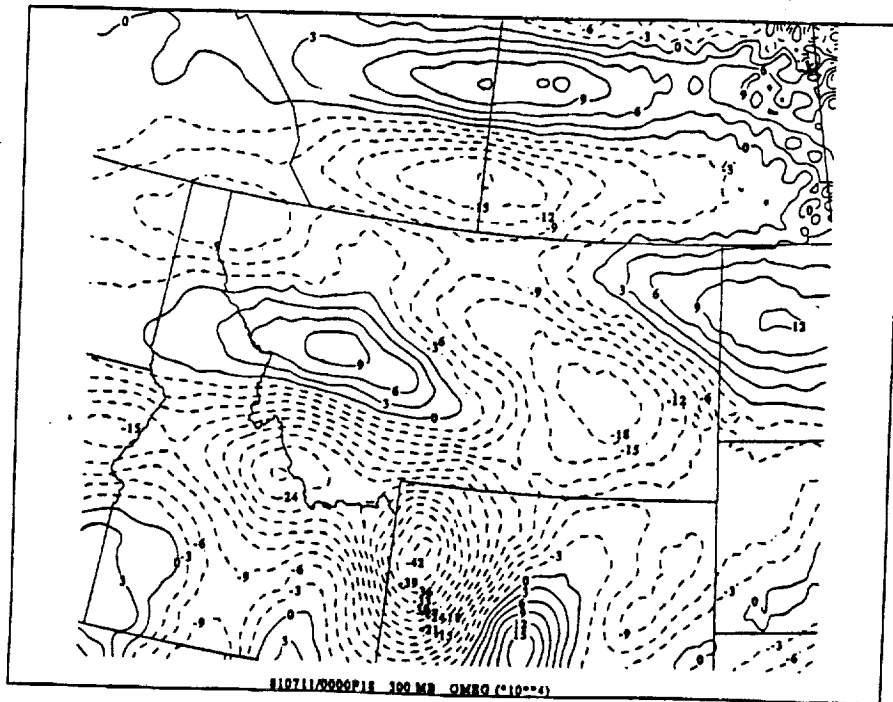
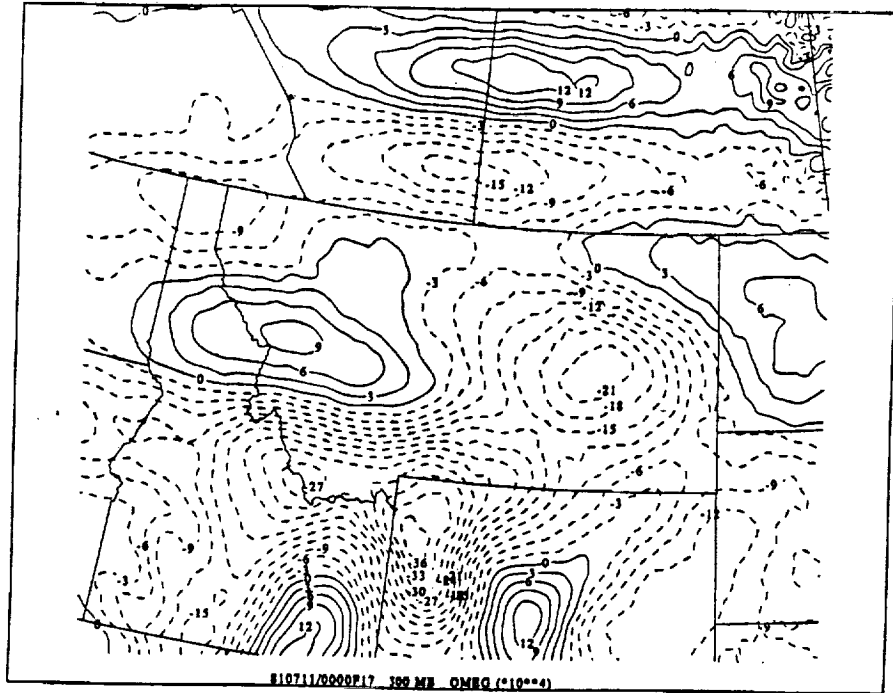




5A

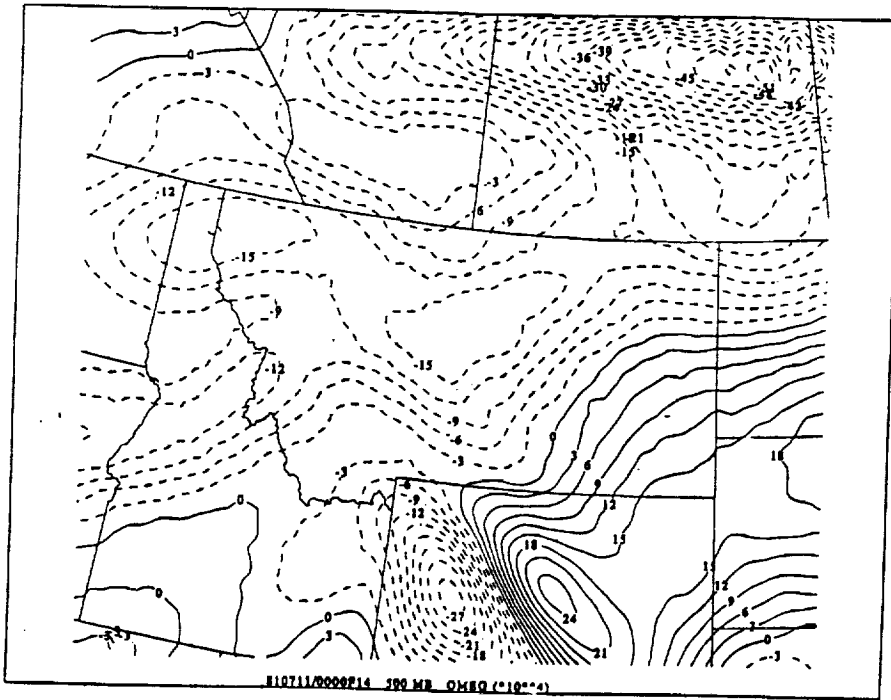
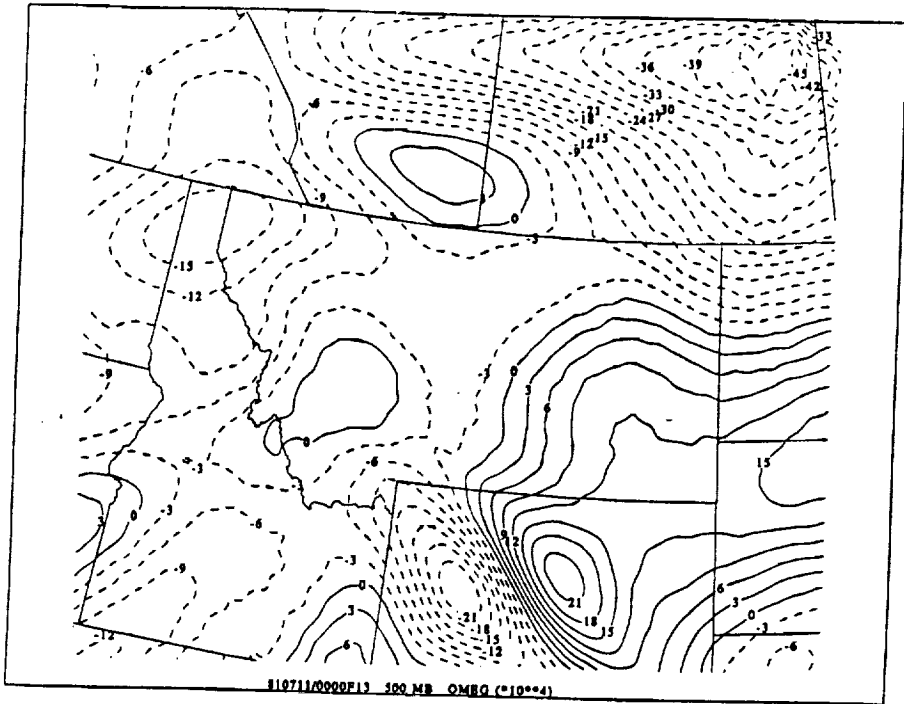


**5A**

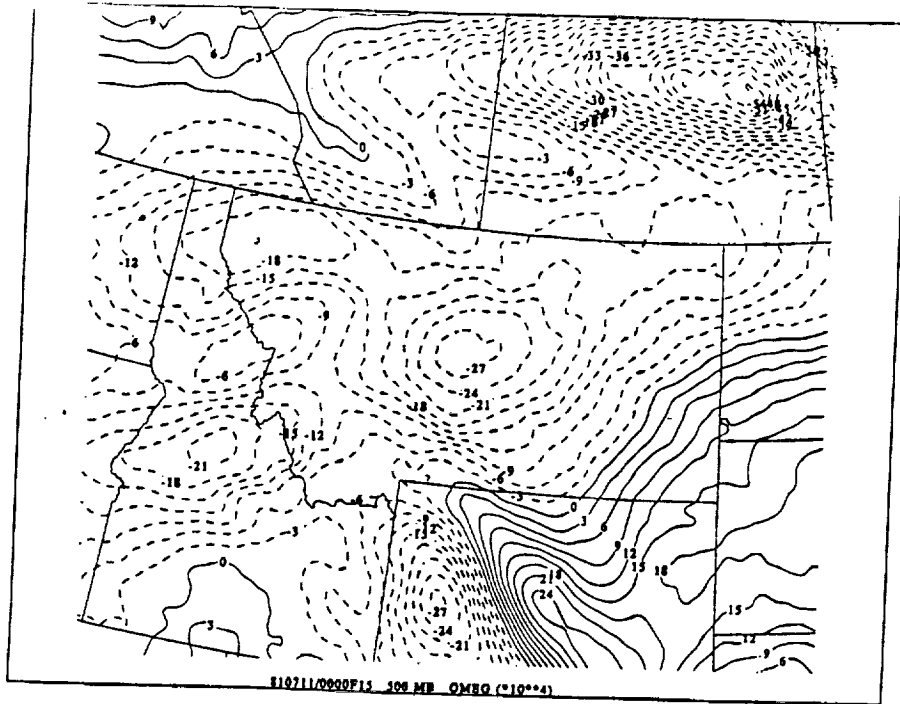


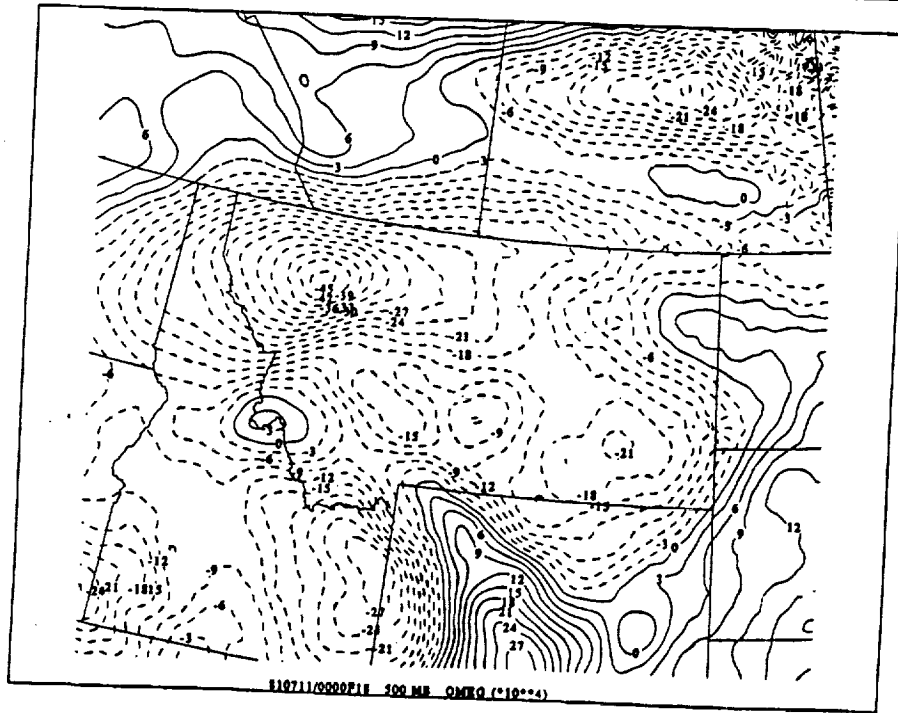
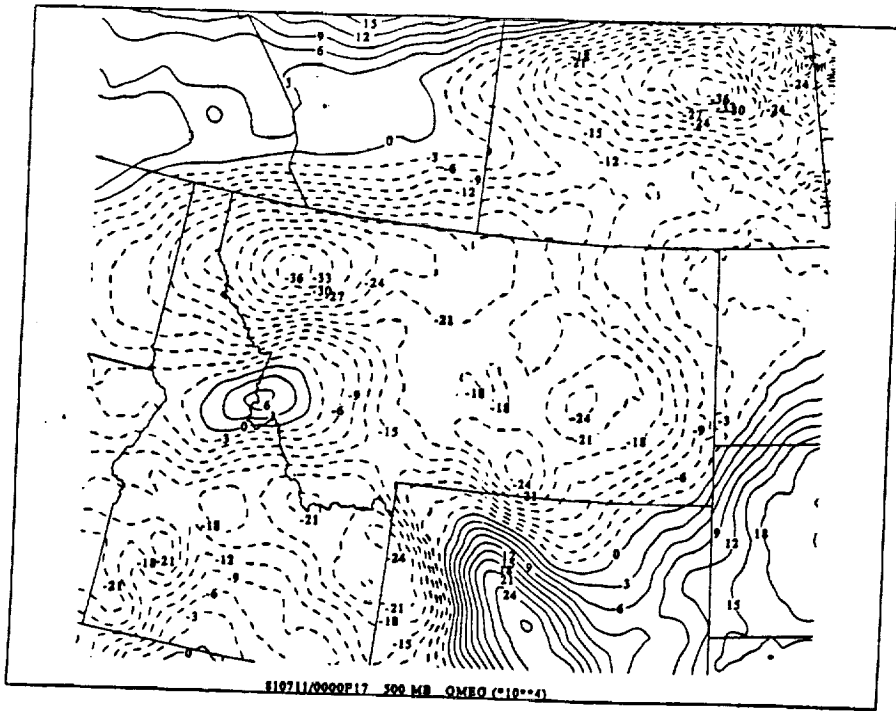
**5A**





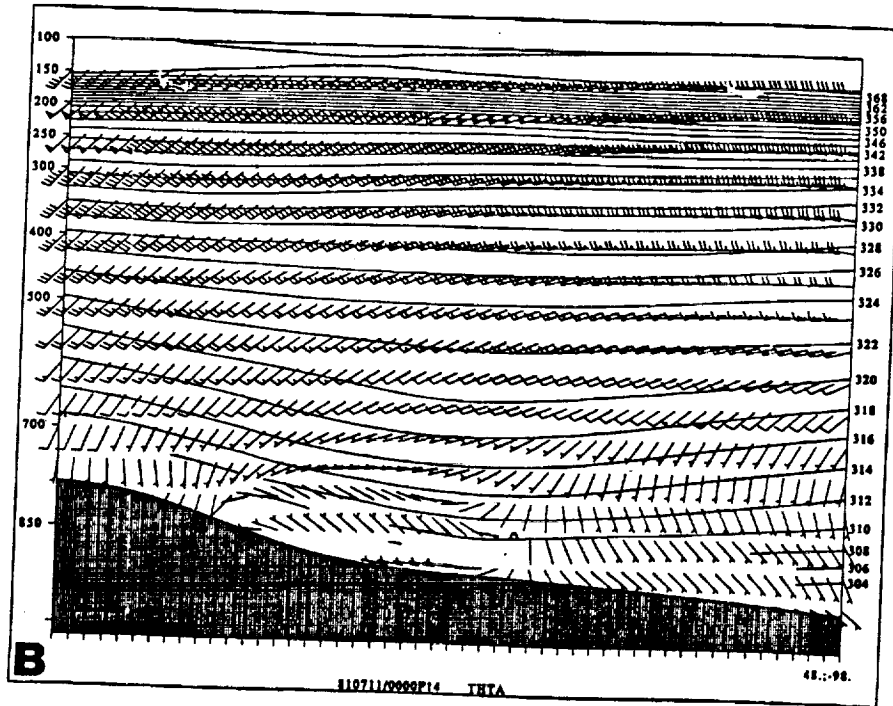
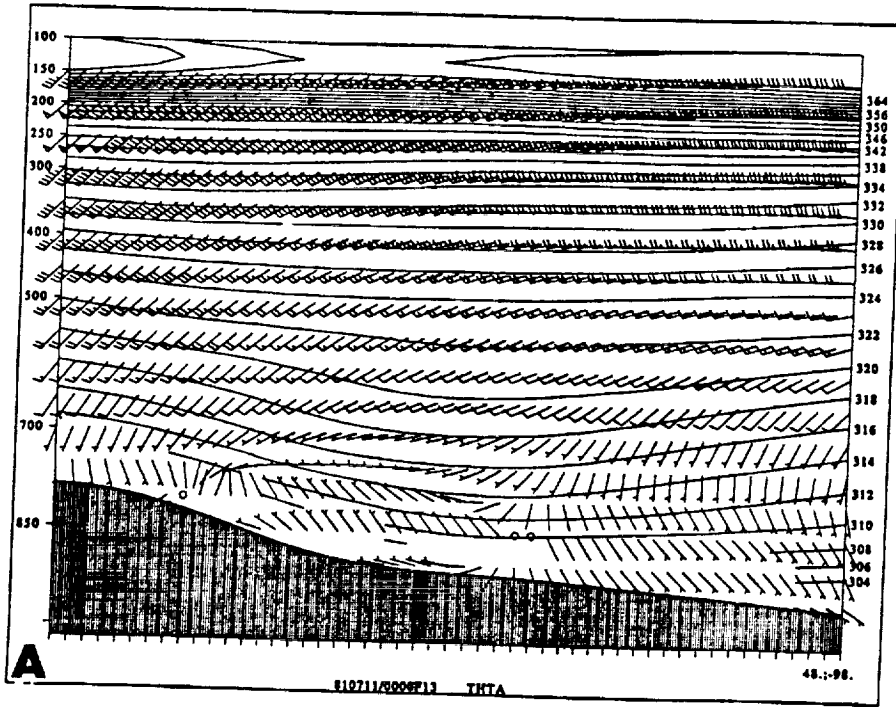
**5B**

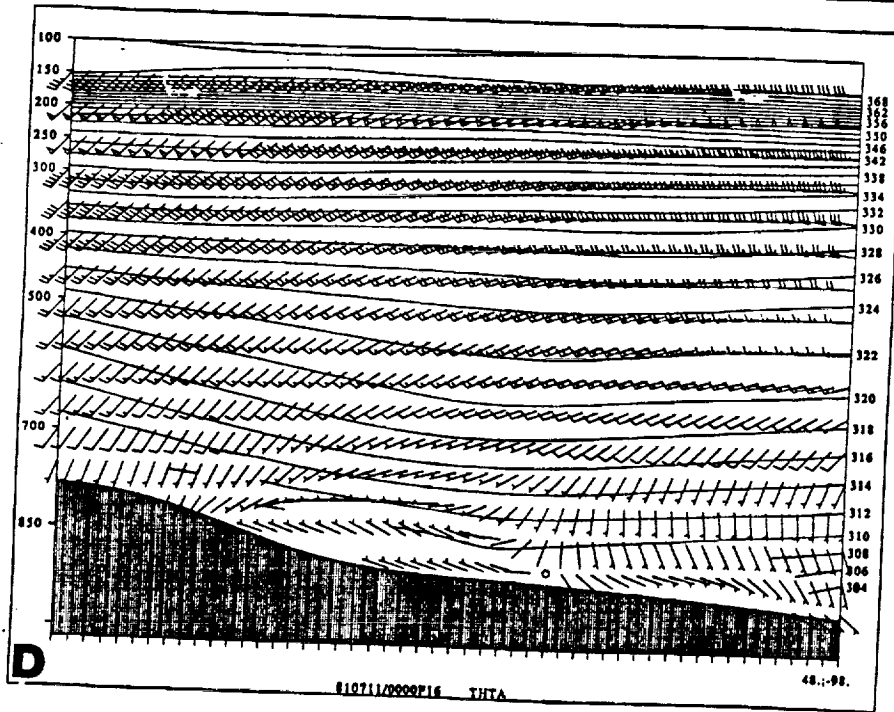
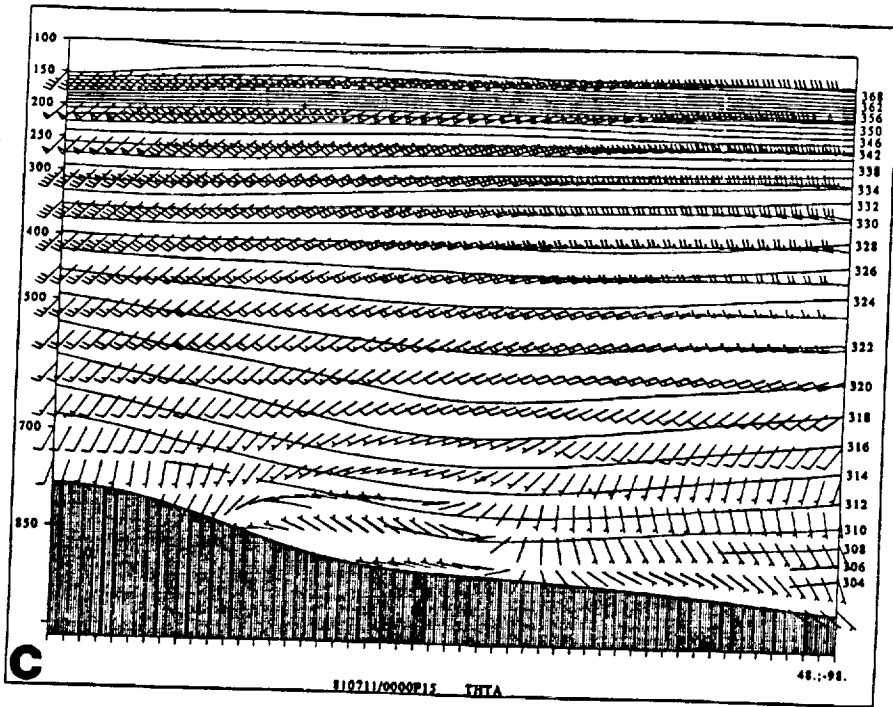


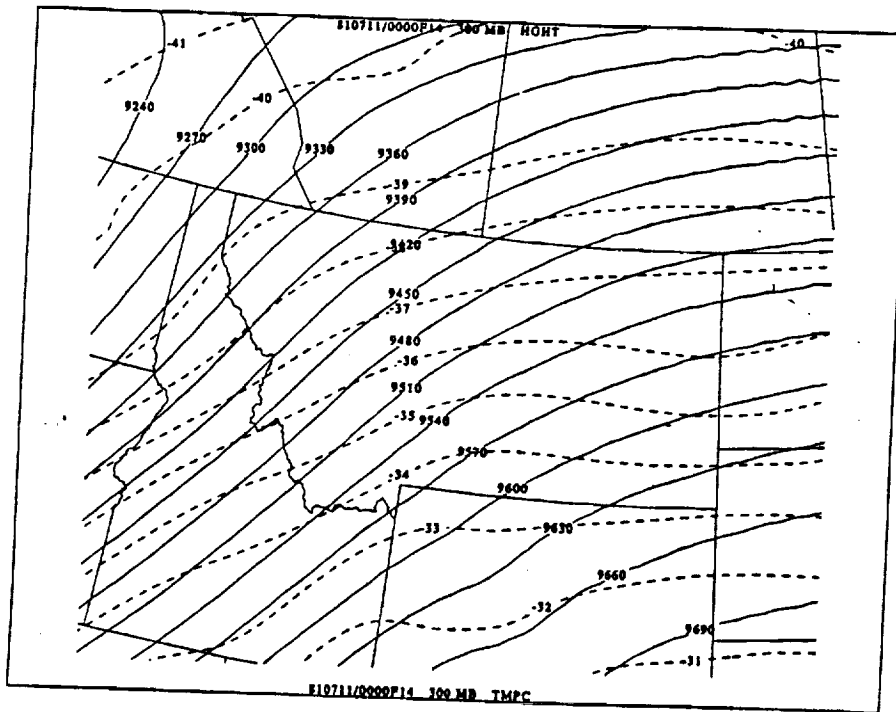
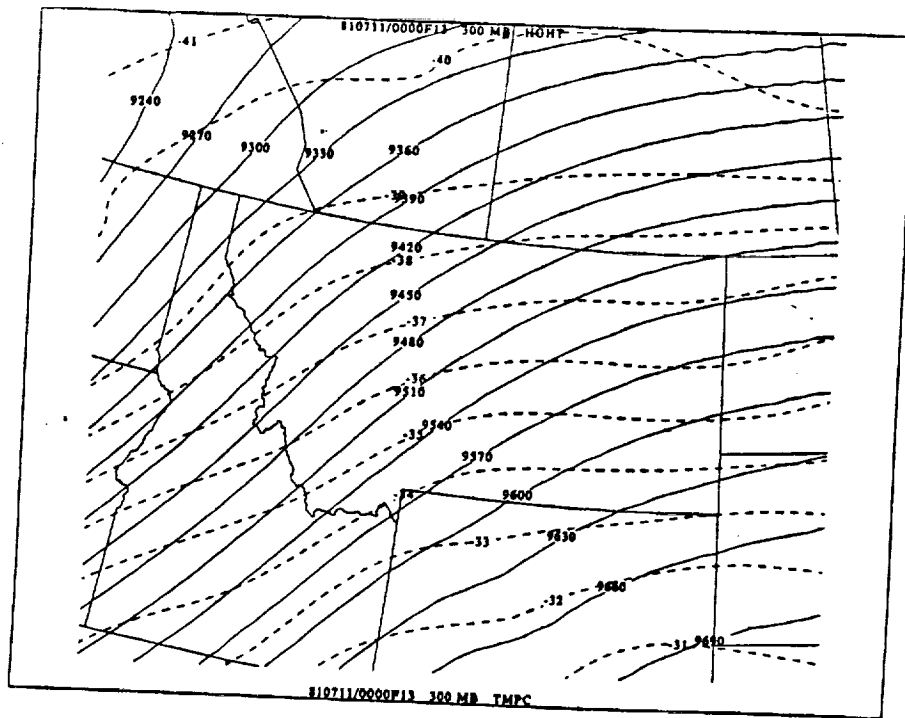


**5B**

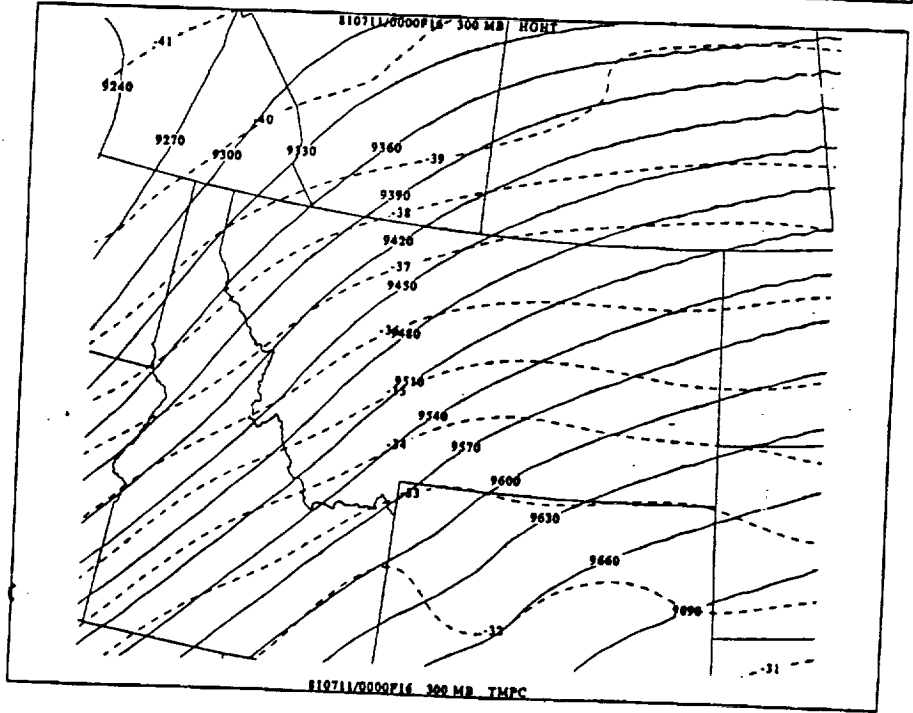
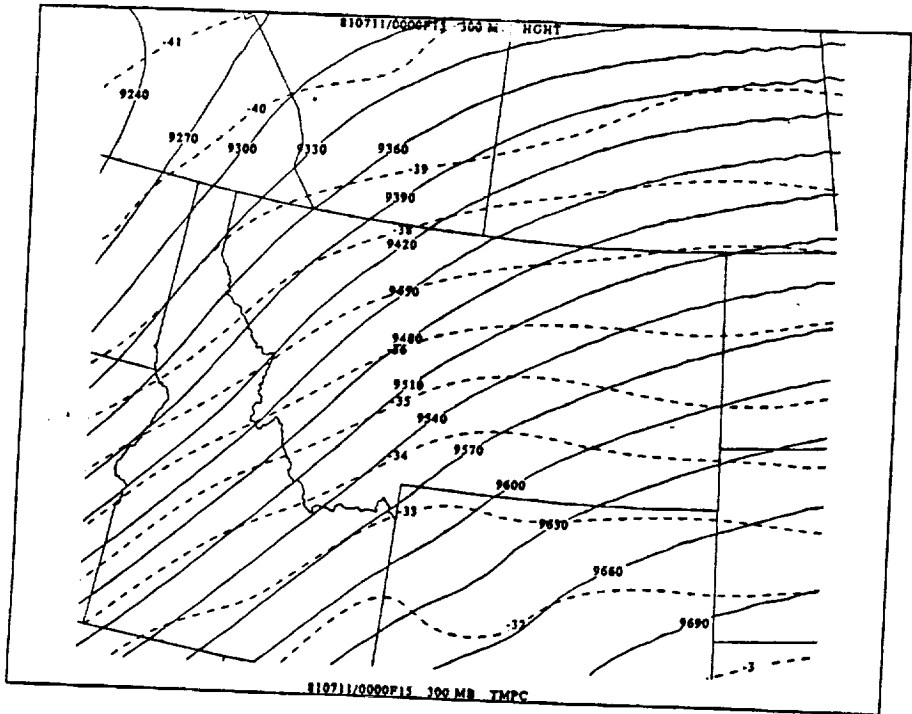


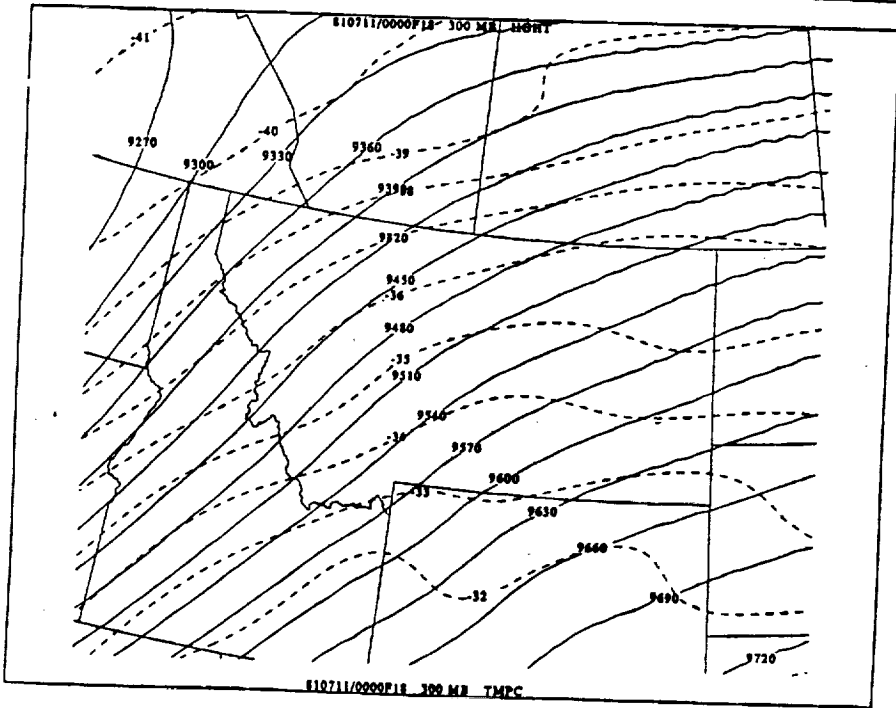
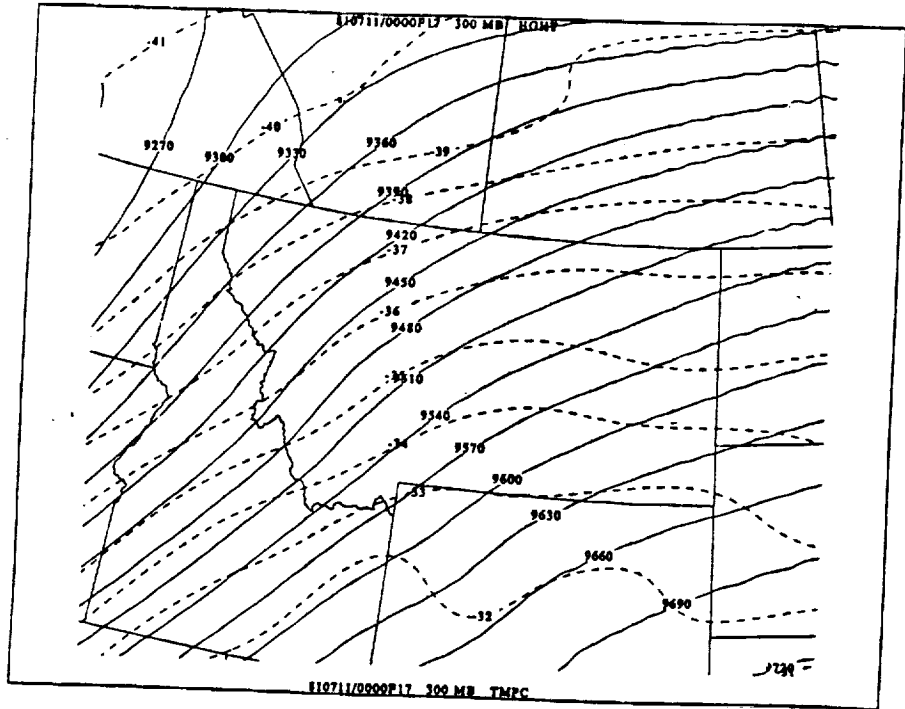




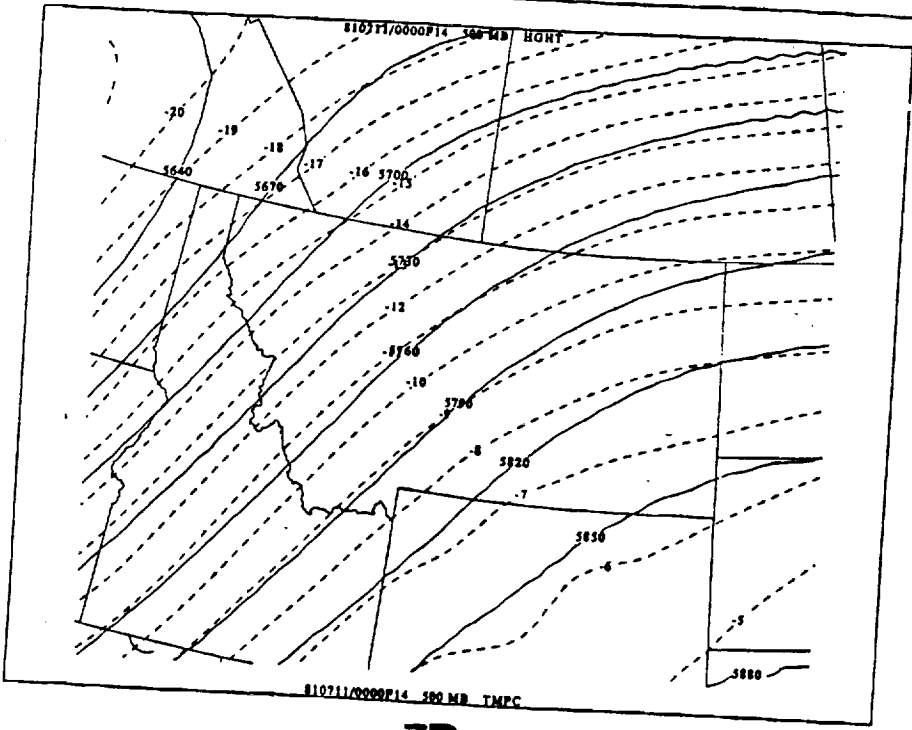
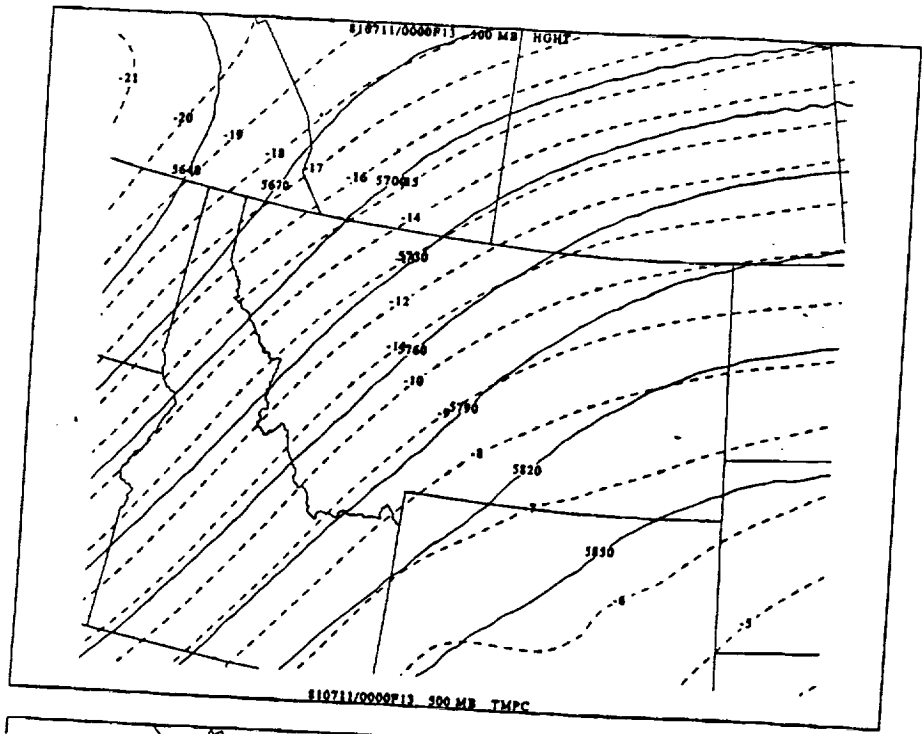


7A

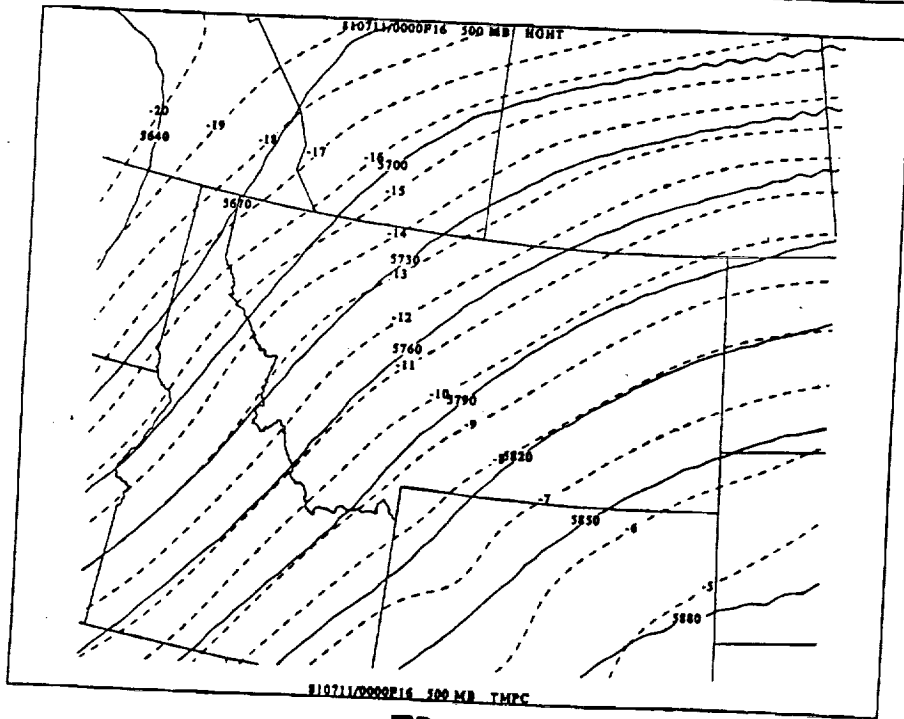
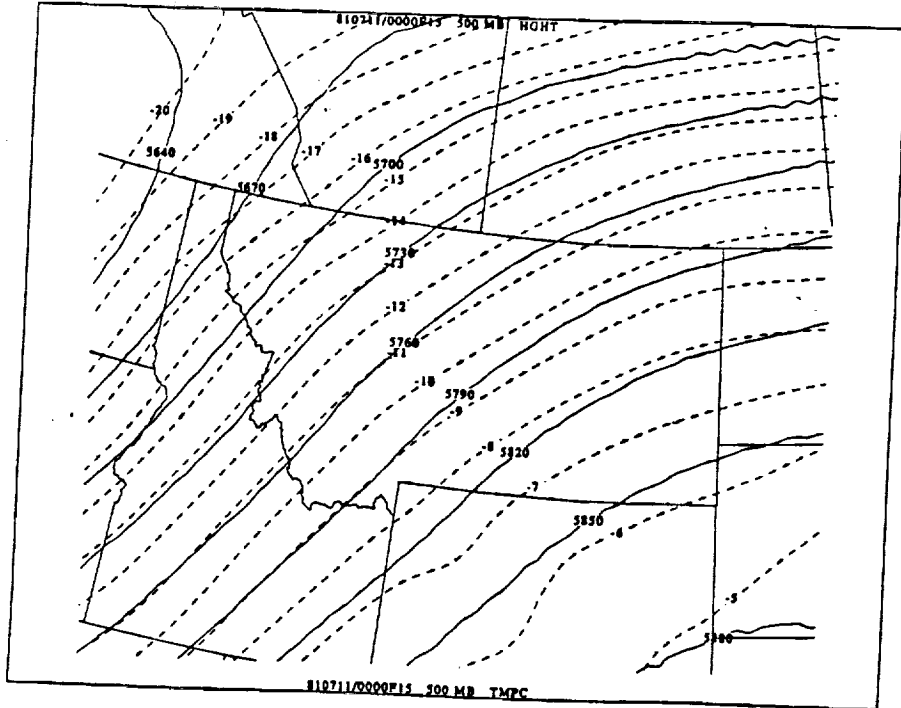




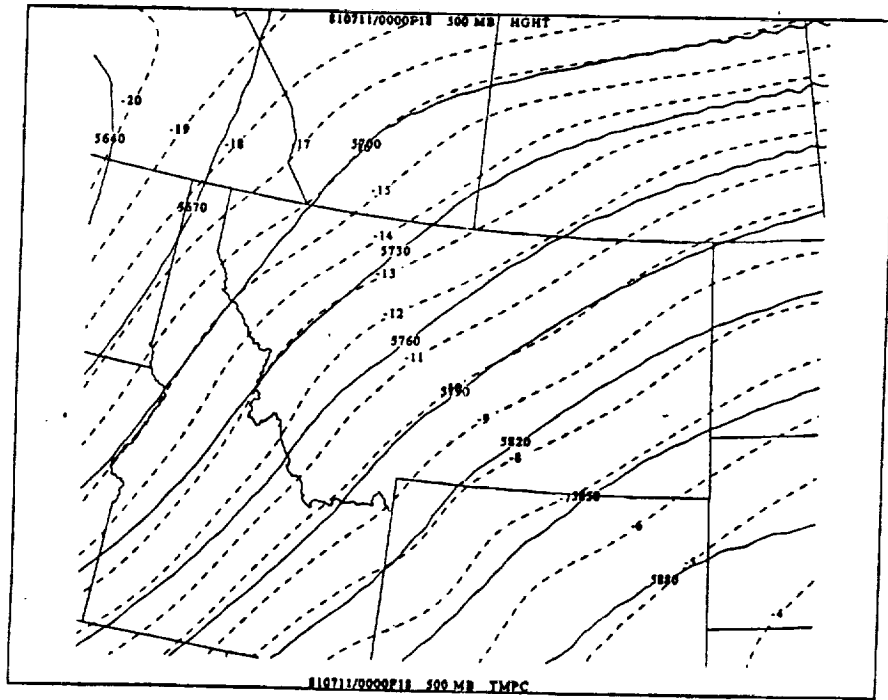
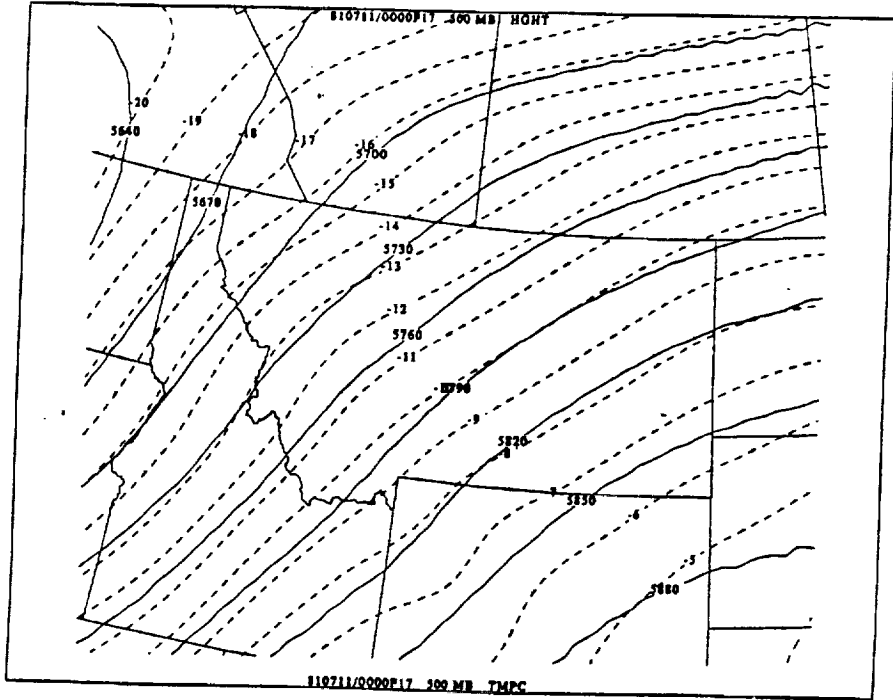
**7A**



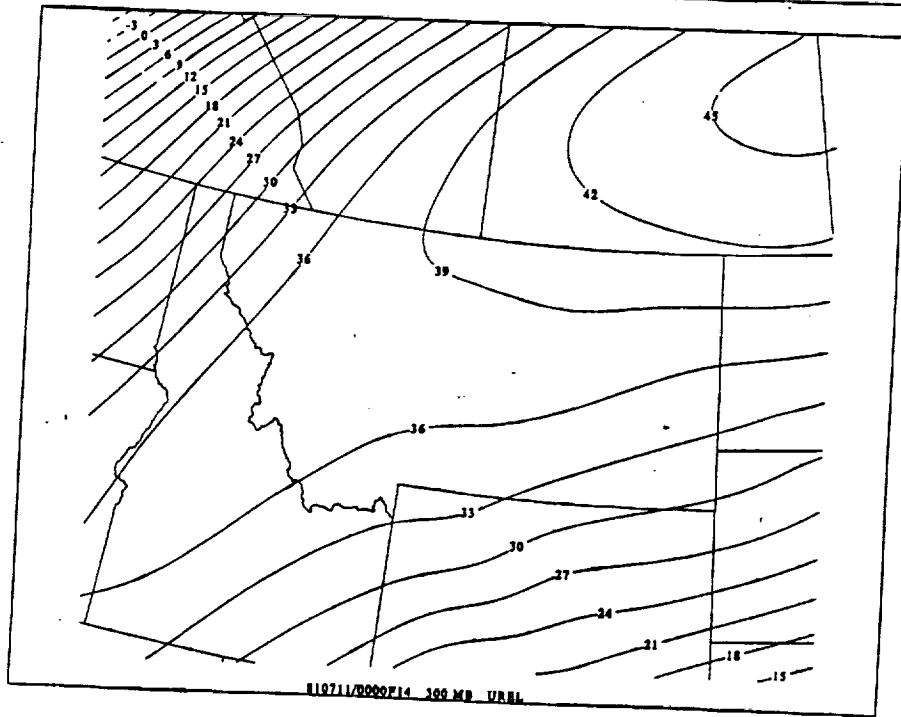
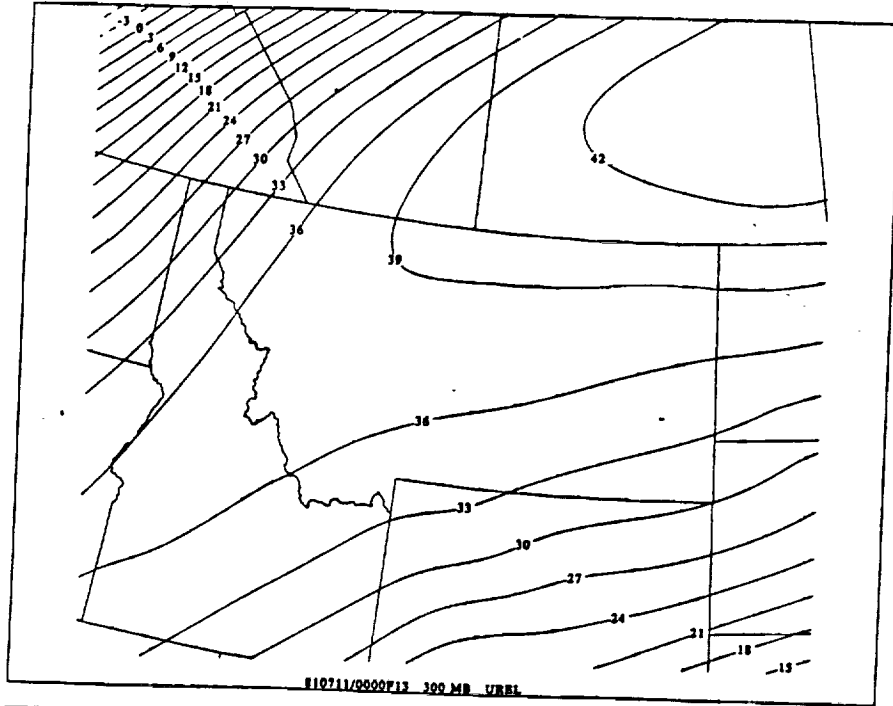
7B



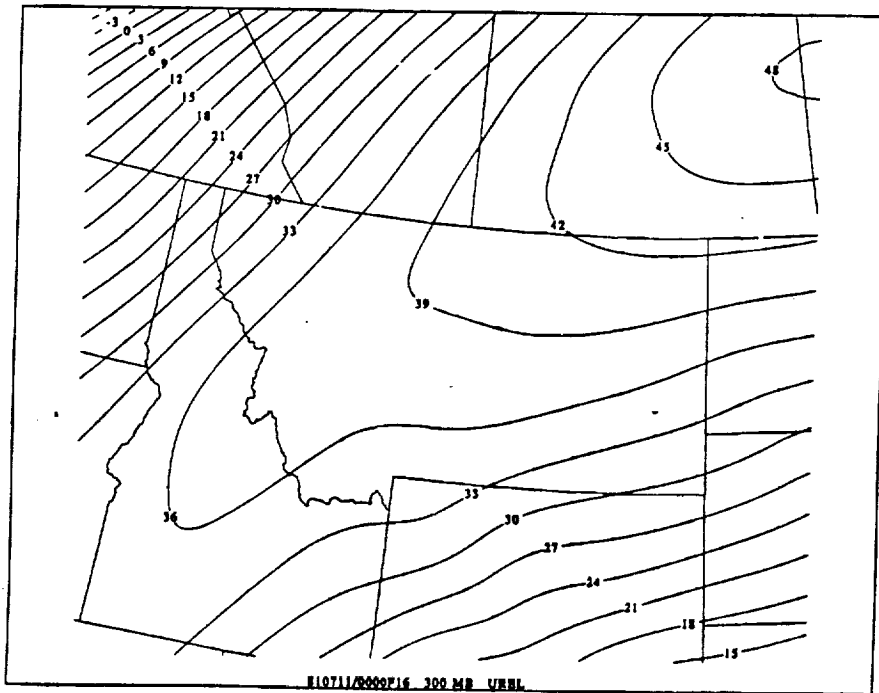
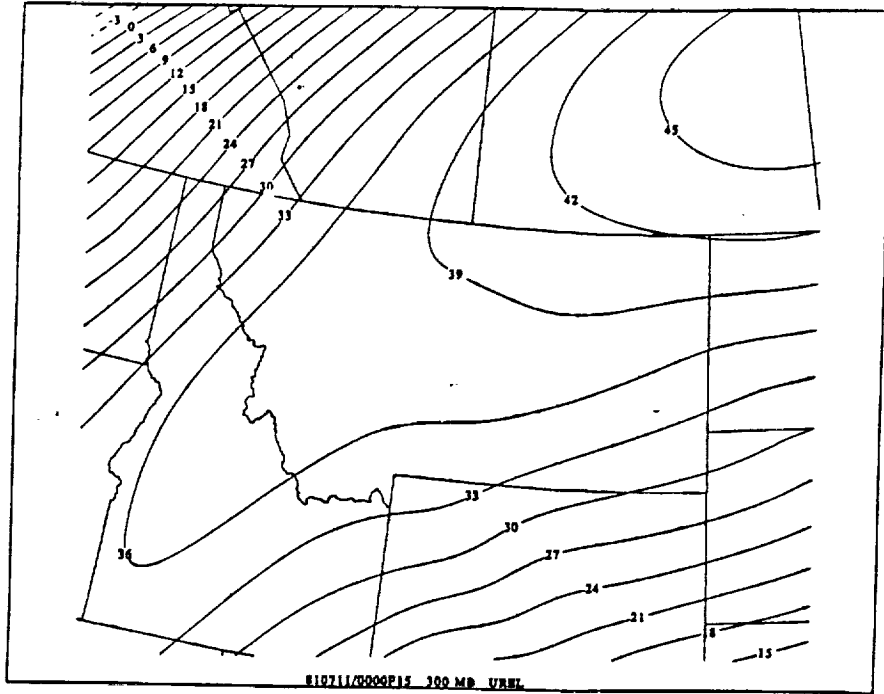
7B



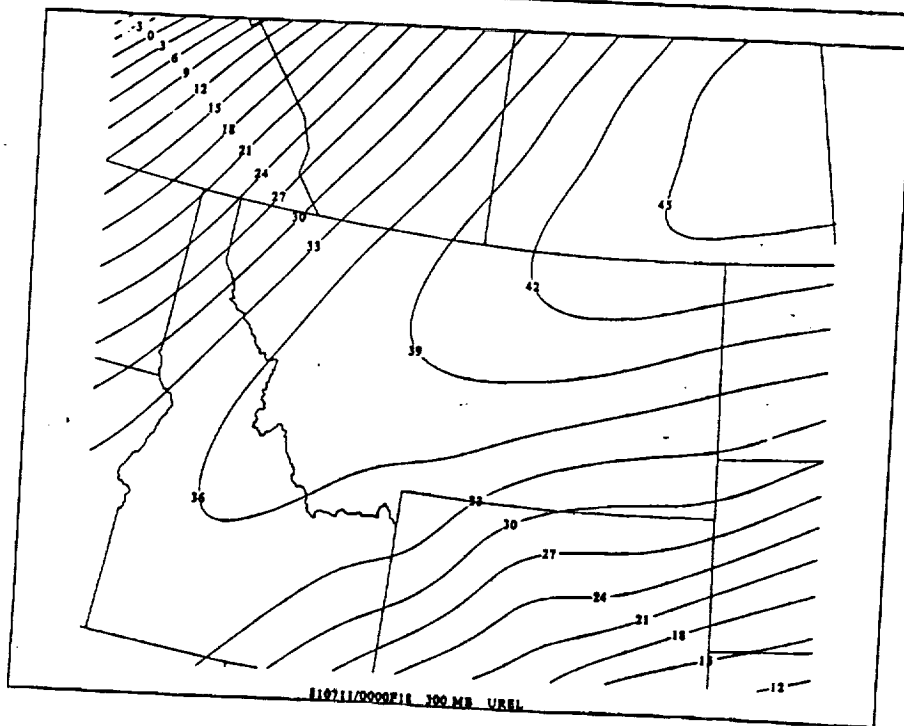
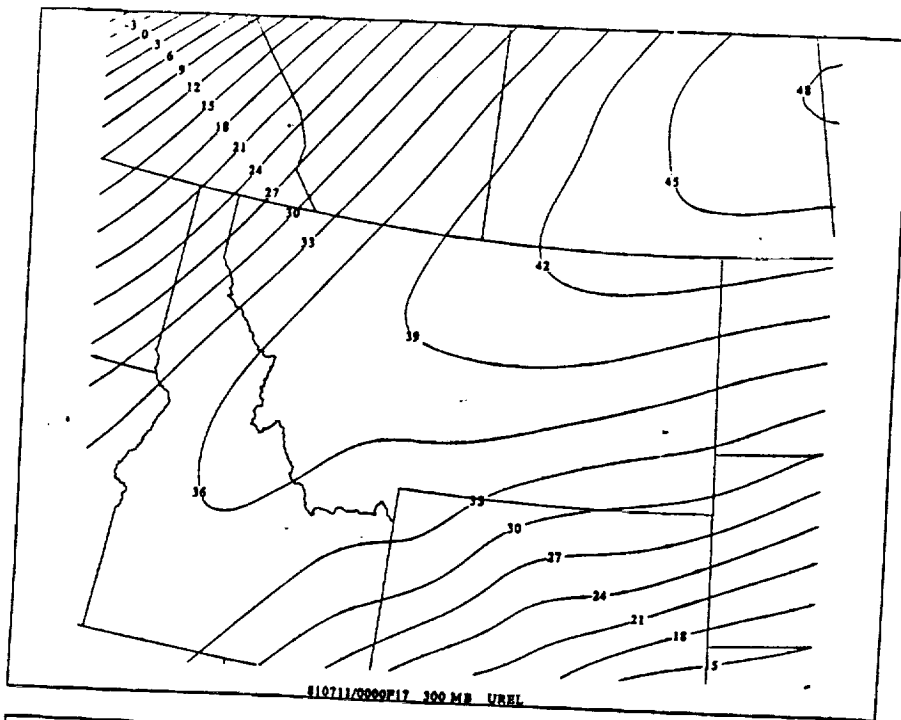




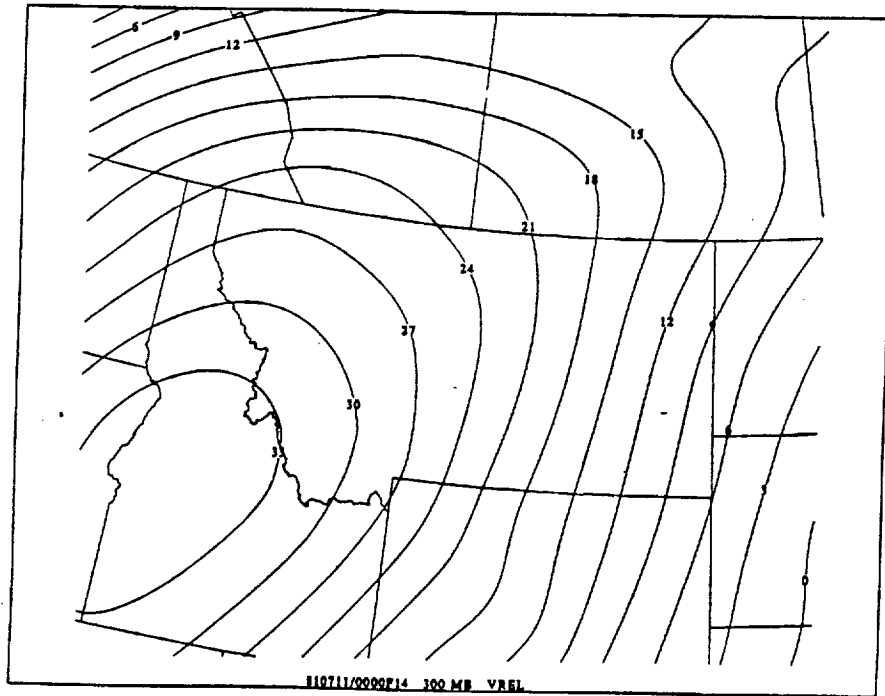
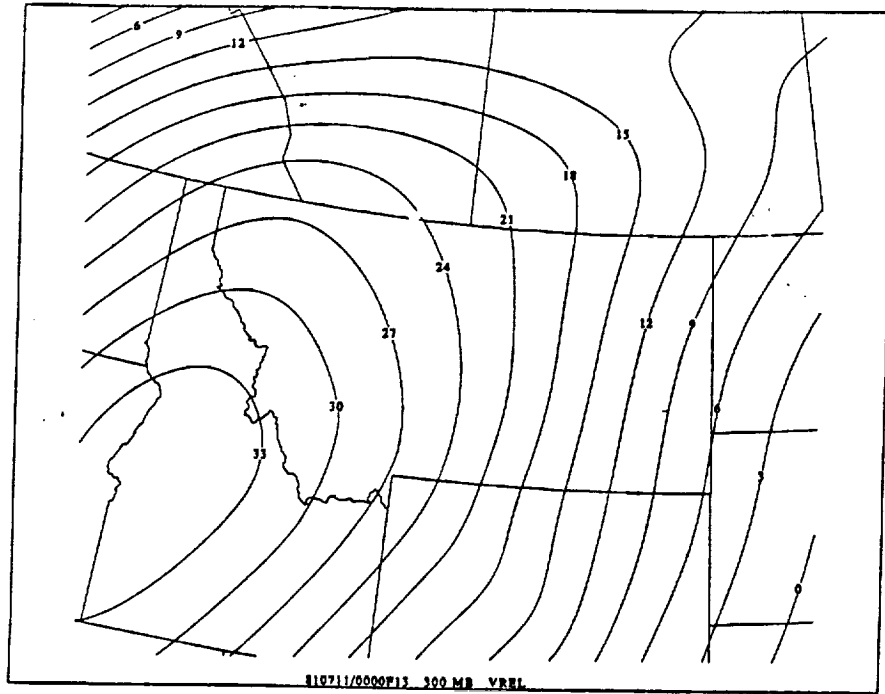
7C



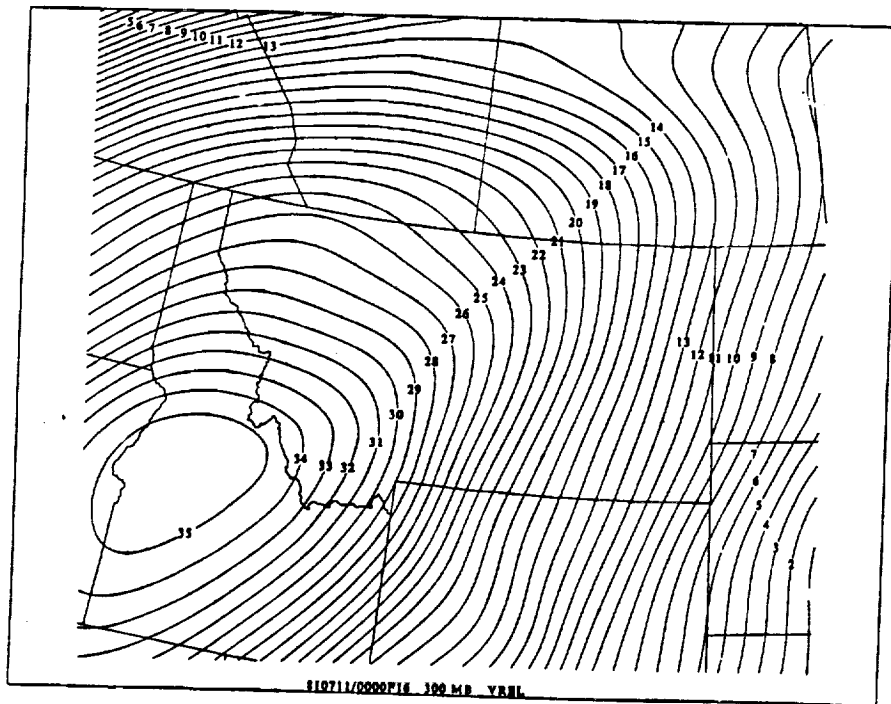
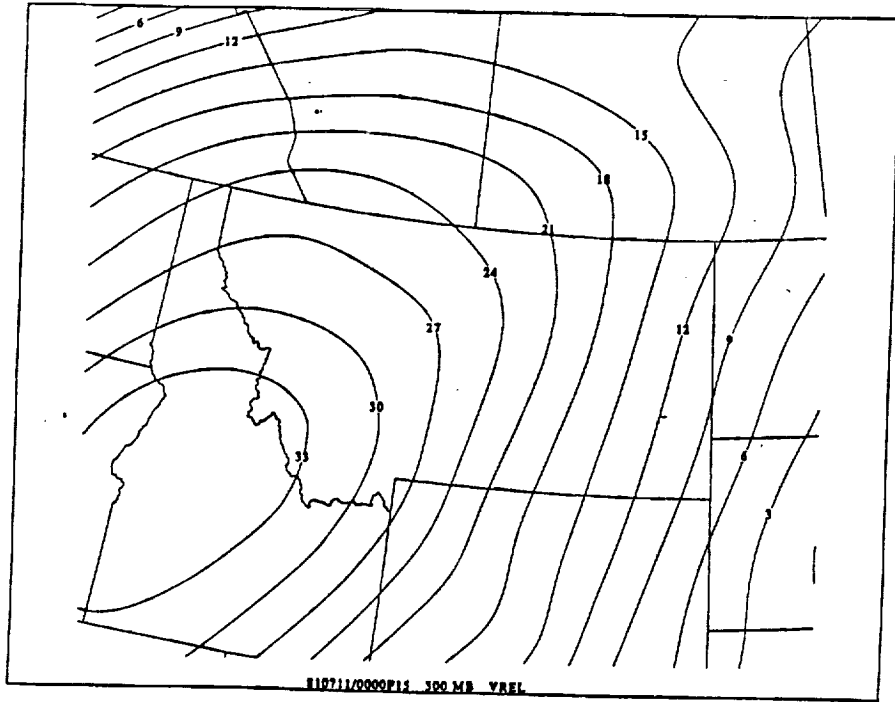
7C



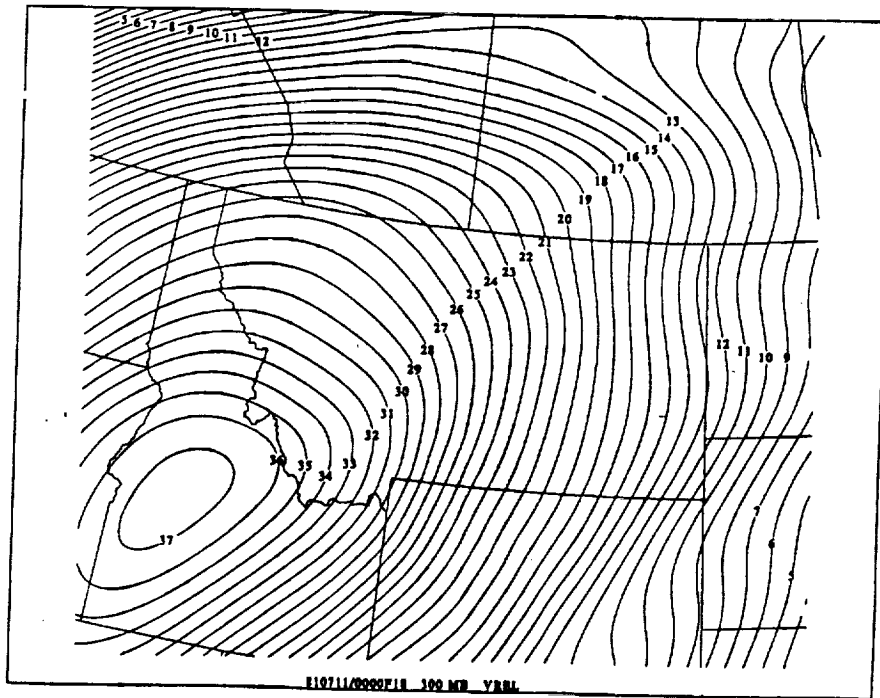
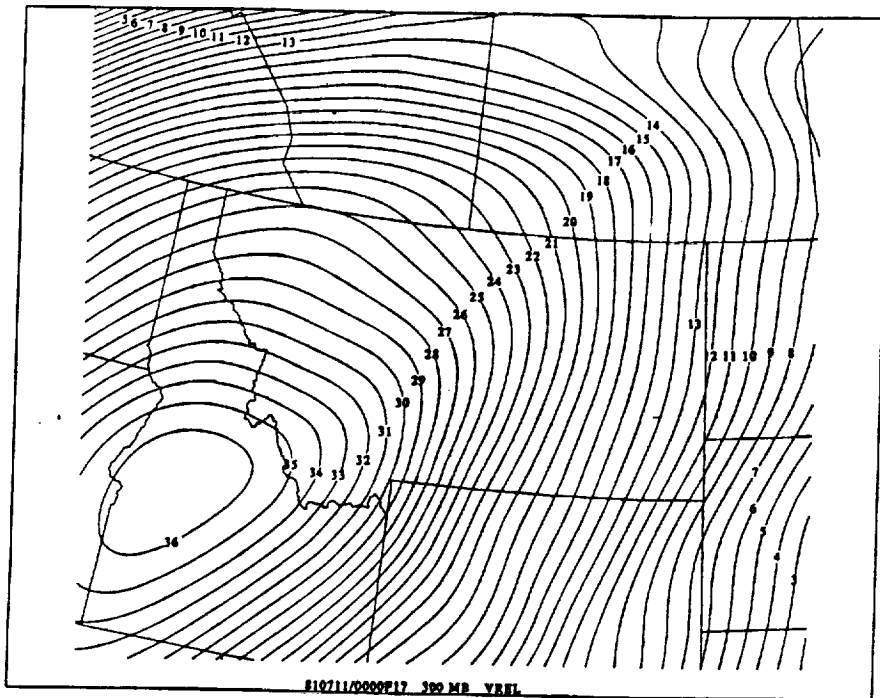
**7C**



7D

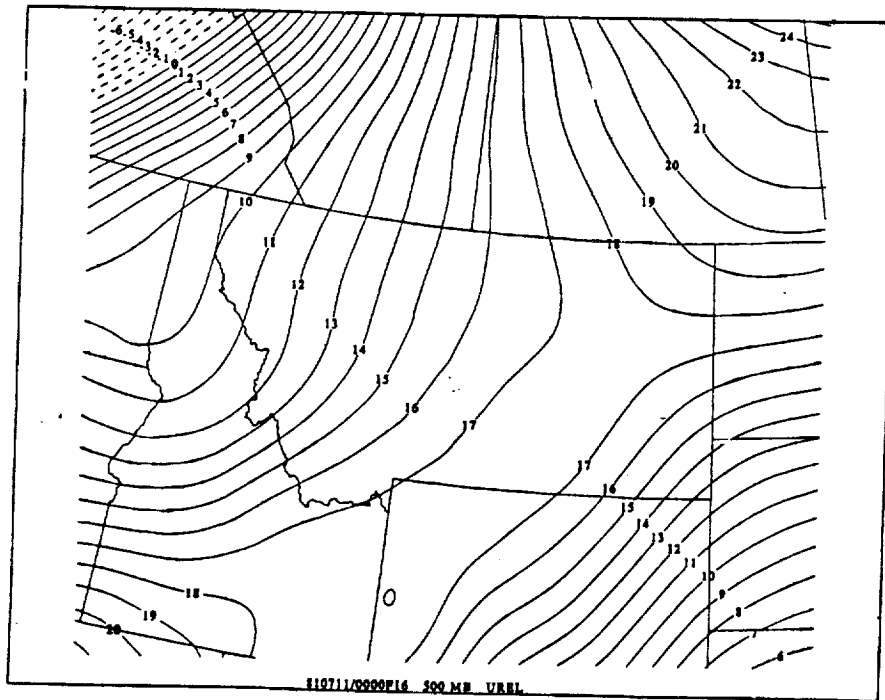
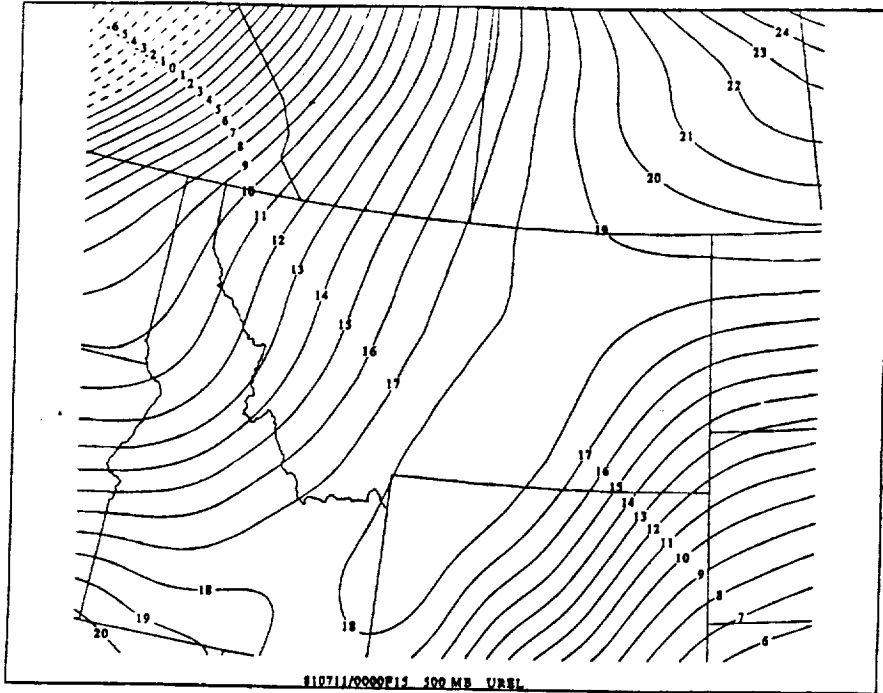


7D



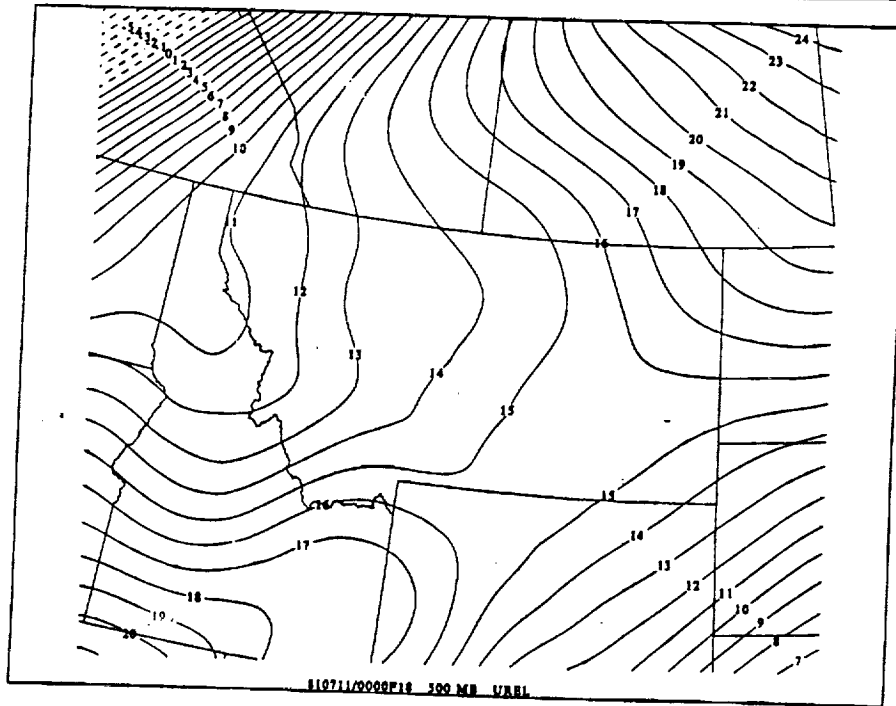
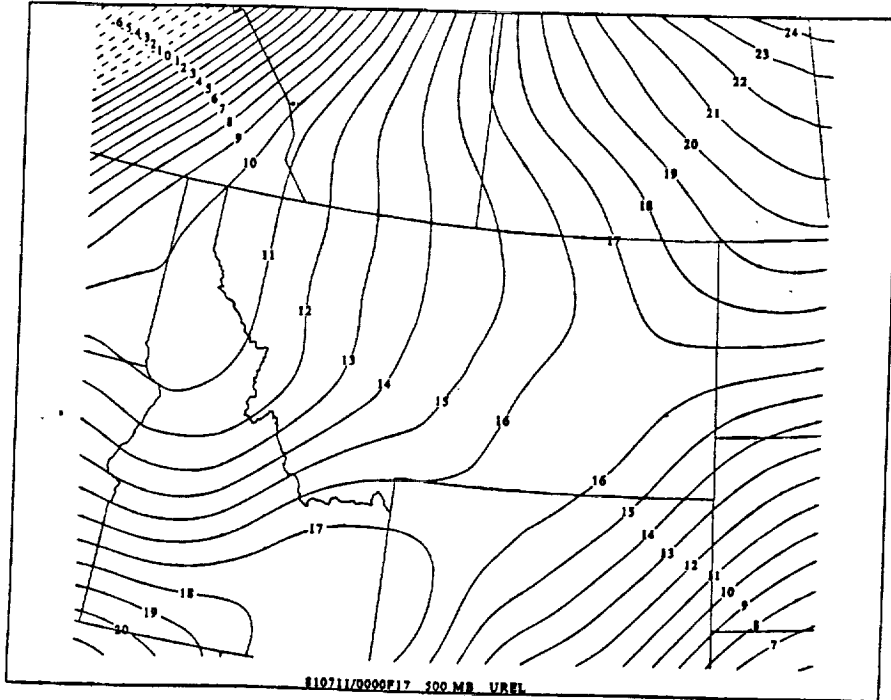
**7D**



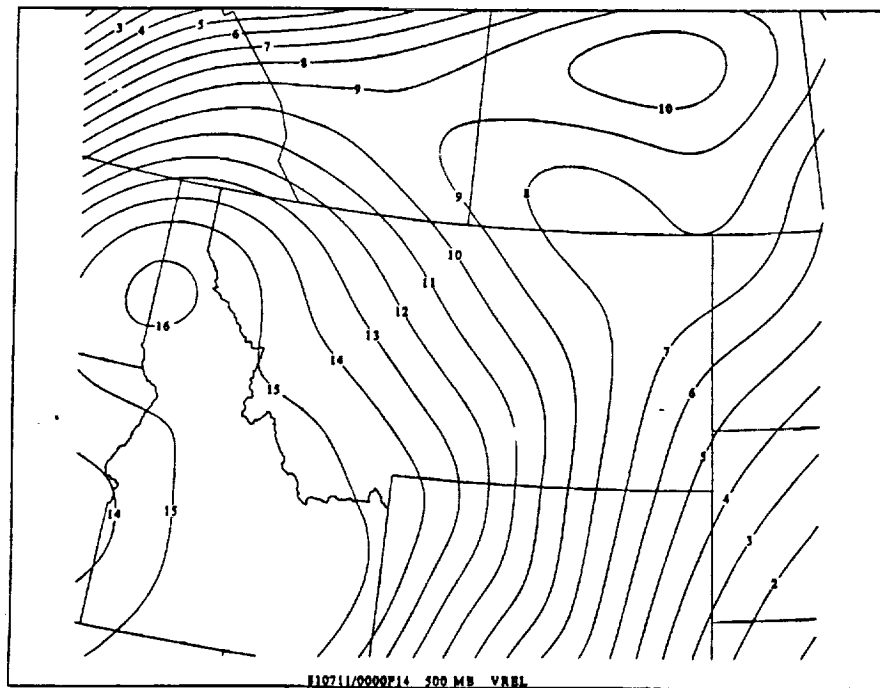
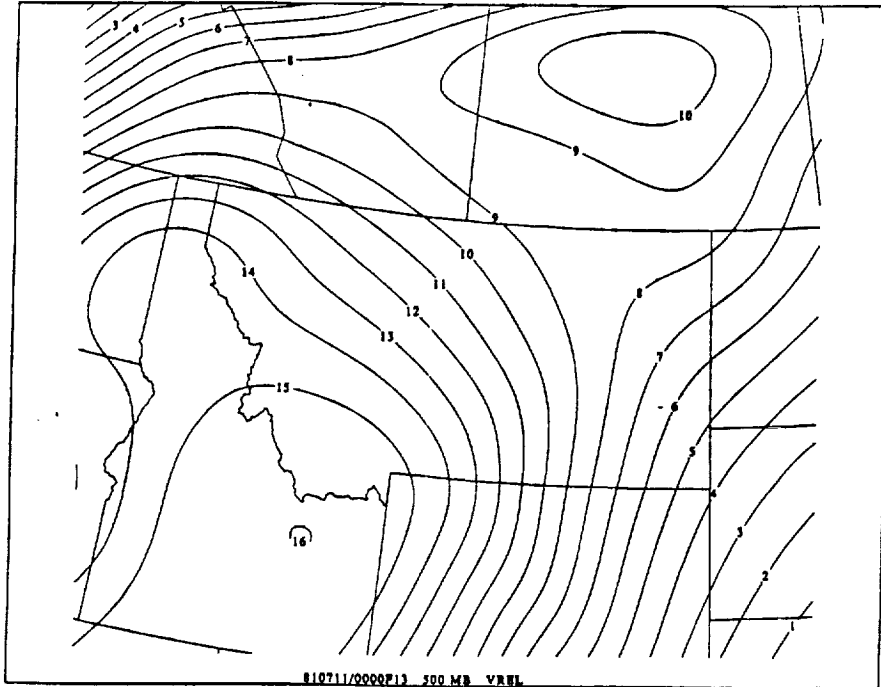


**7E**

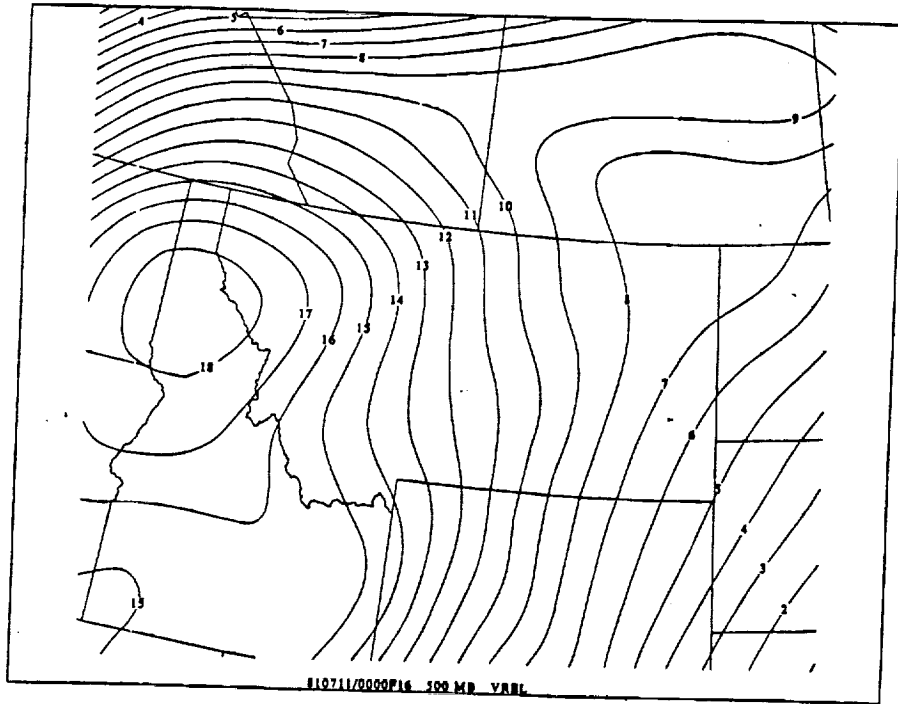
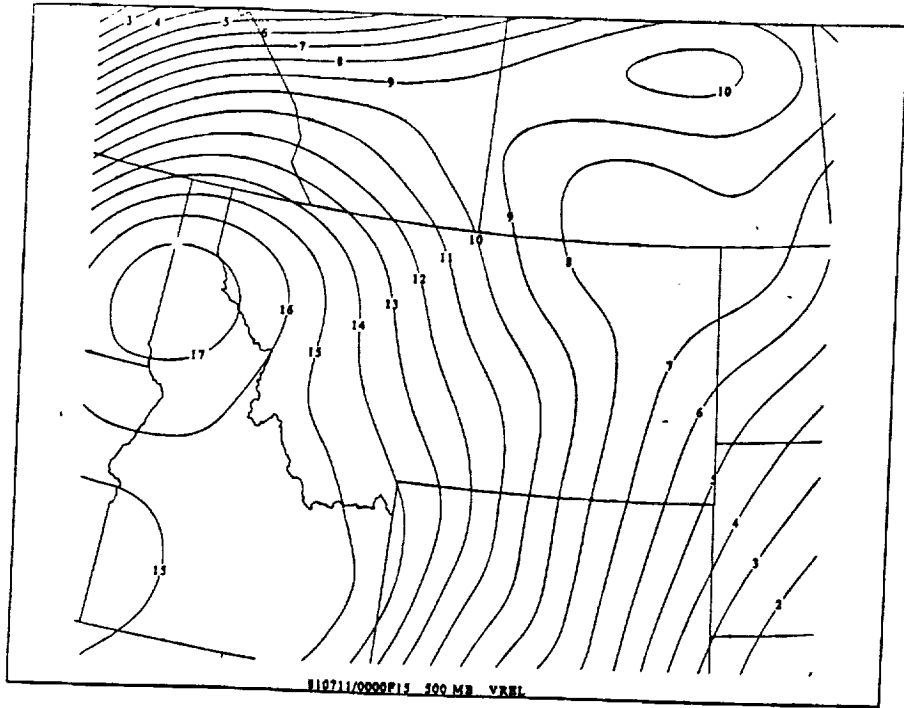




7E

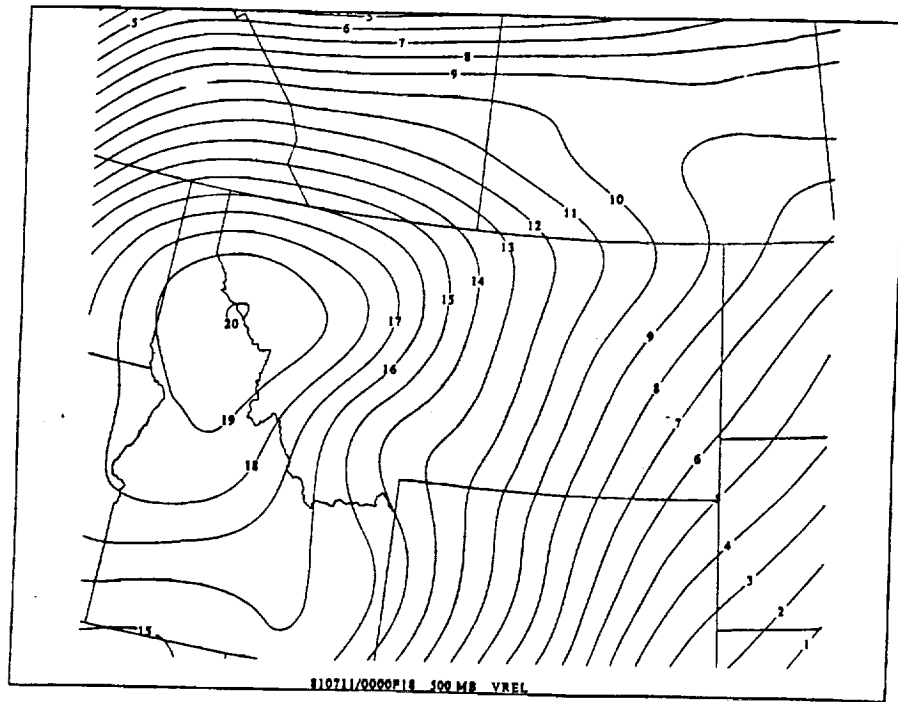
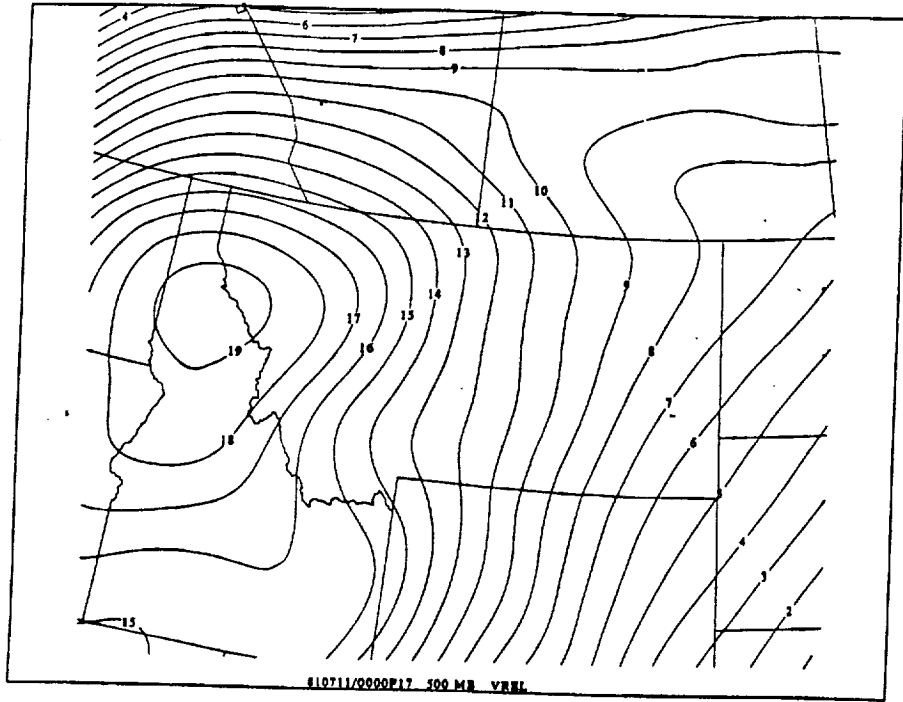


**7F**

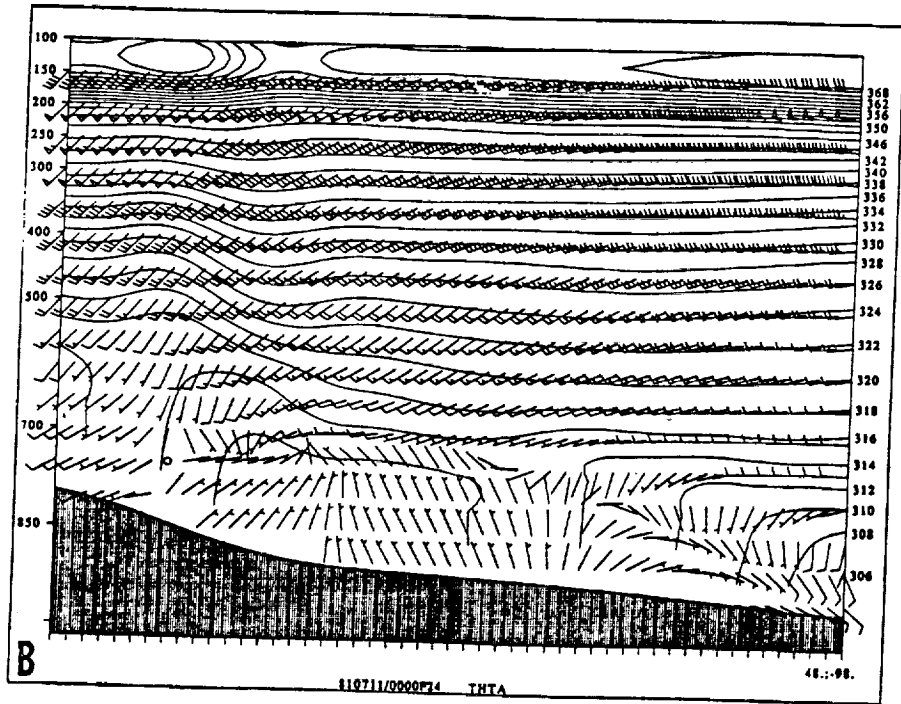
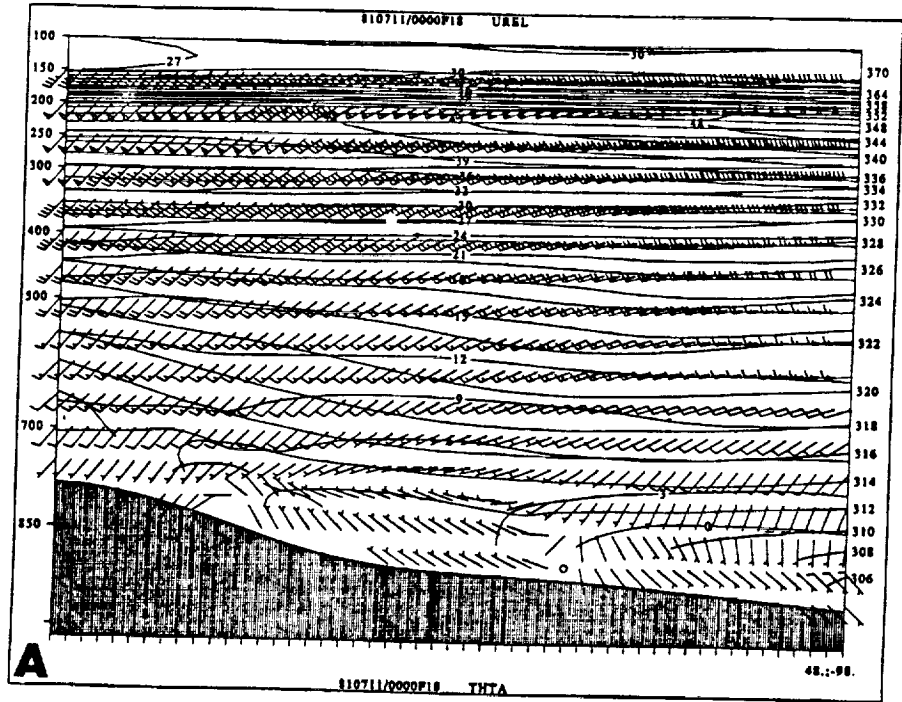


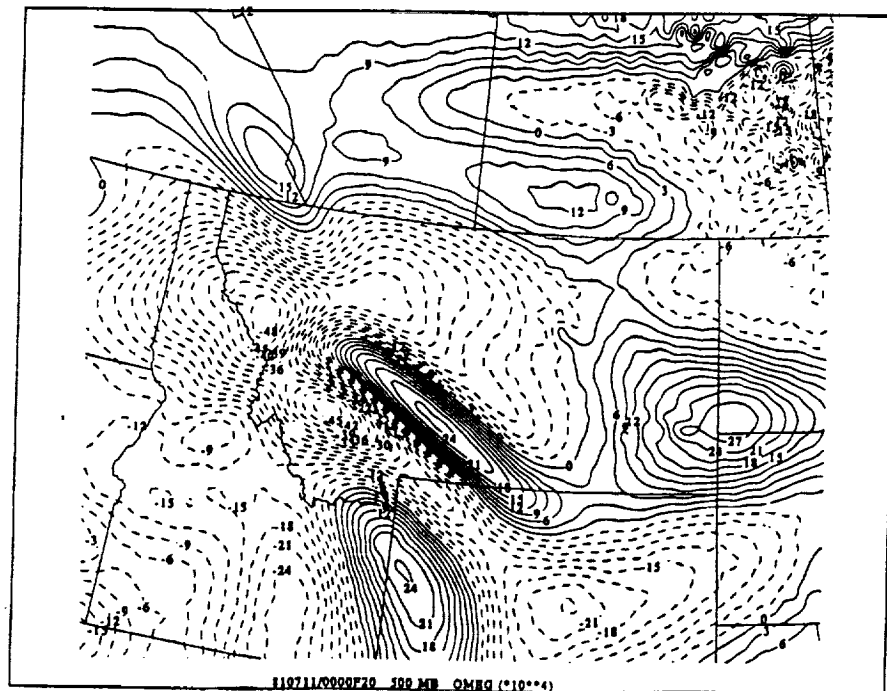
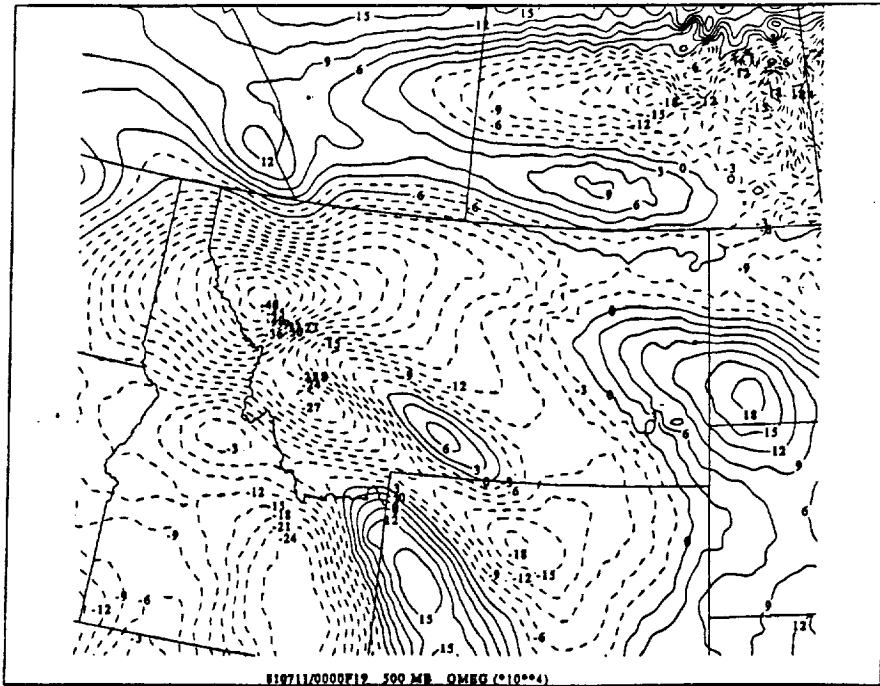
7F

-

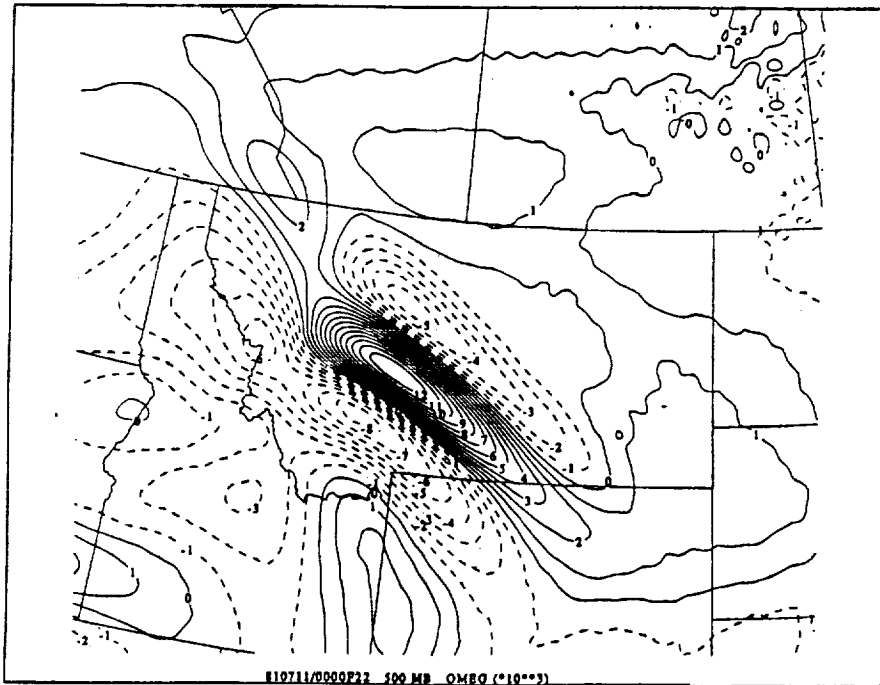
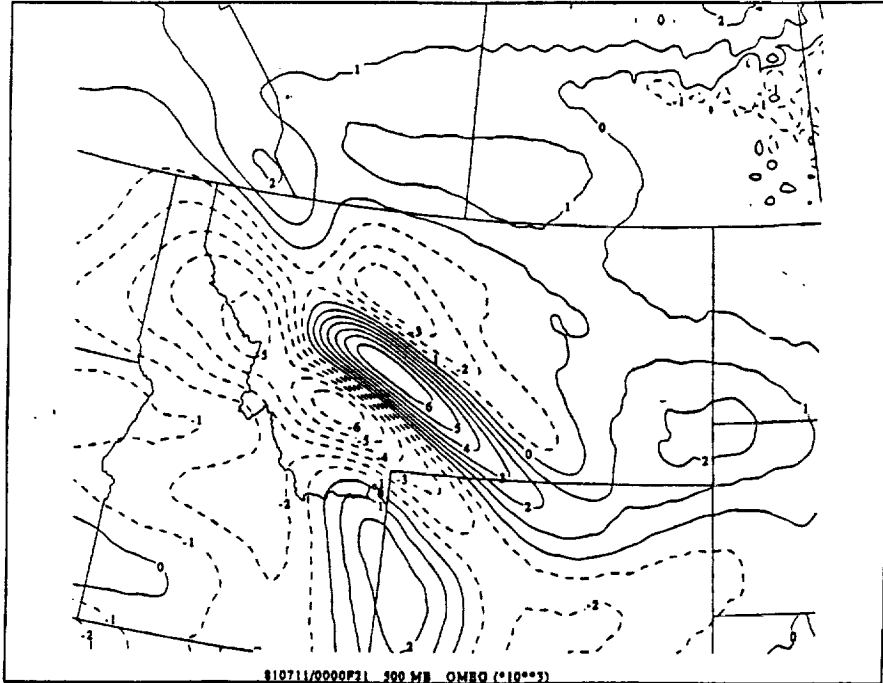


7F  
—  
—

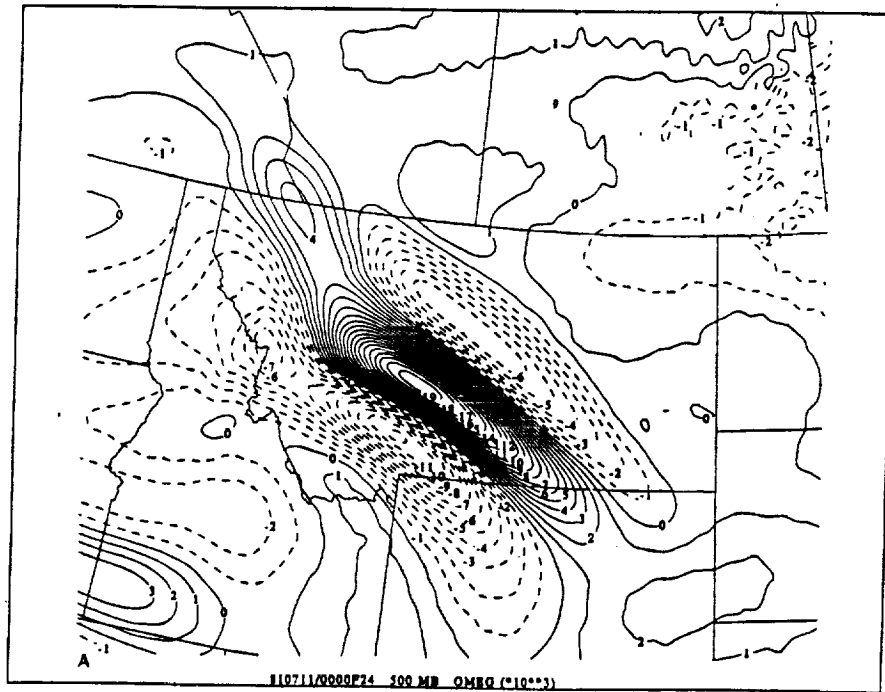
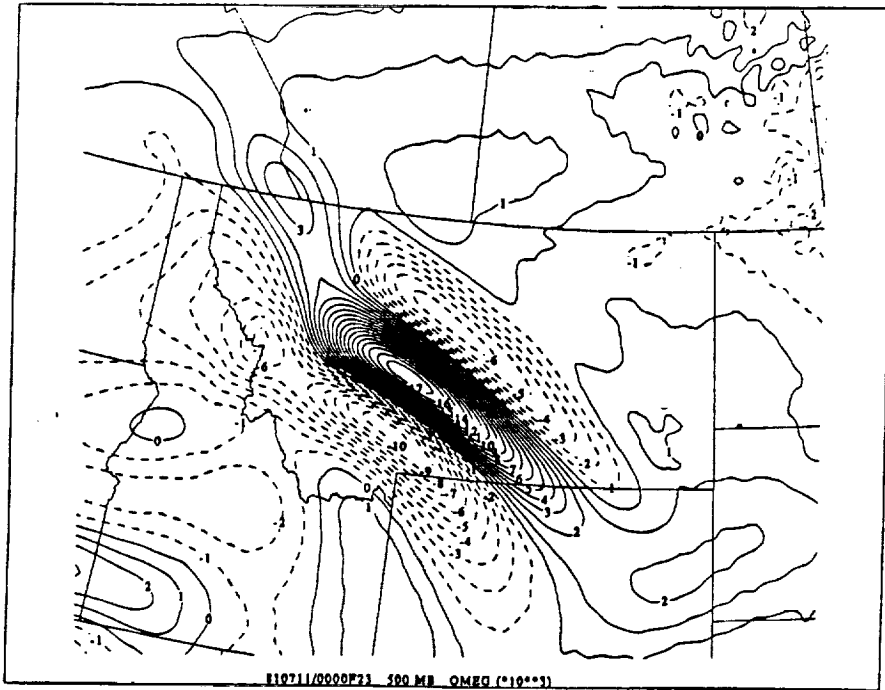




9A

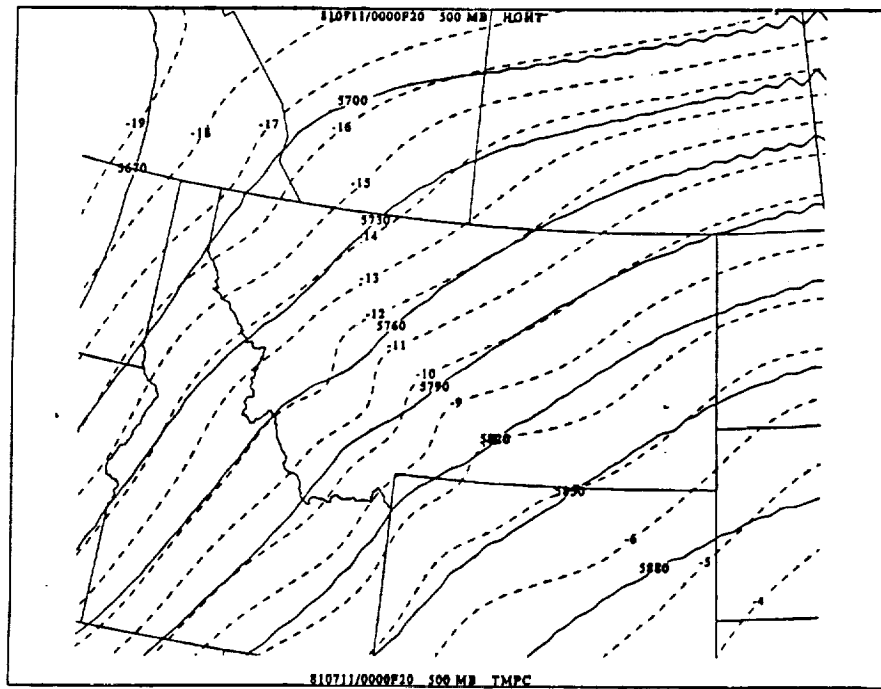
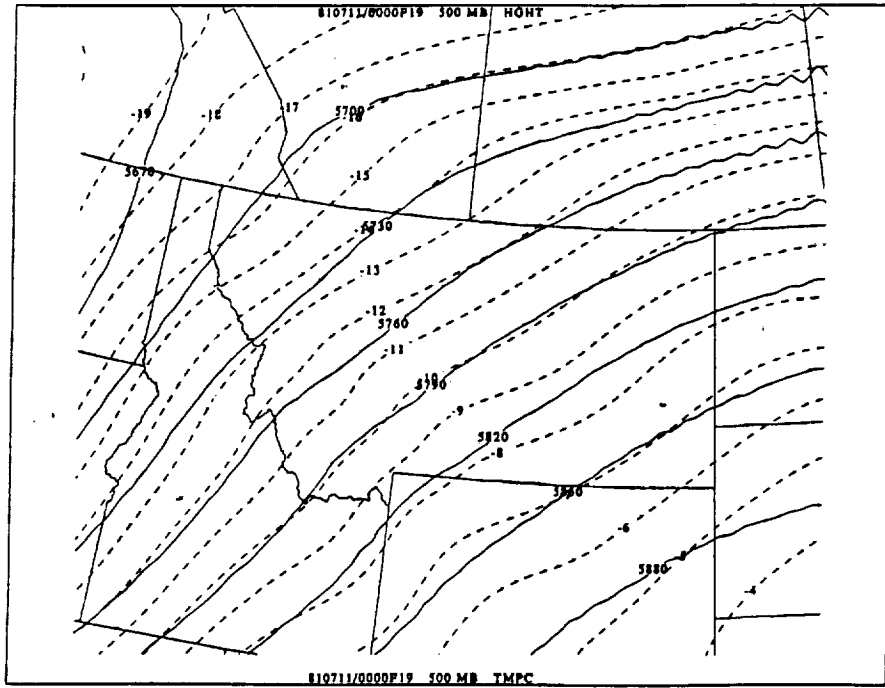


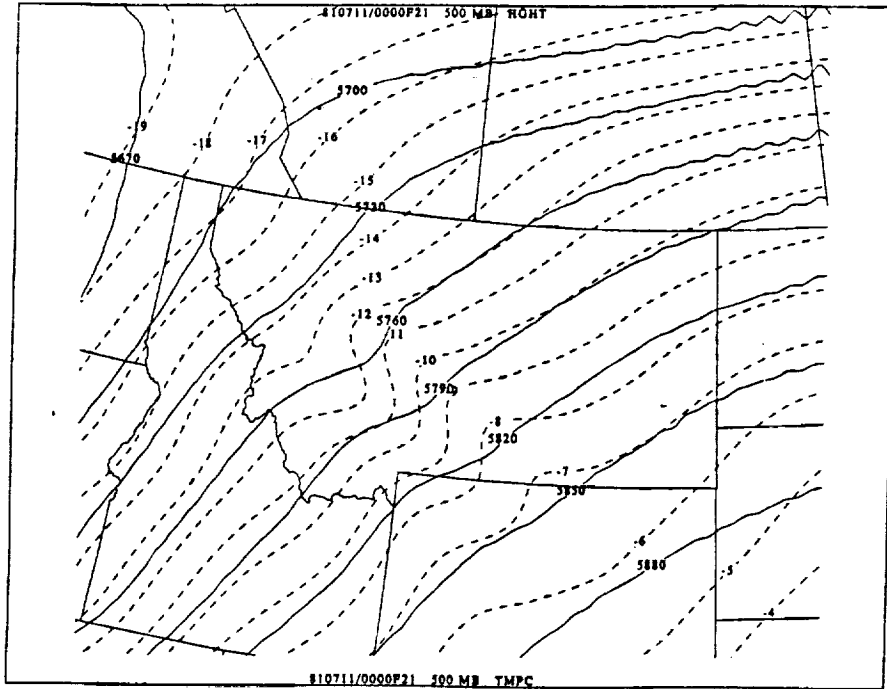
9A

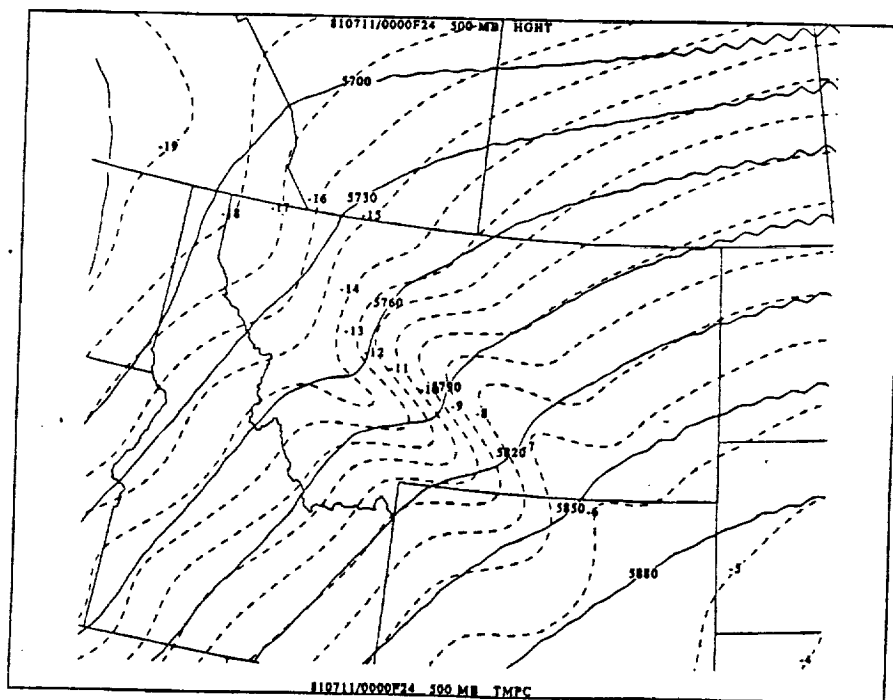
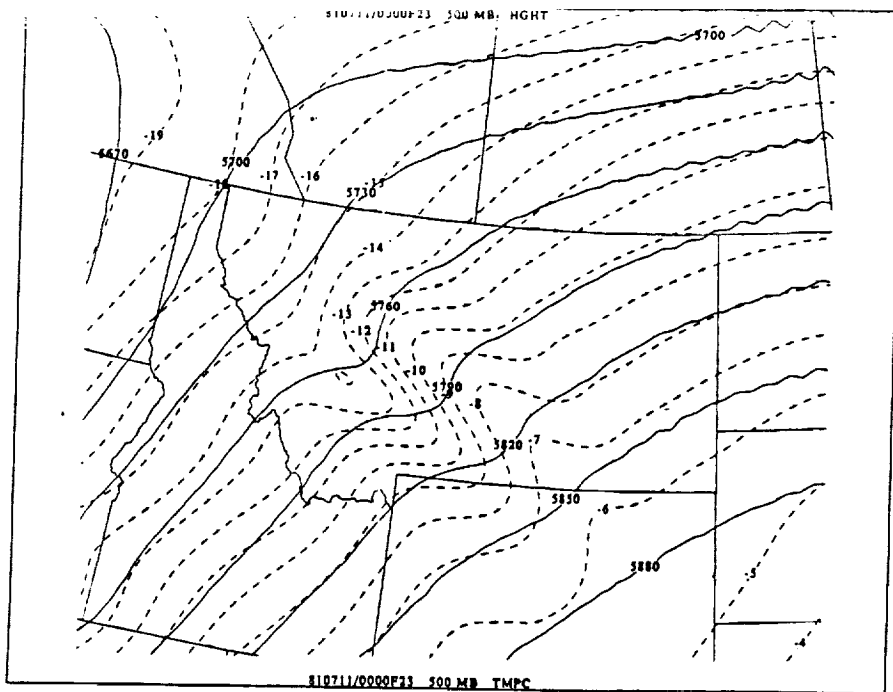


**9A**

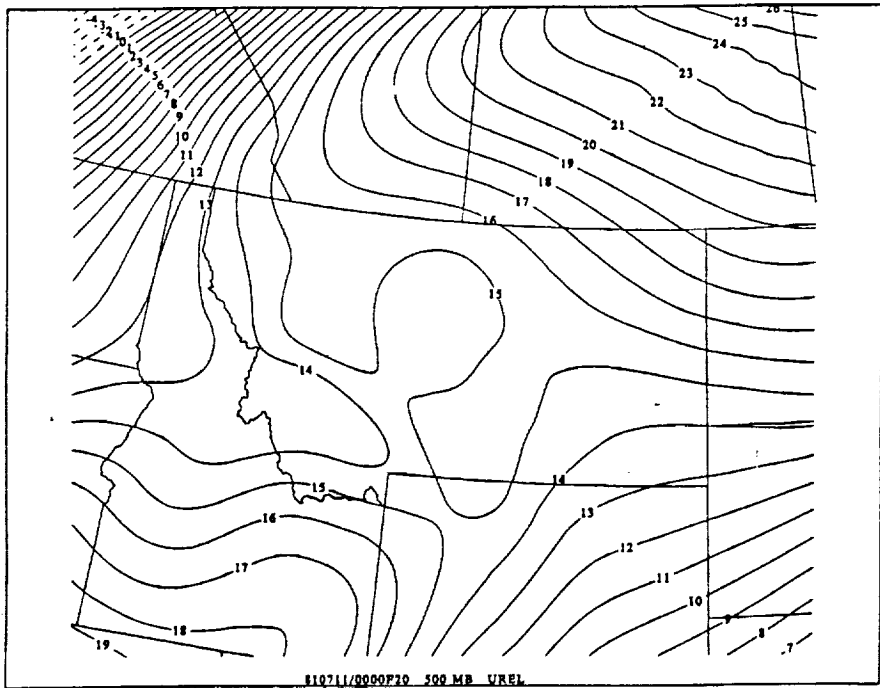
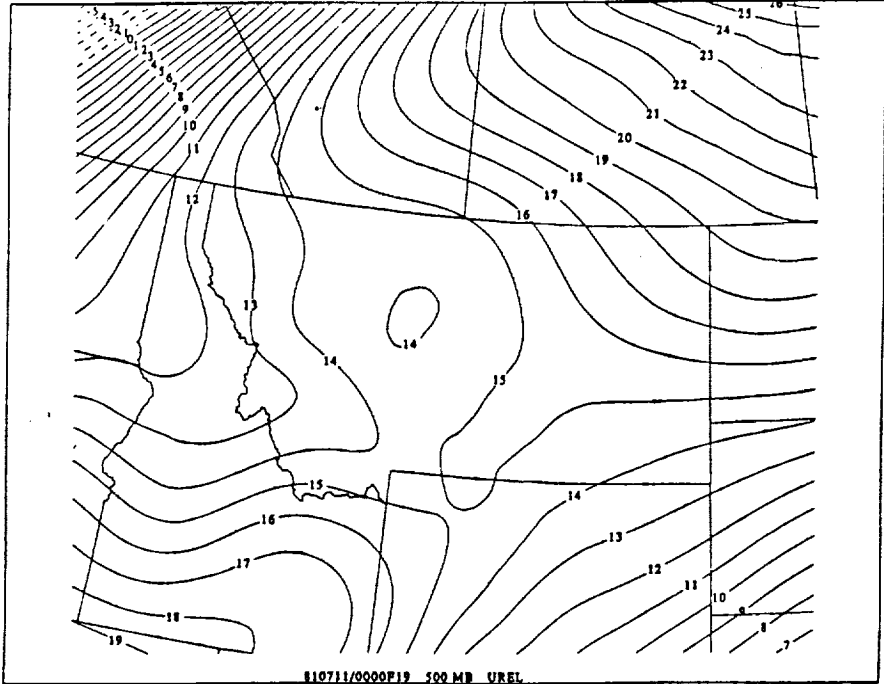




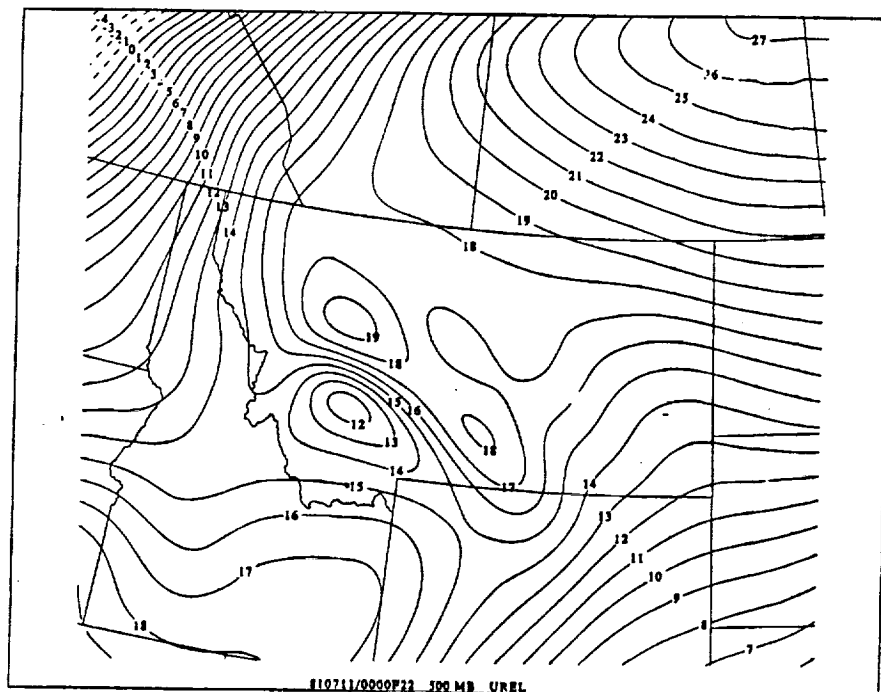
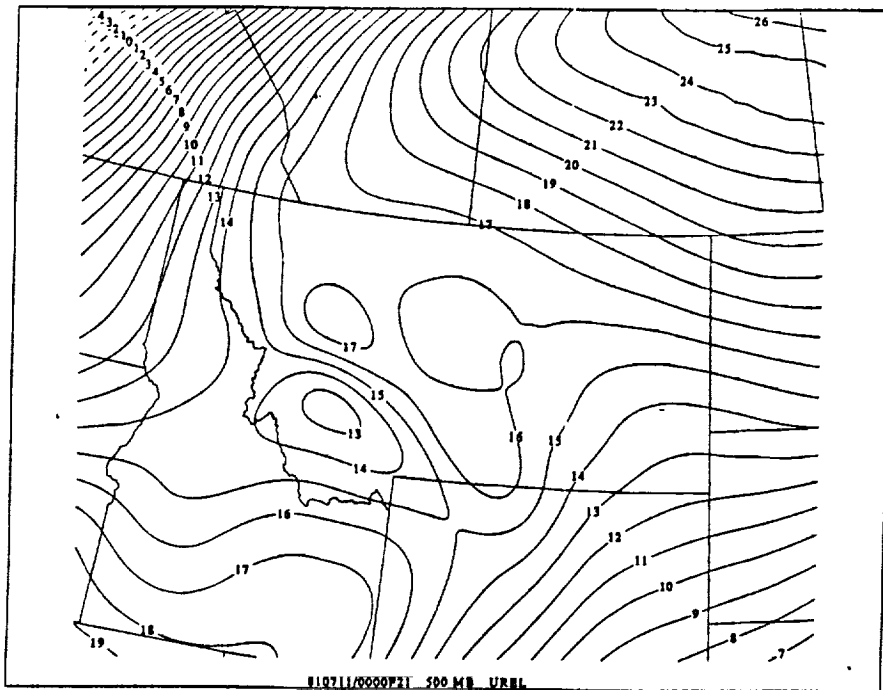


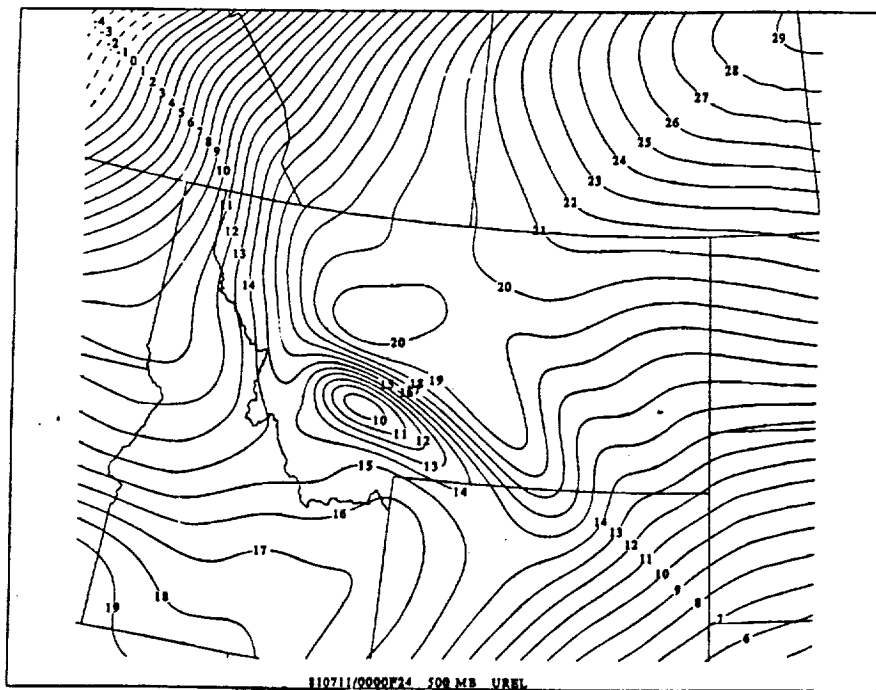
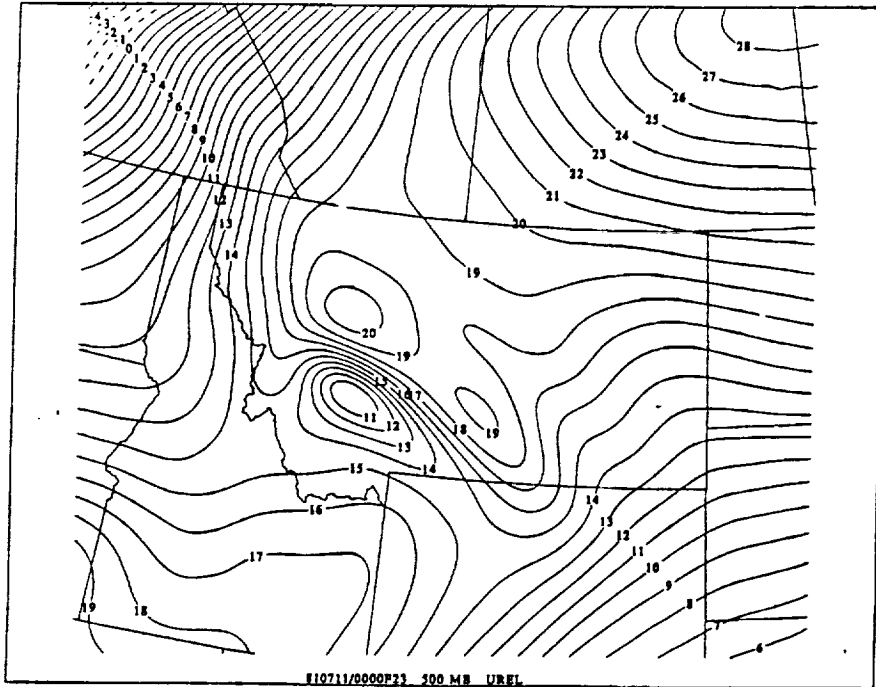


9B  
=

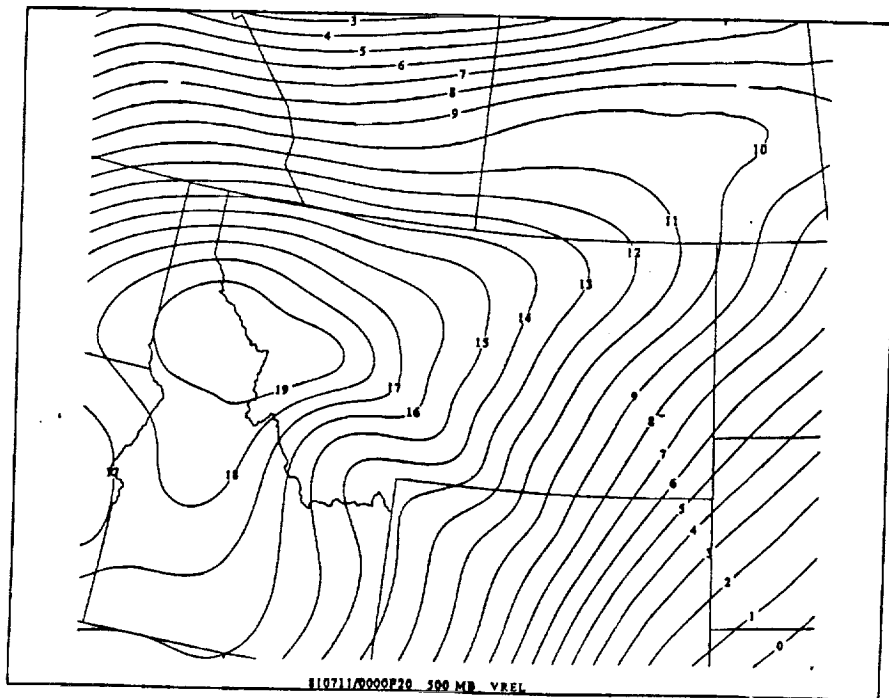
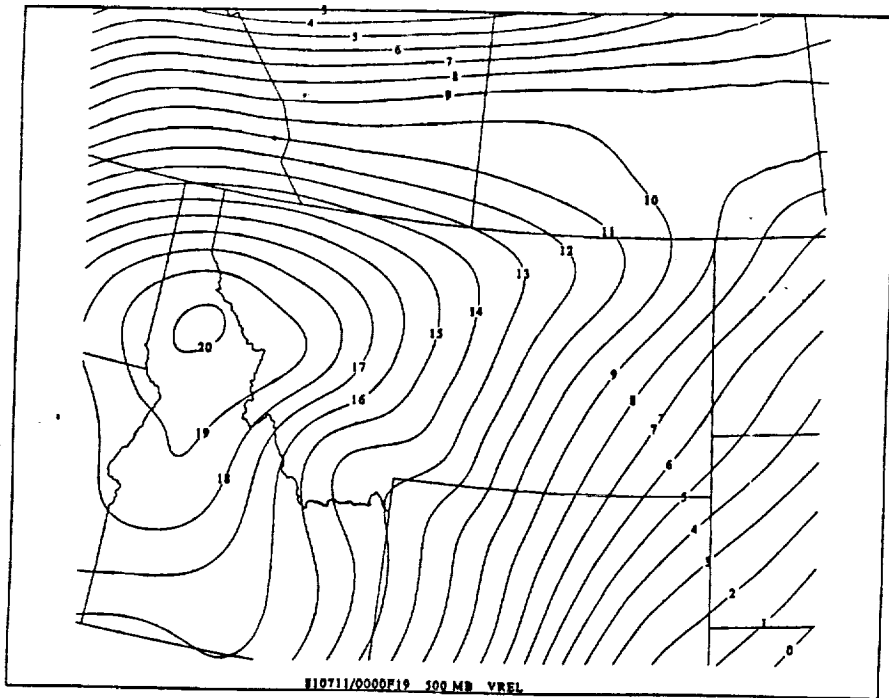


9C

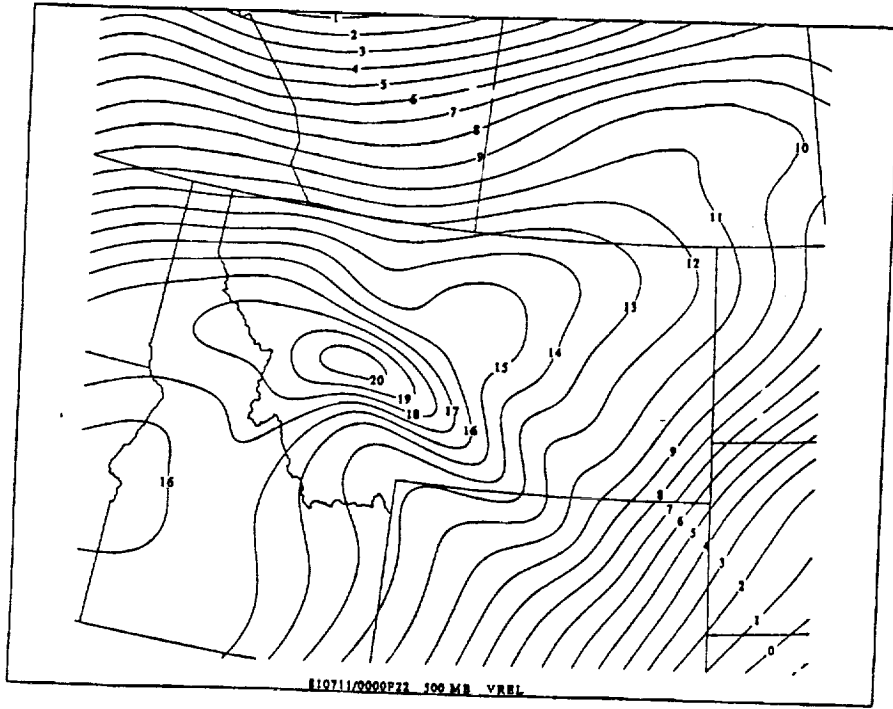
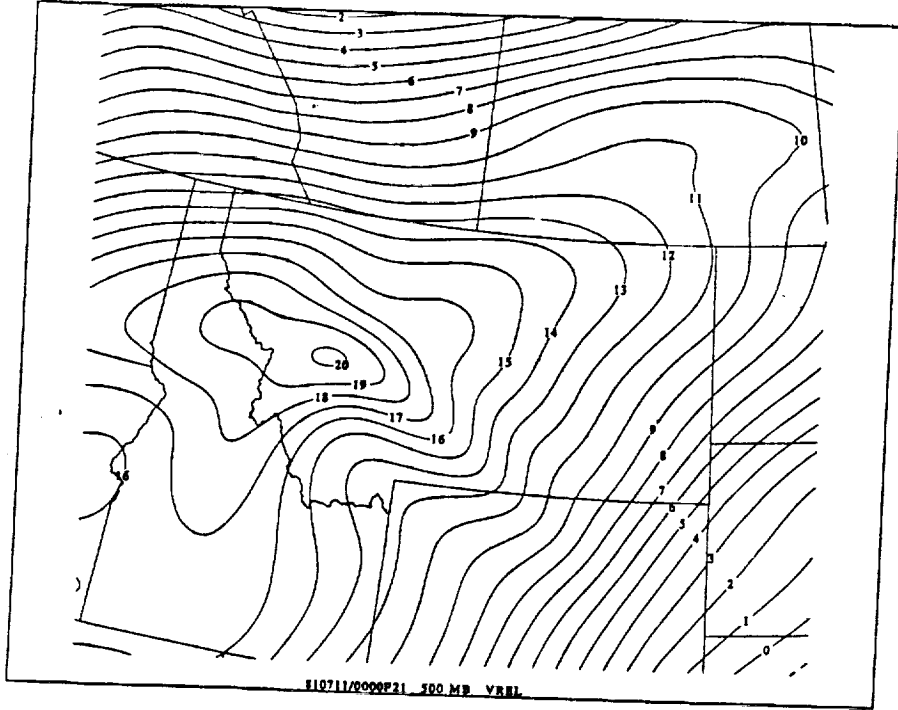




9C  
||

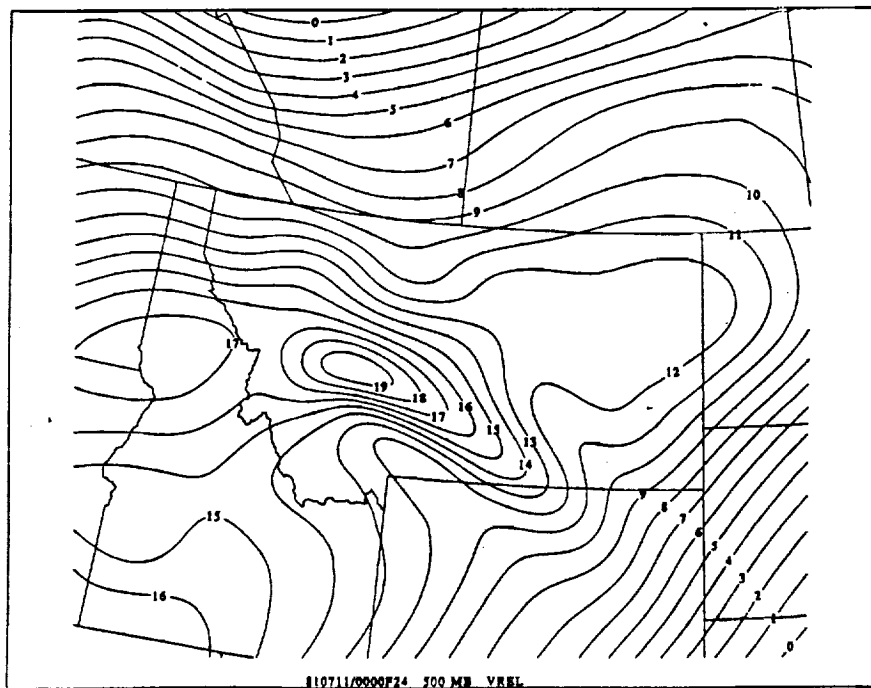
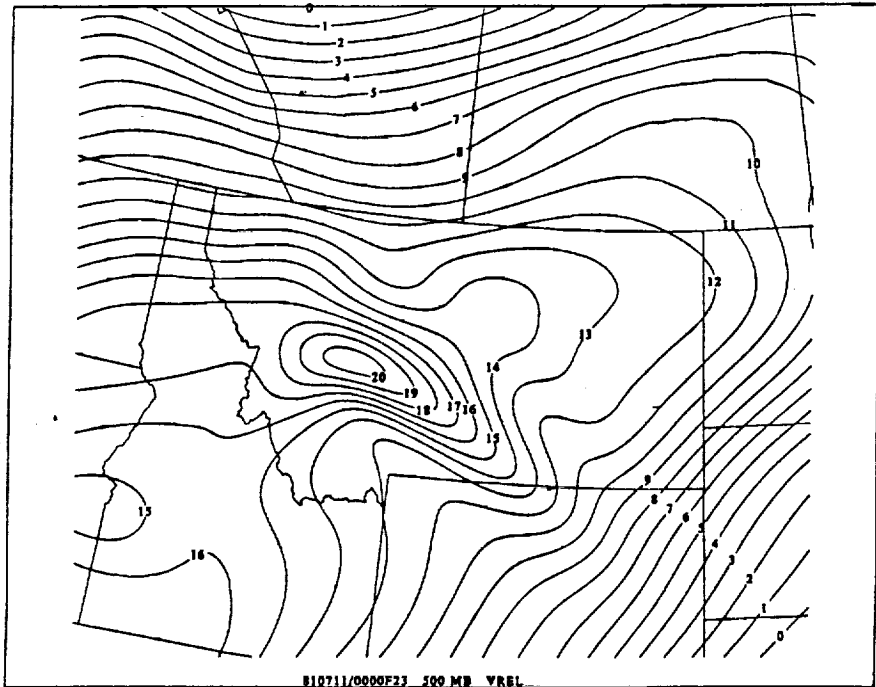


9D

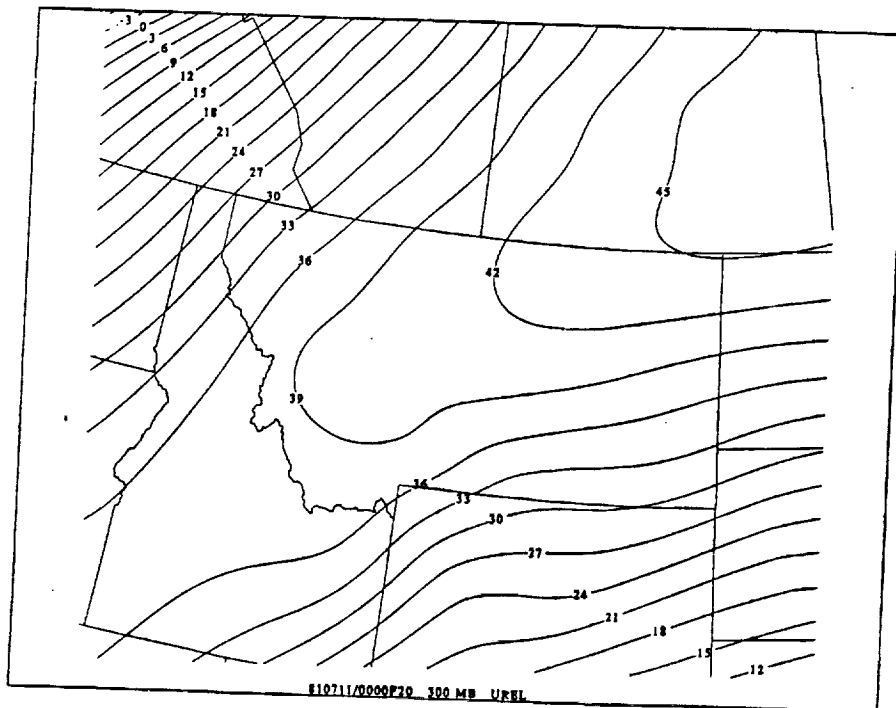
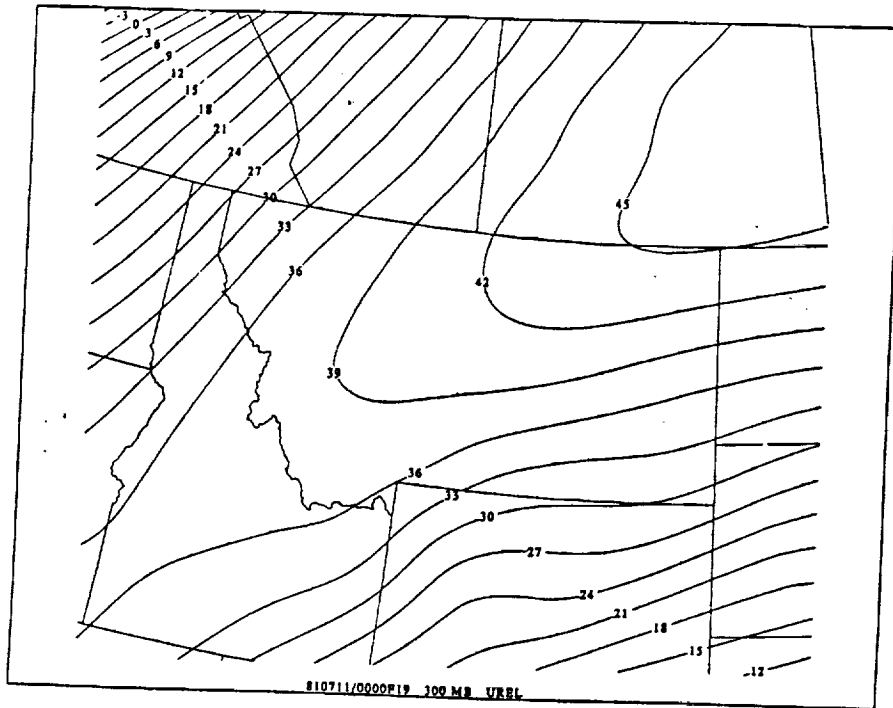


**9D**

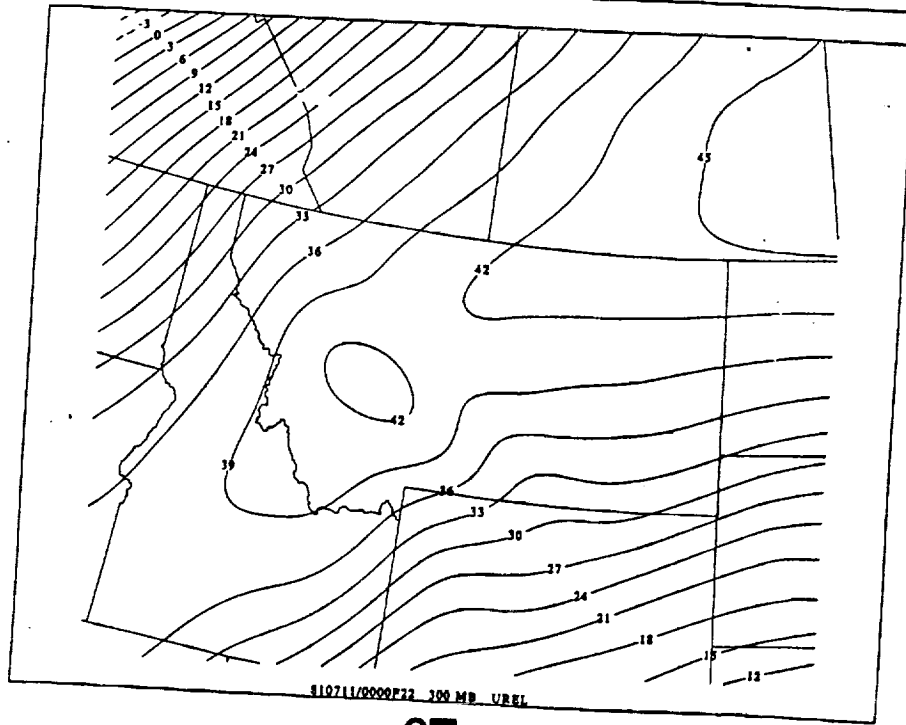
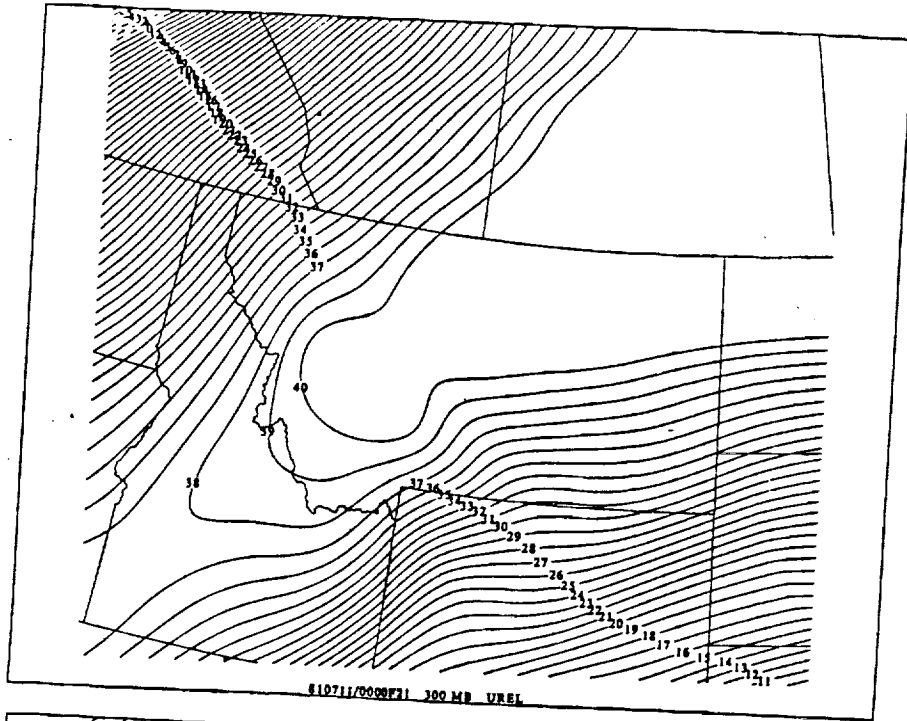




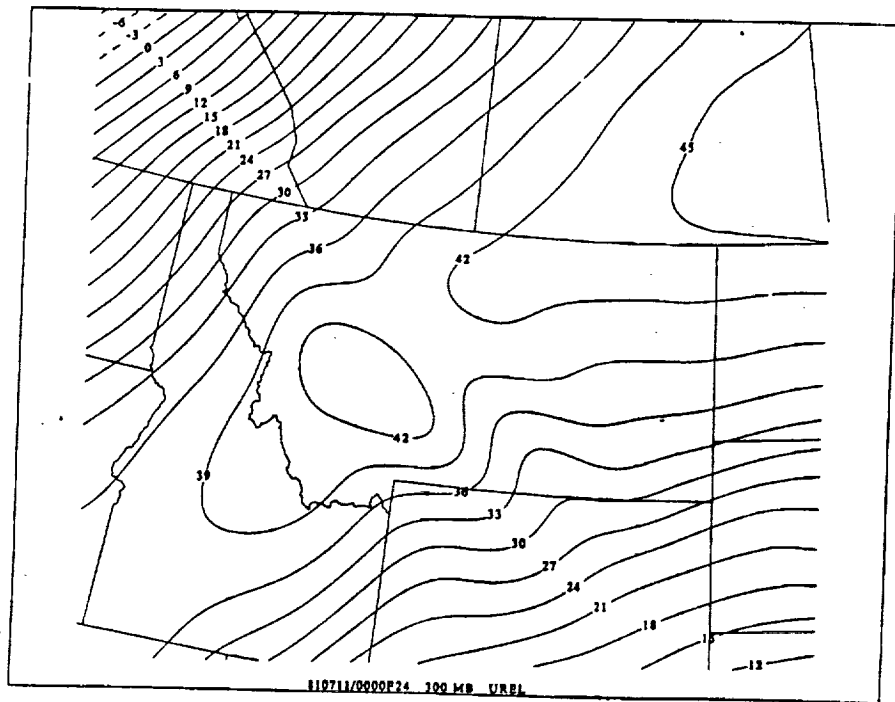
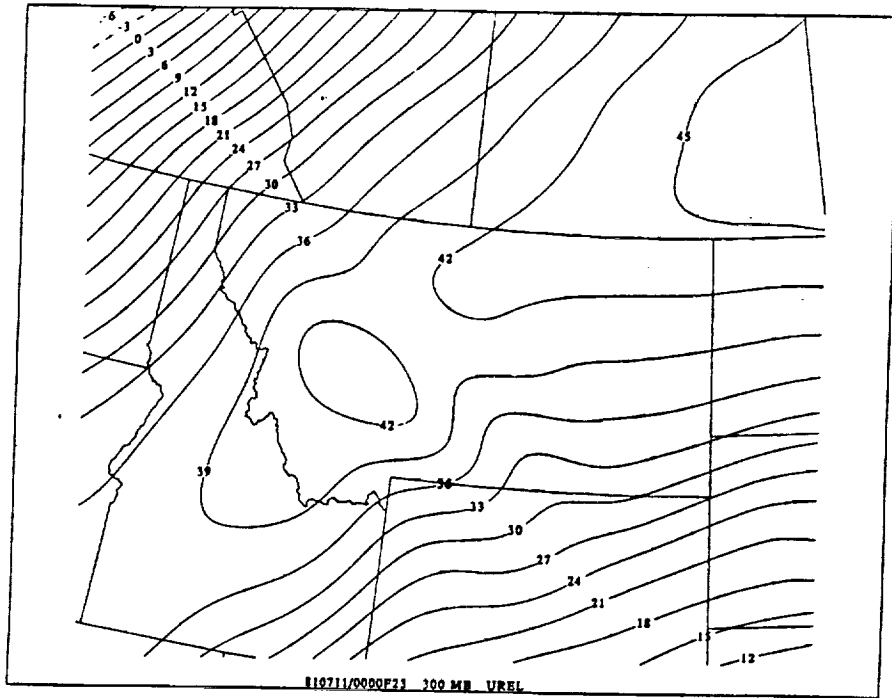
**9D**  
 ==



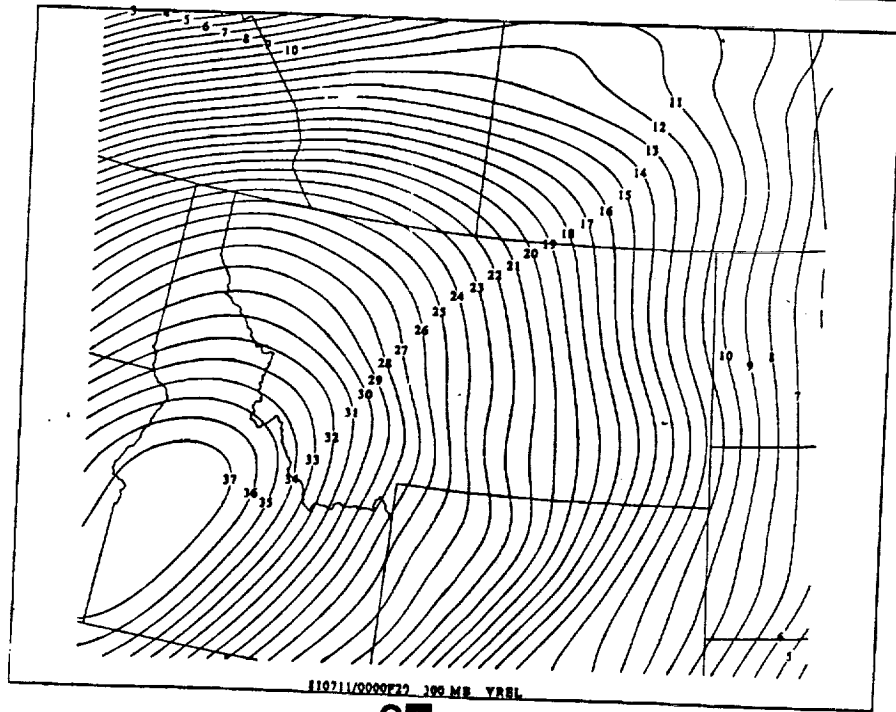
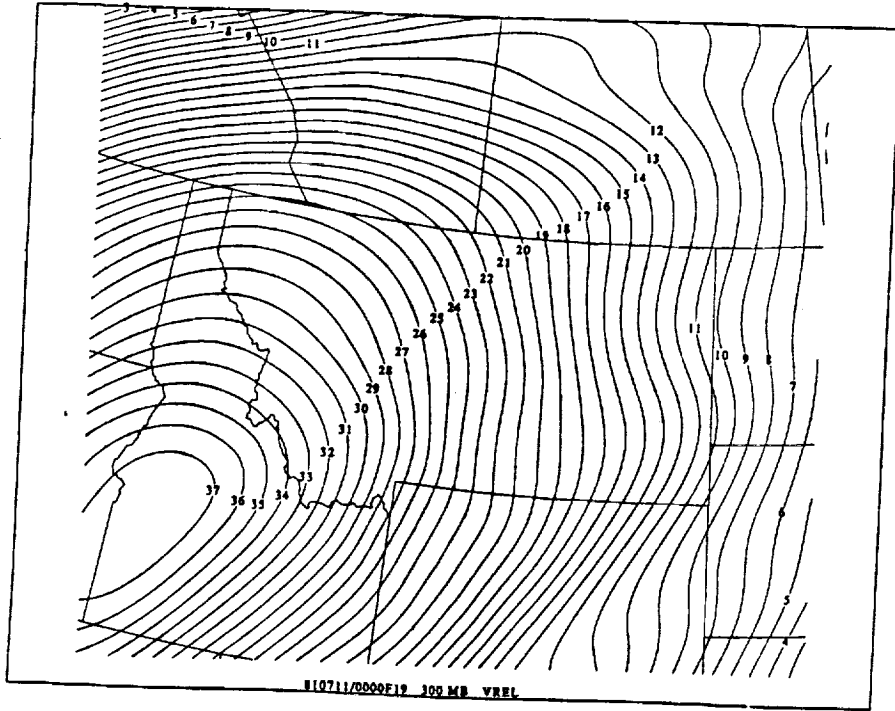
9E



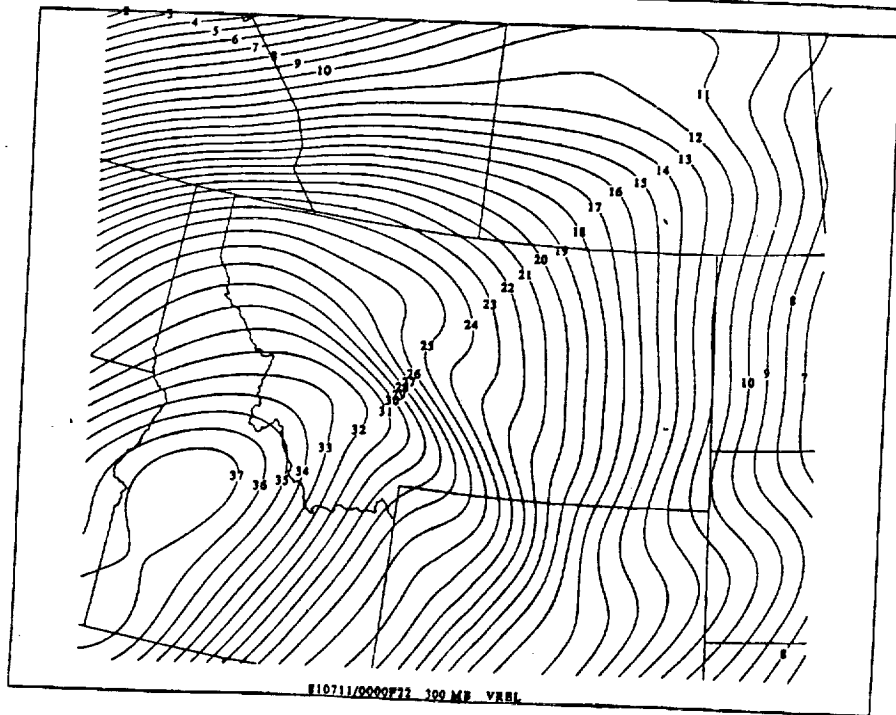
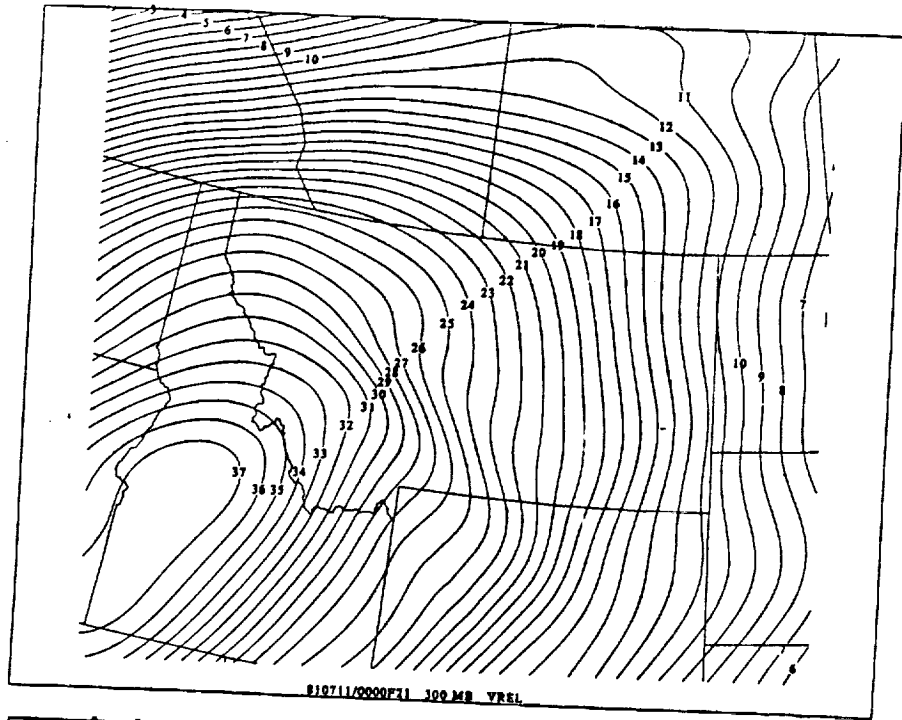
9E



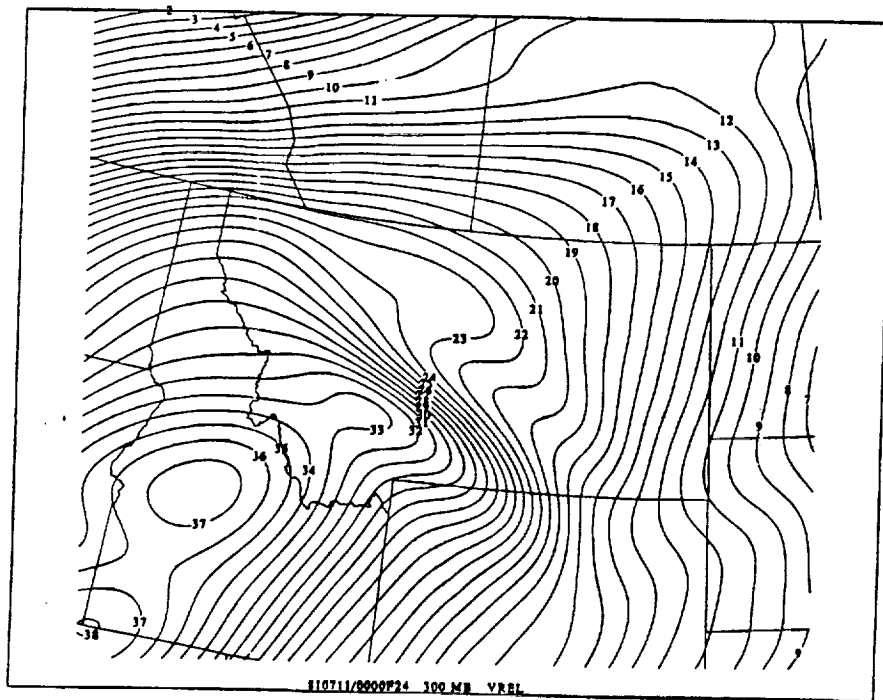
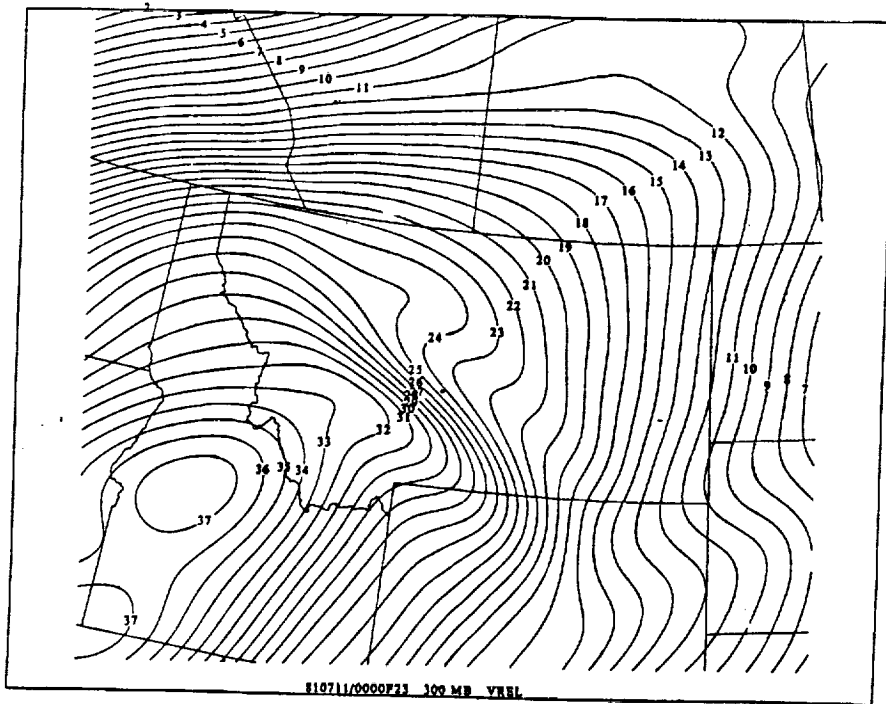
9E



9F

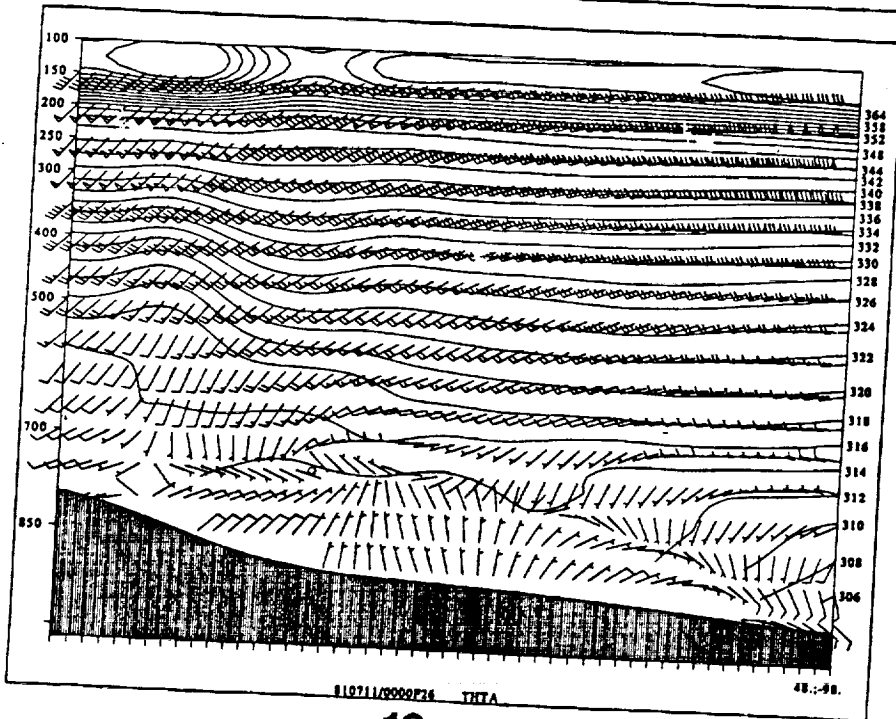
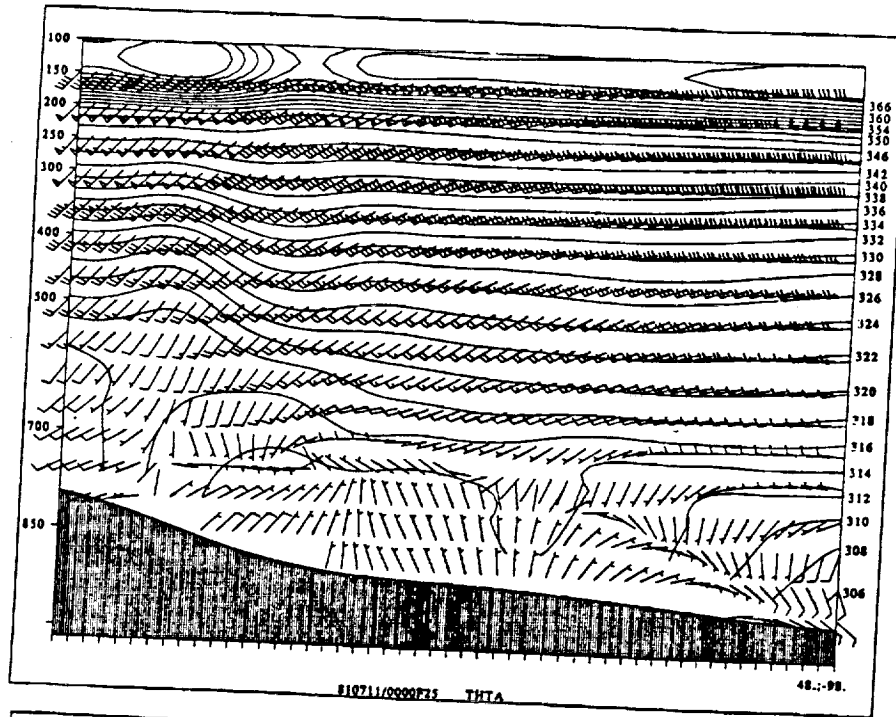


**9F**

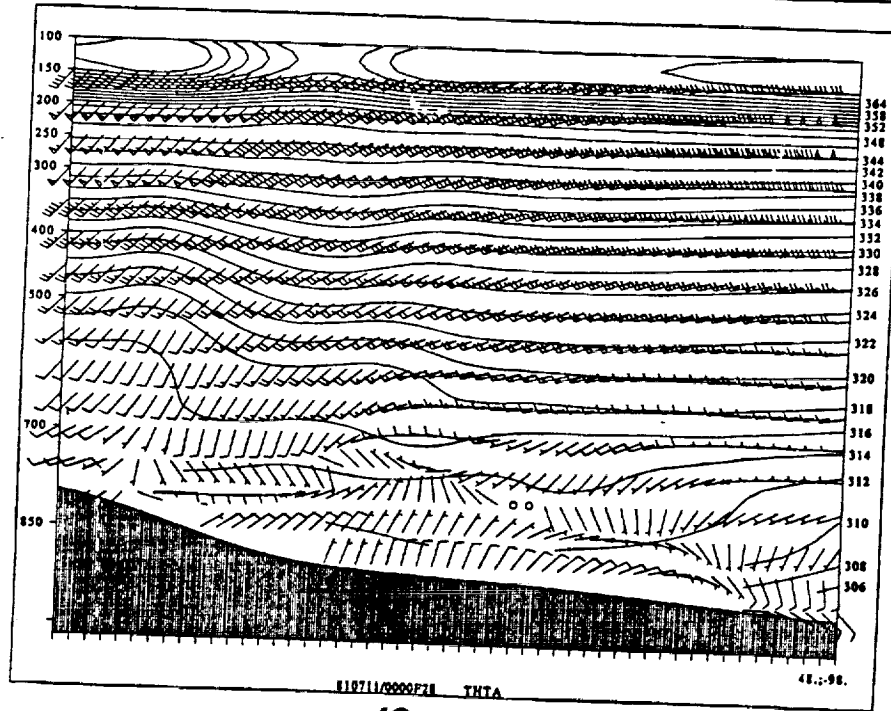
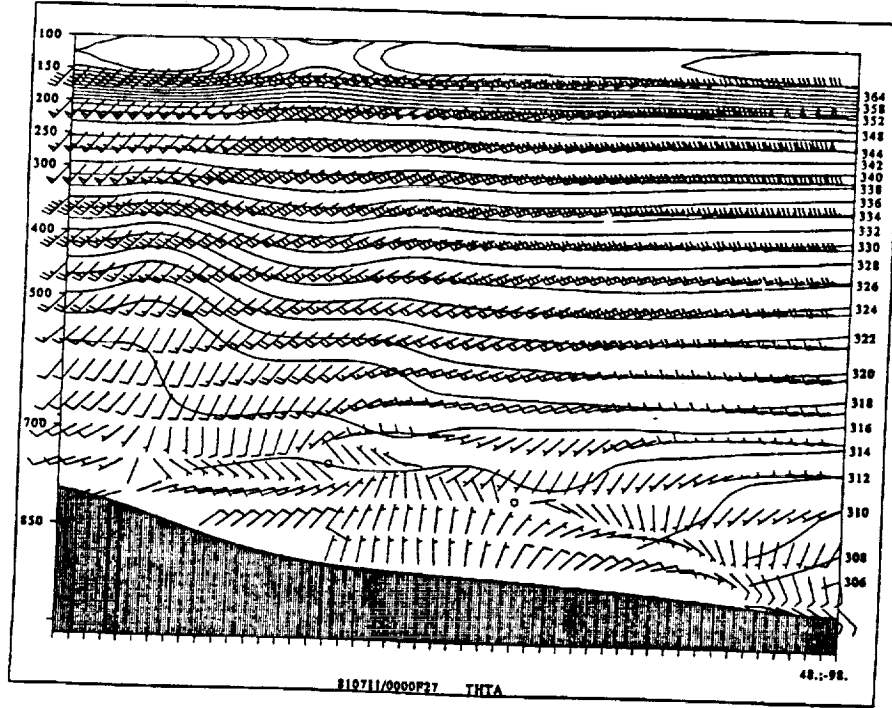


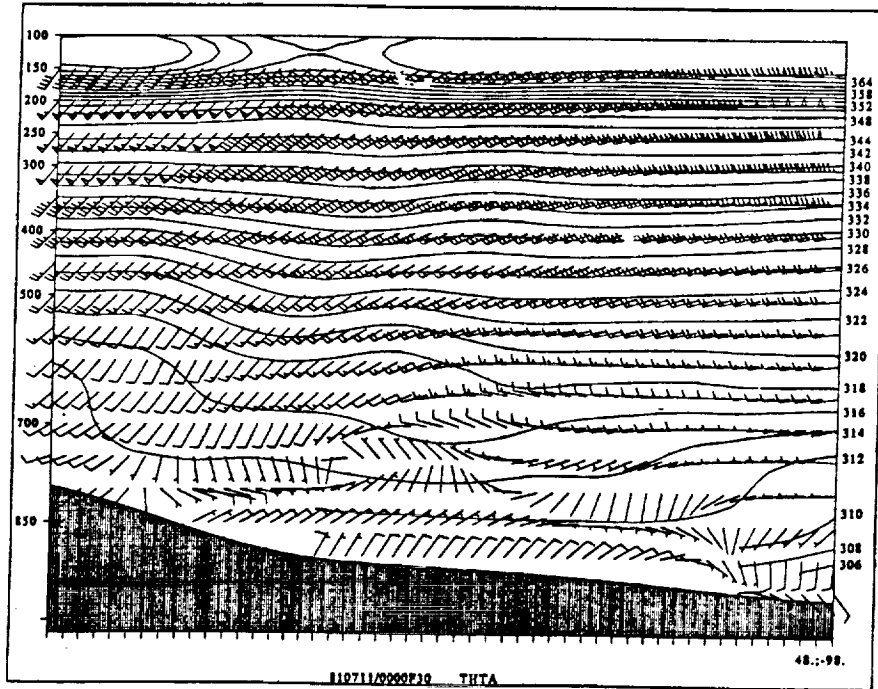
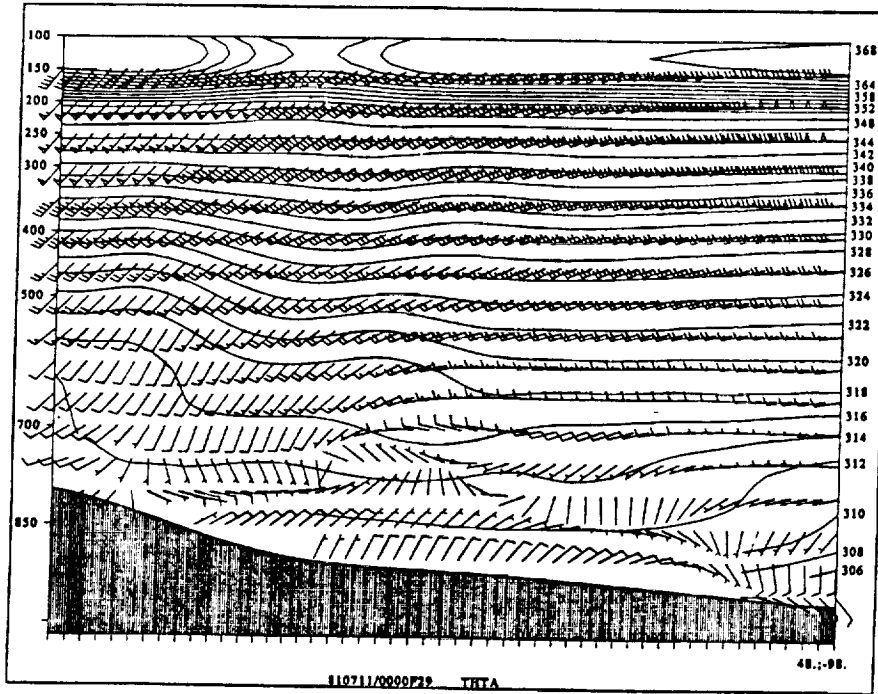
9F



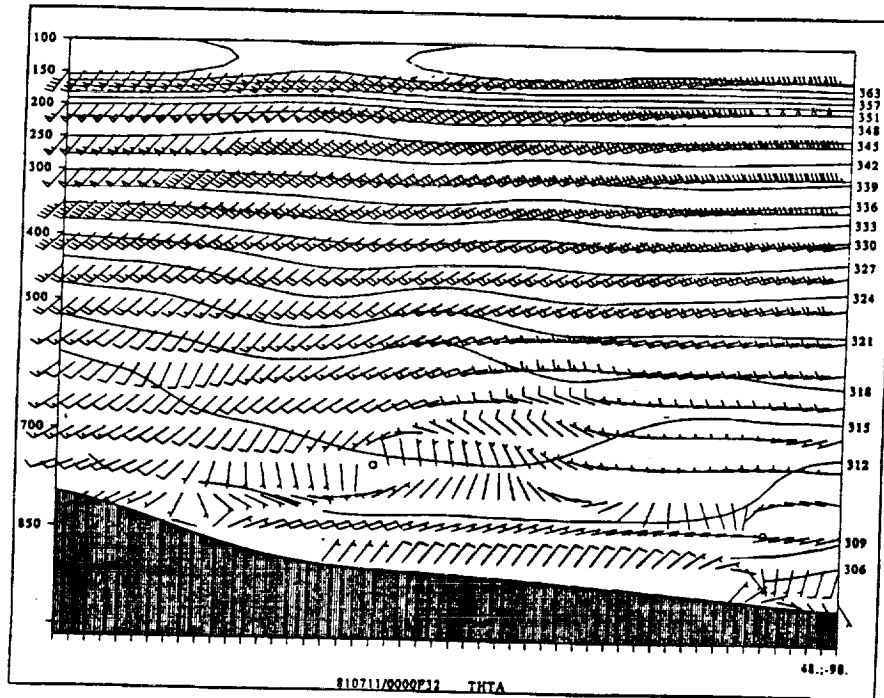
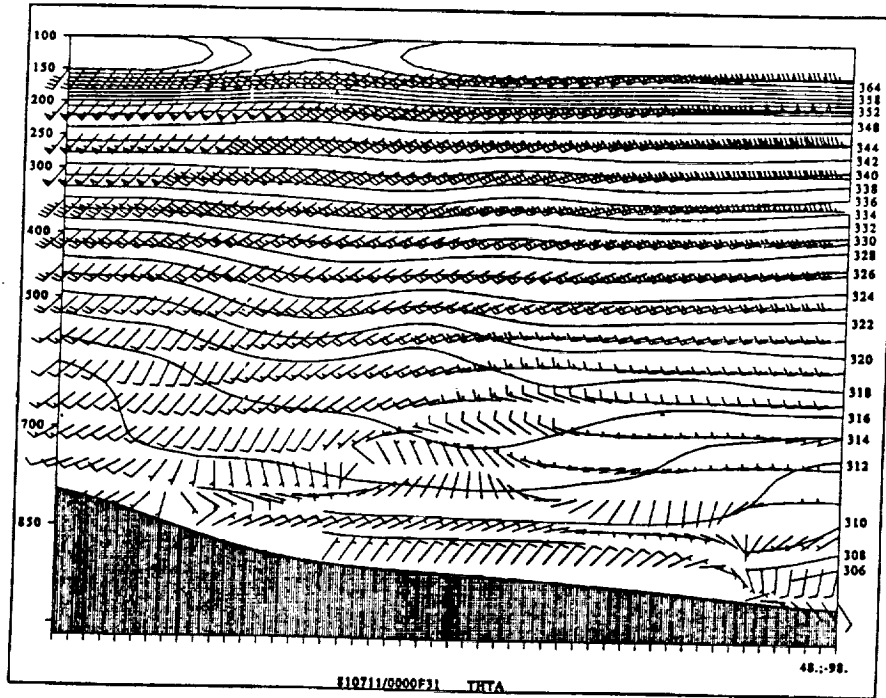


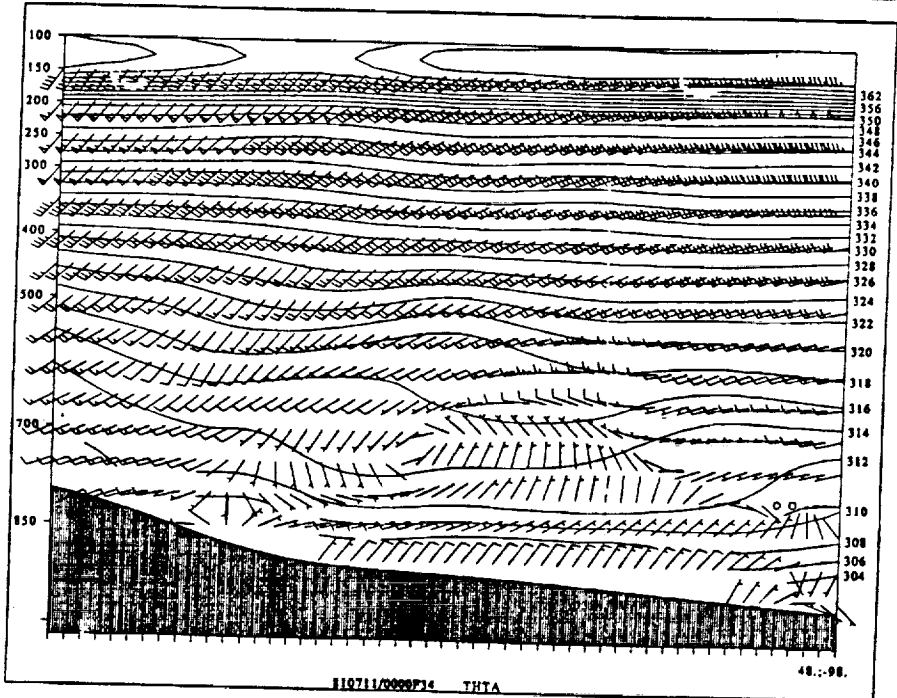
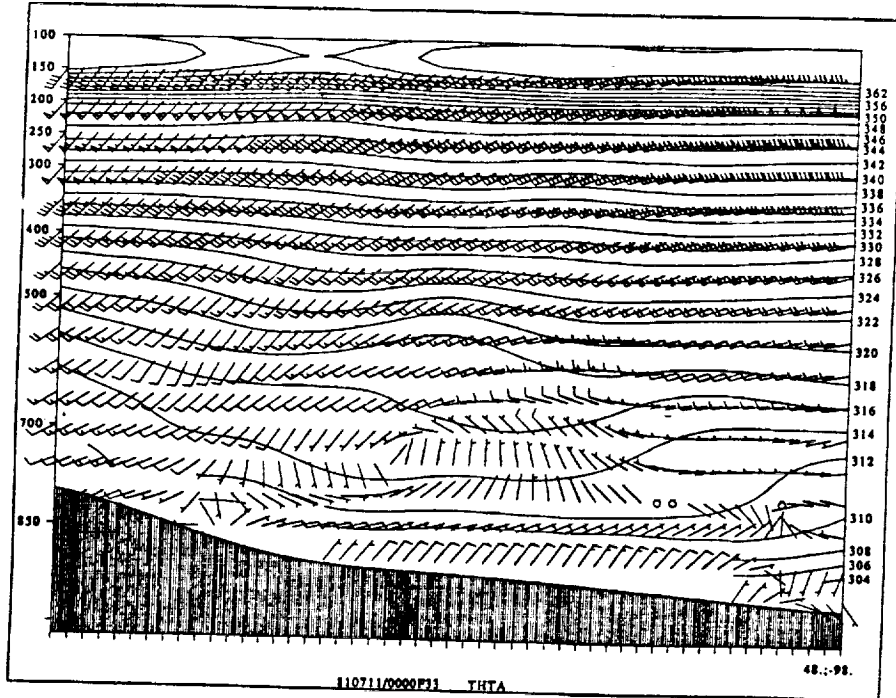




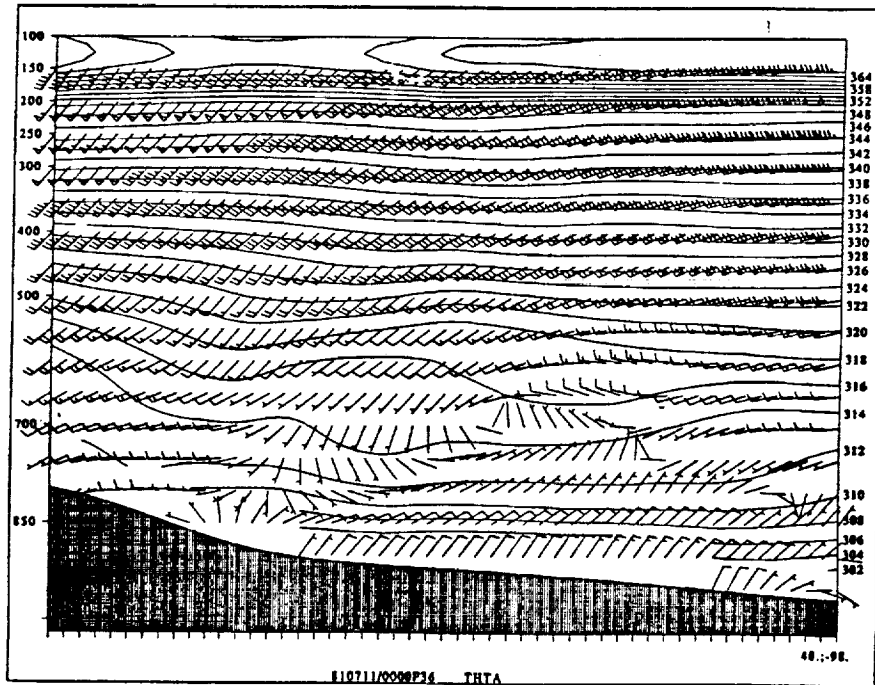
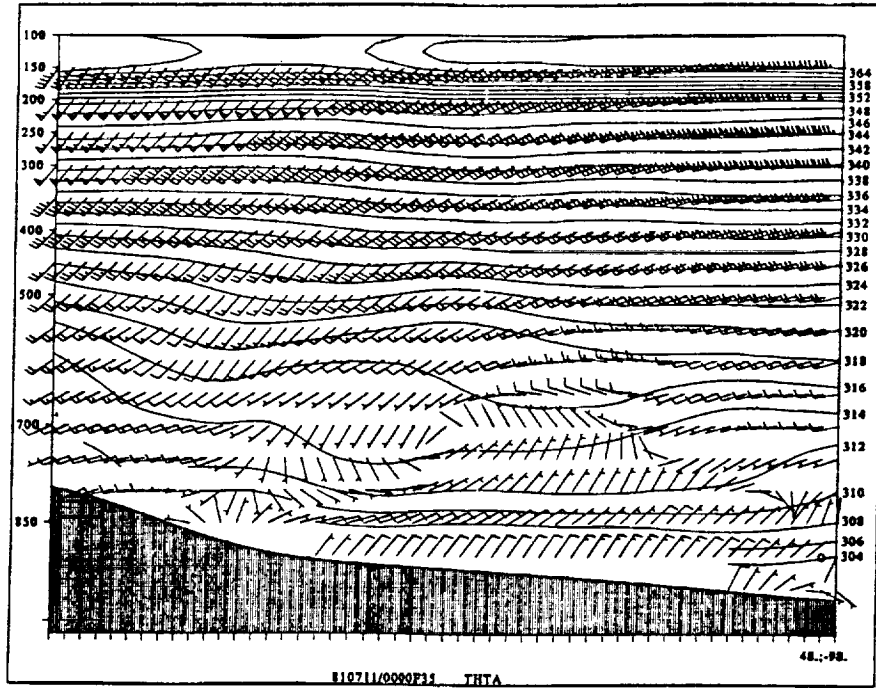


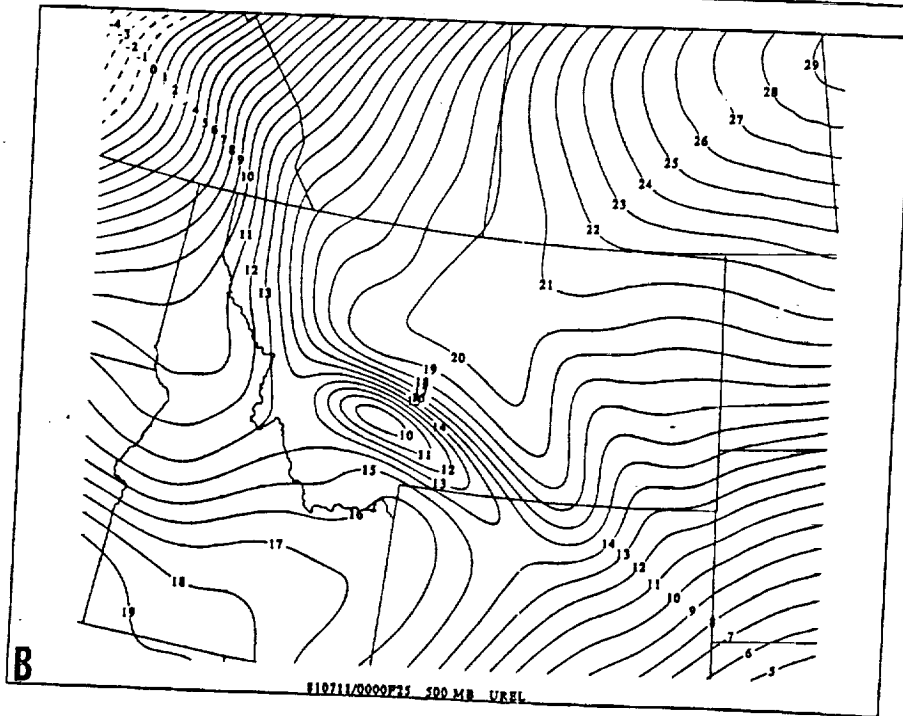
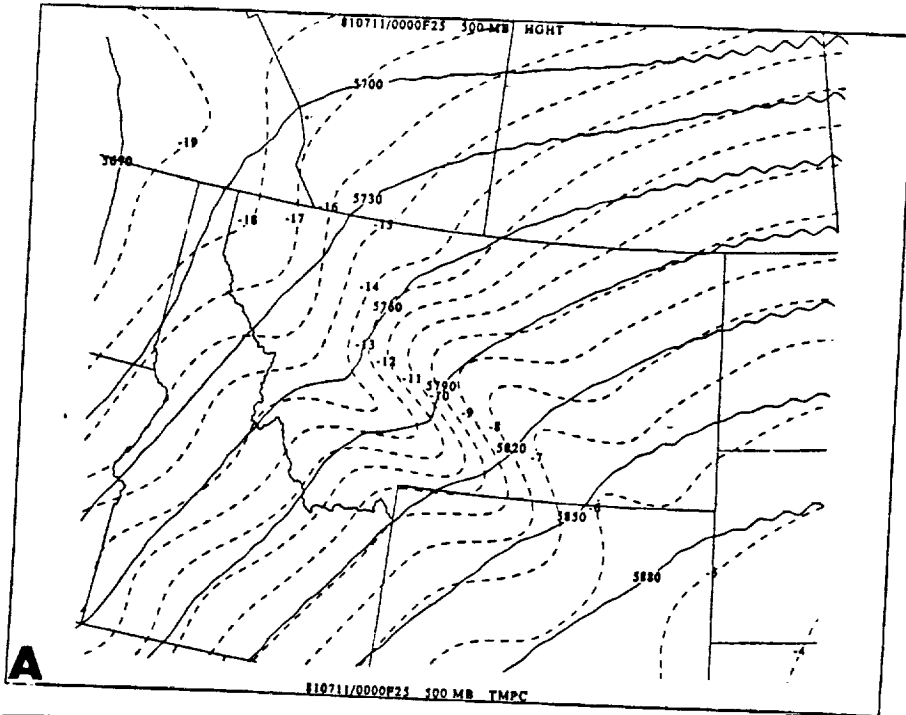
10  
||

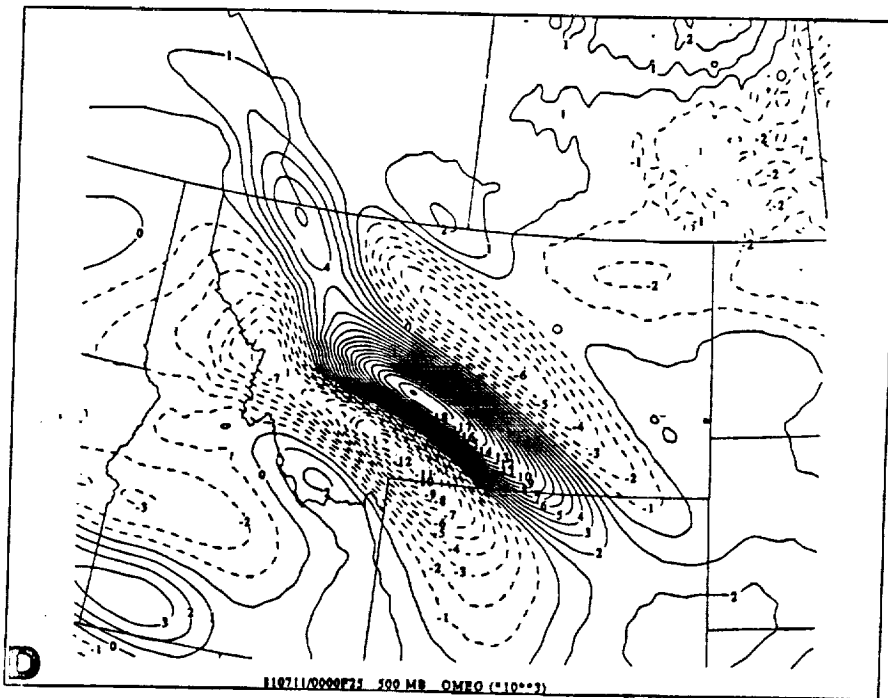
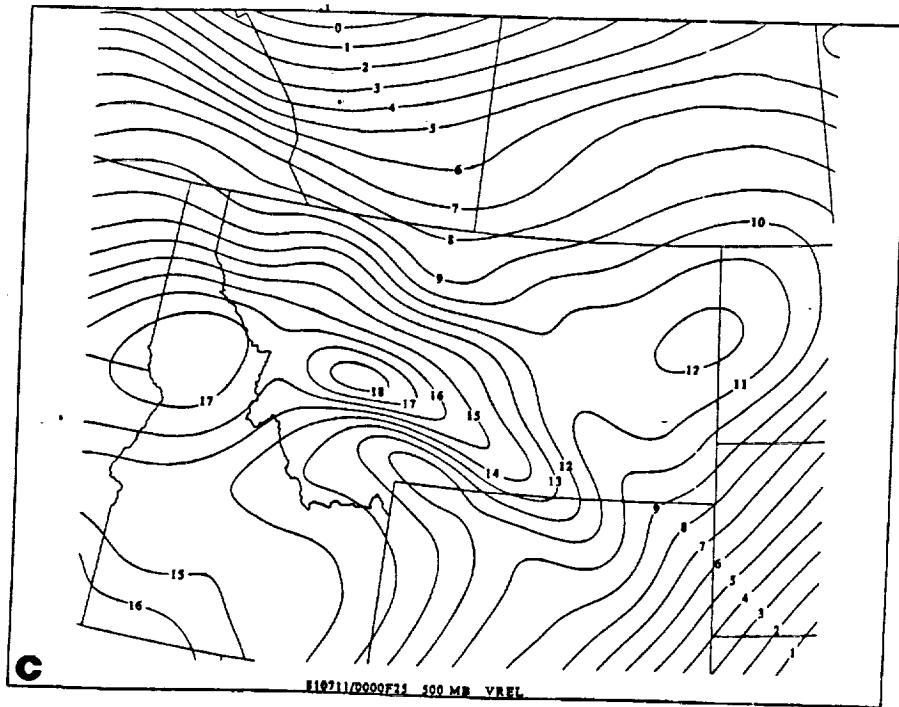


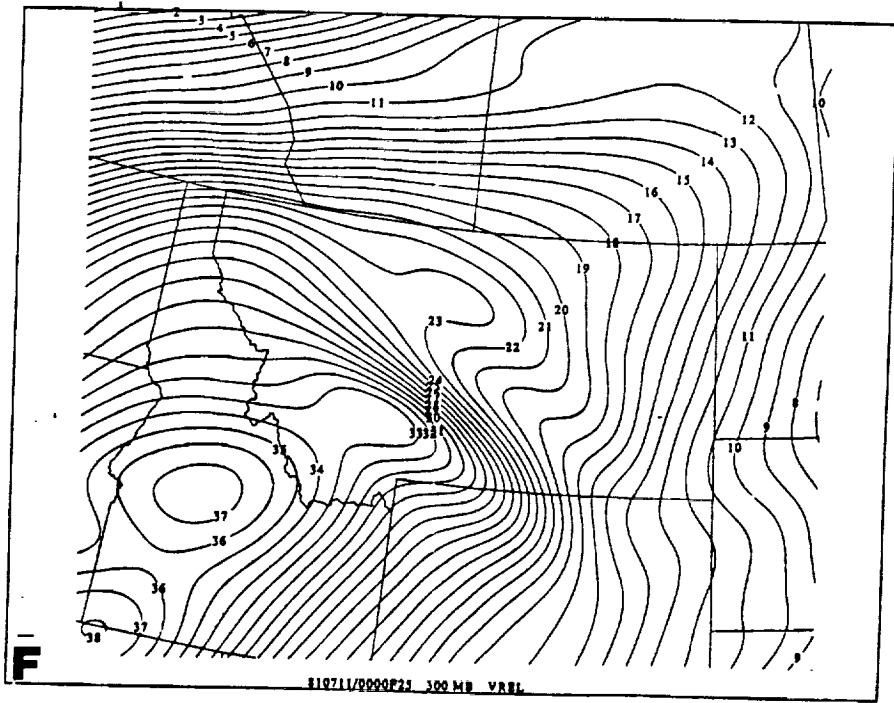
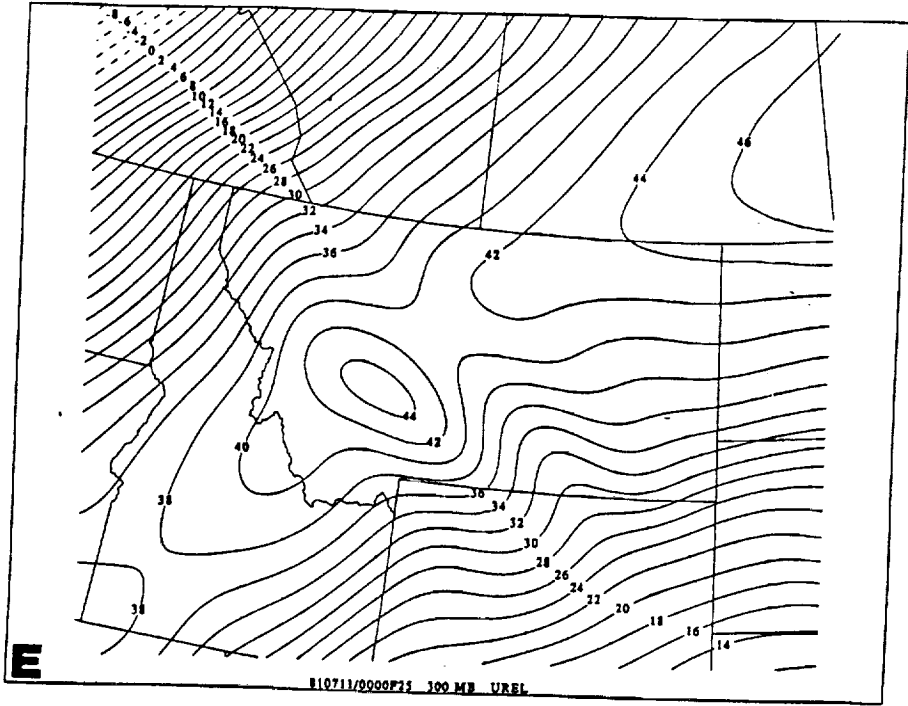


10  
 =  
 =

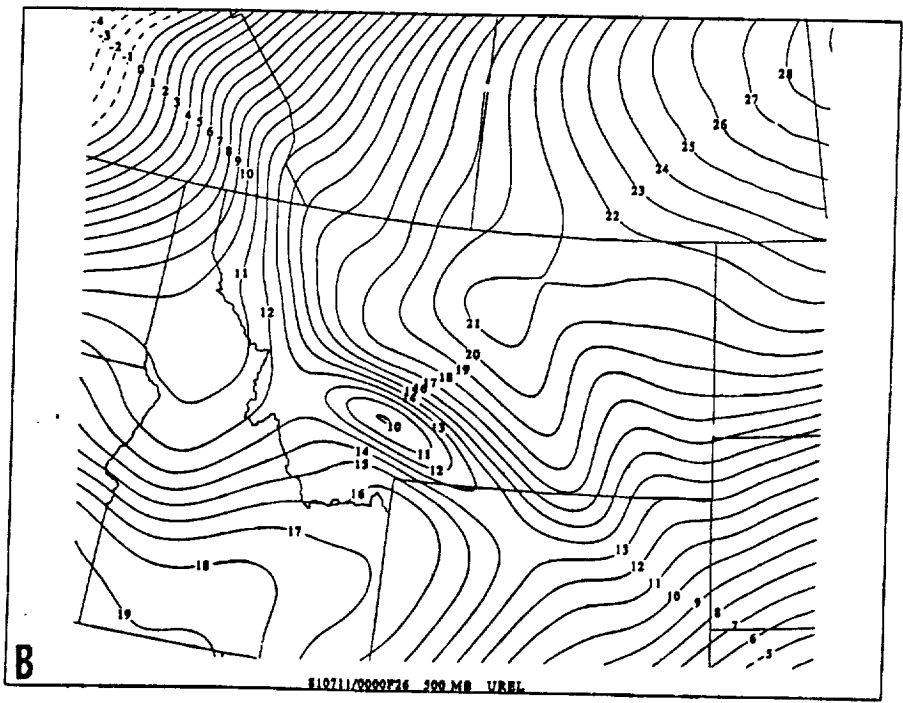
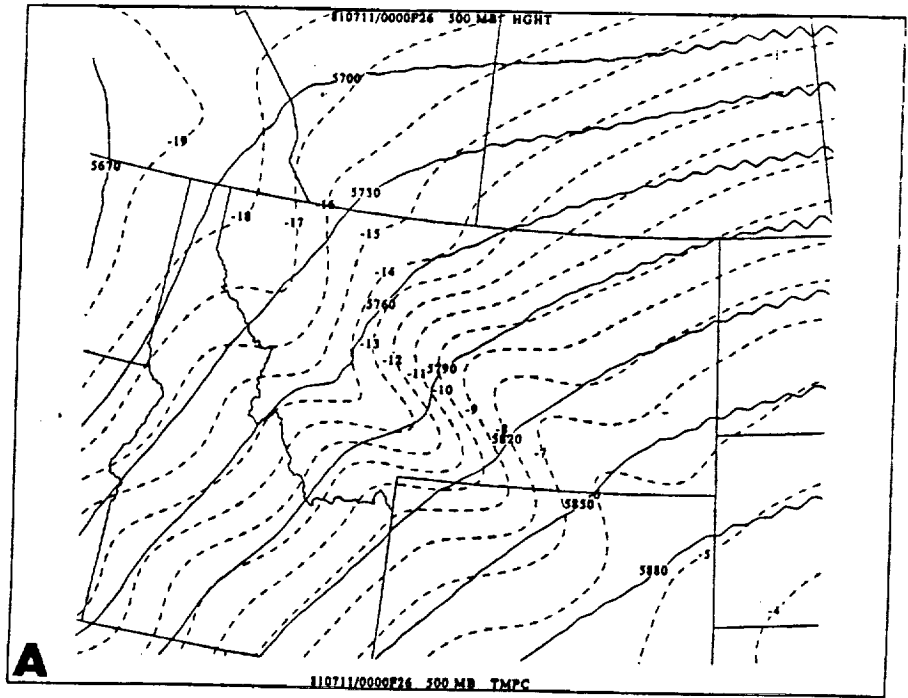


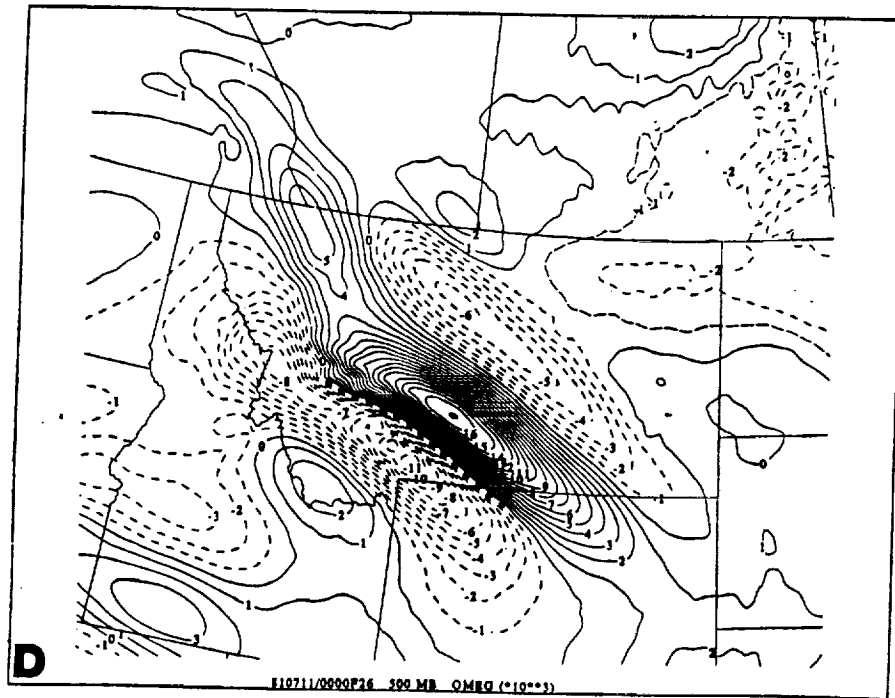
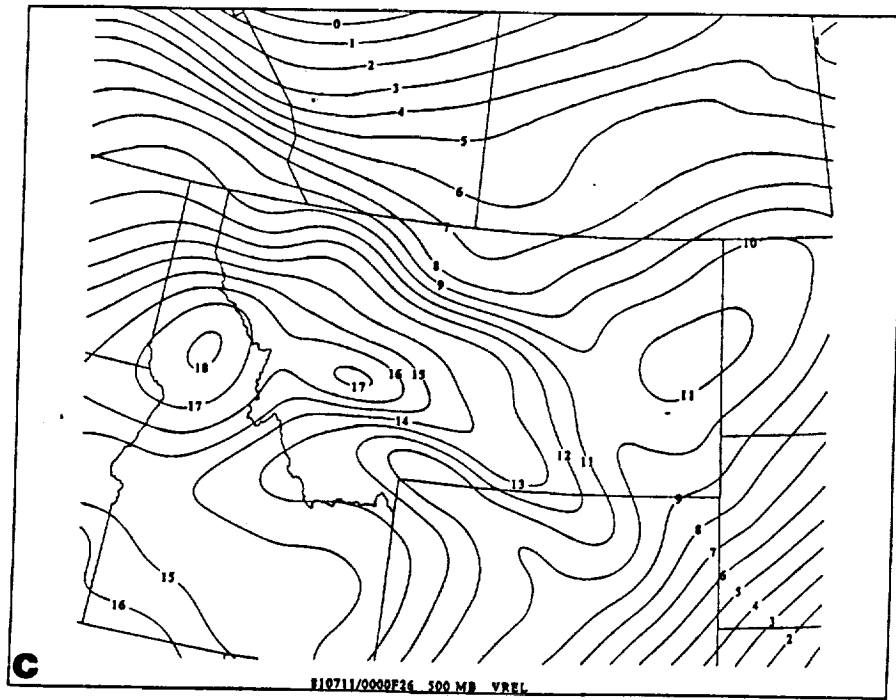


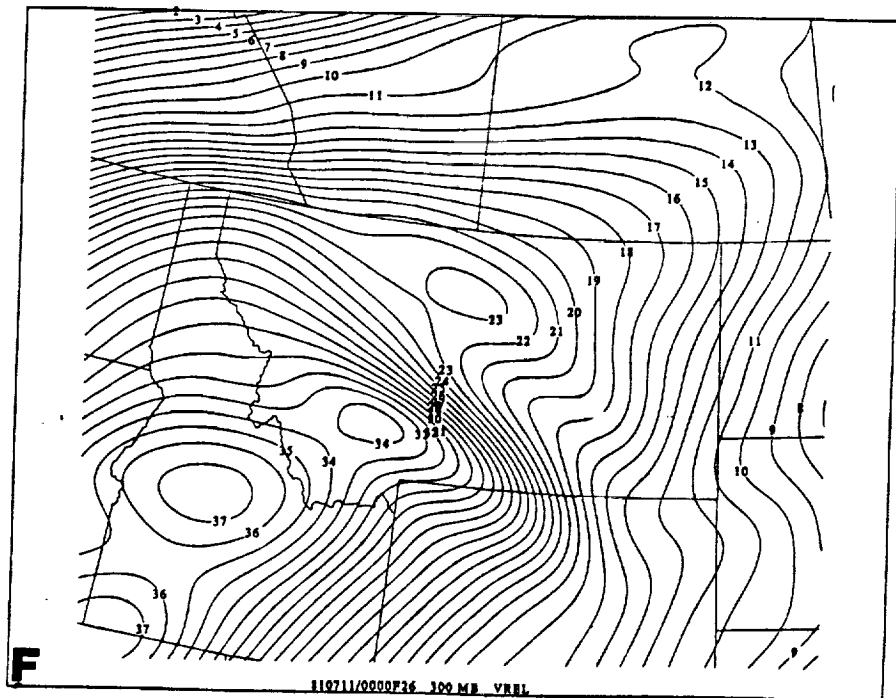
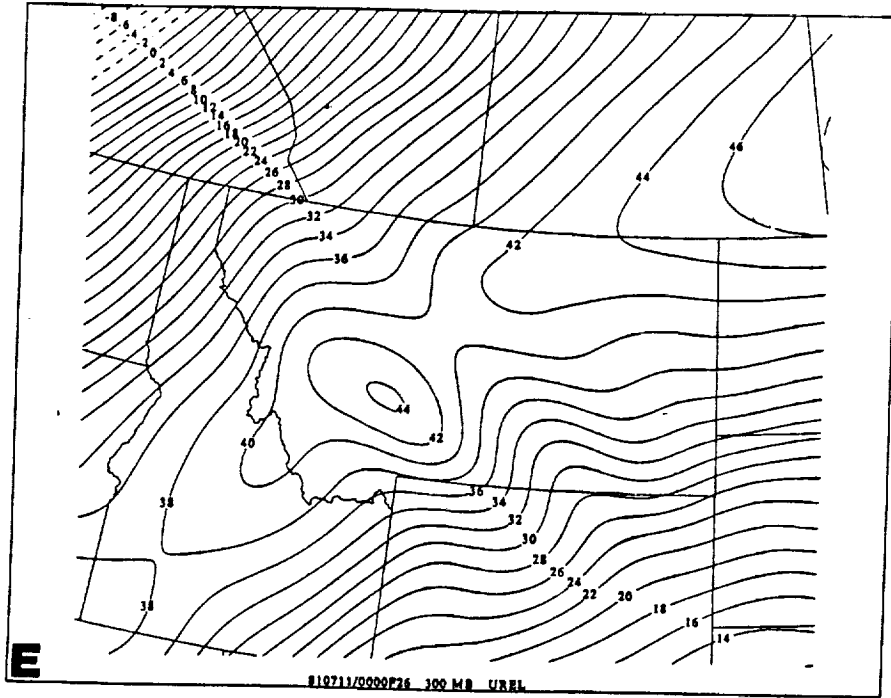


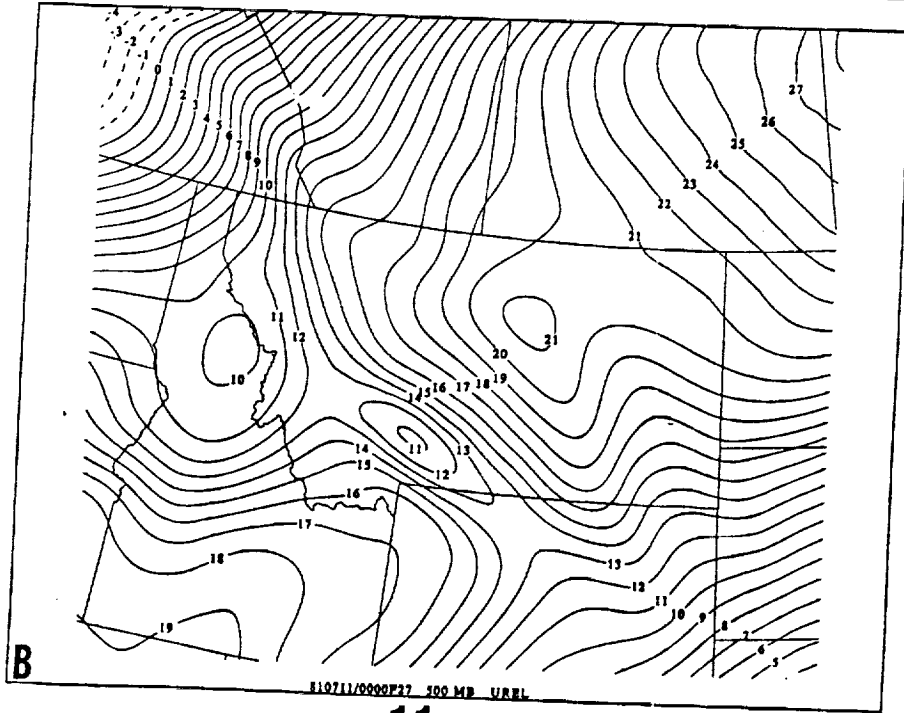
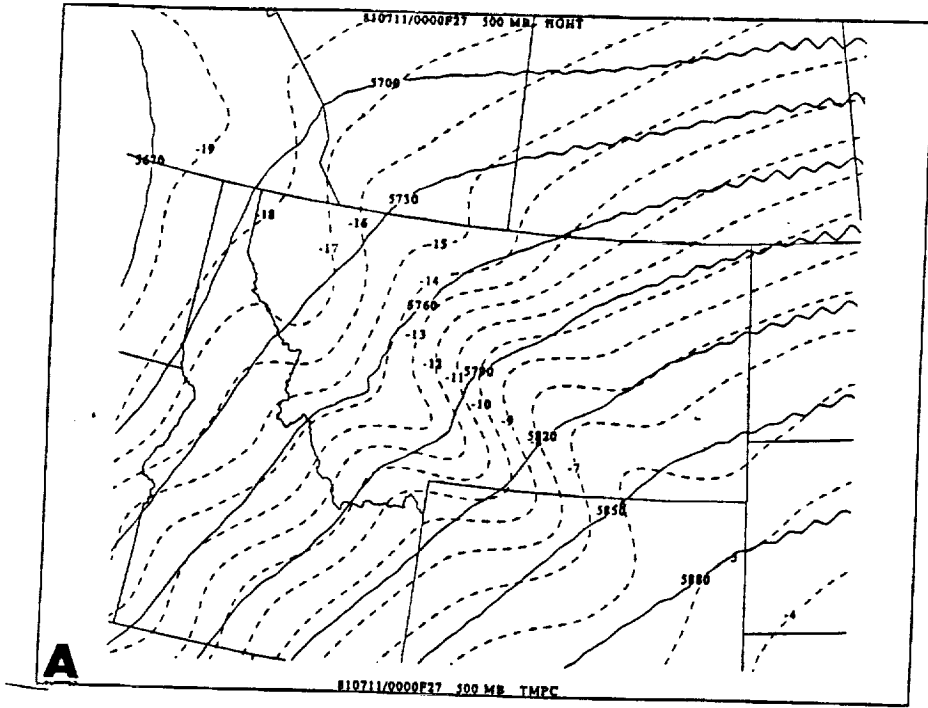


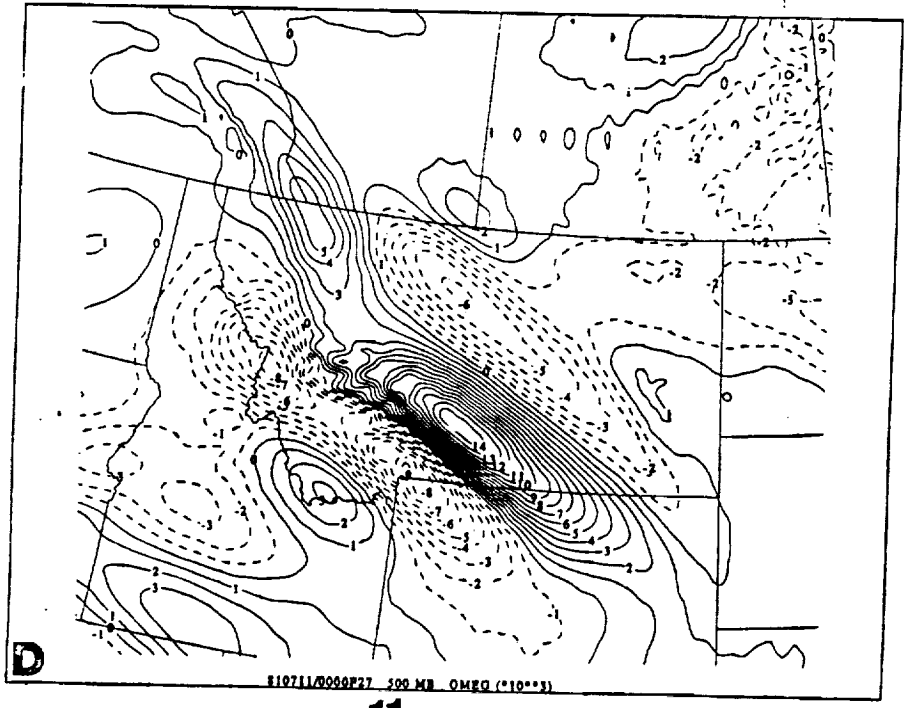
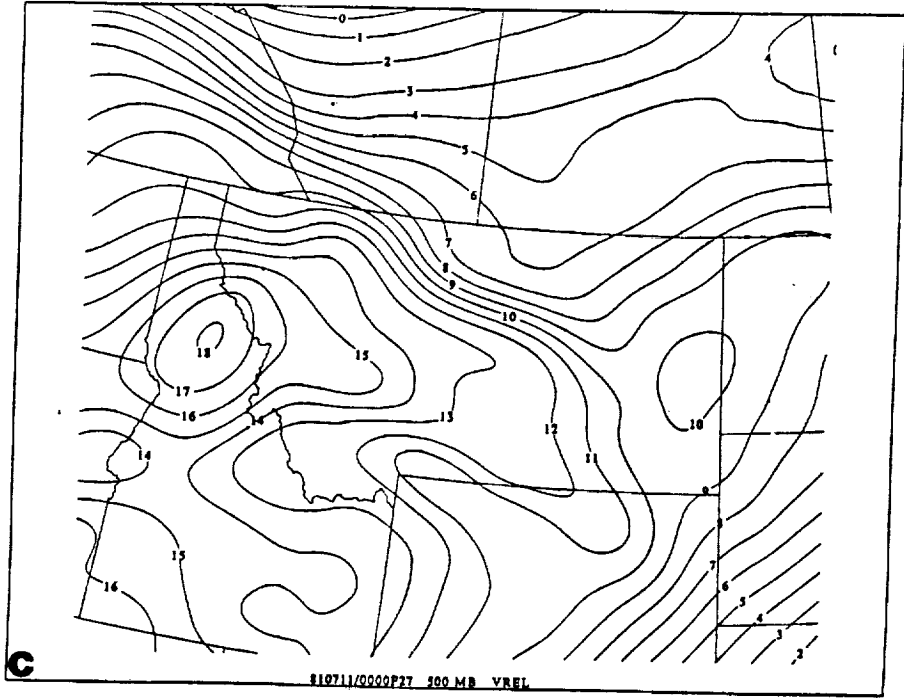


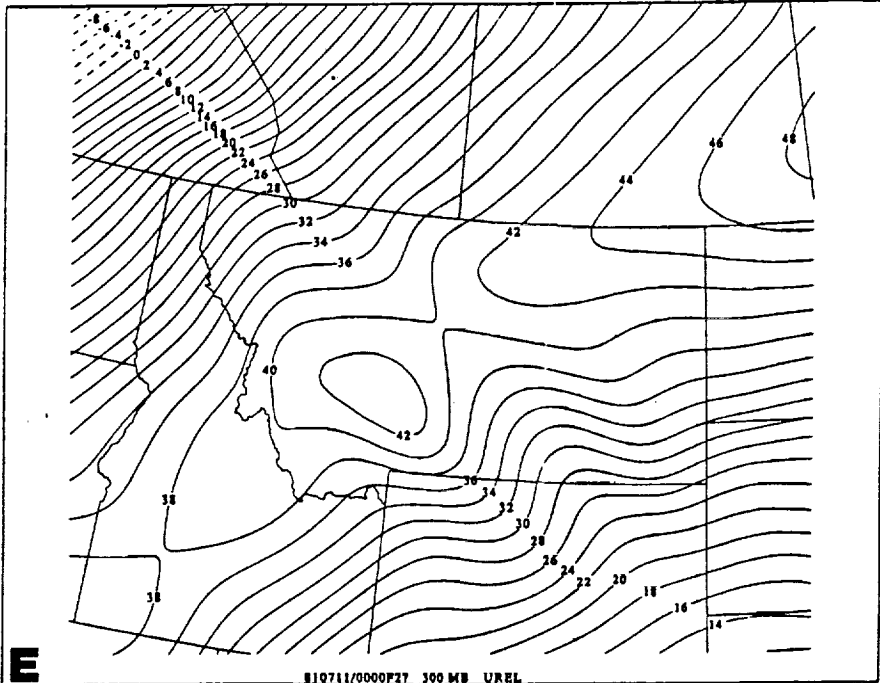




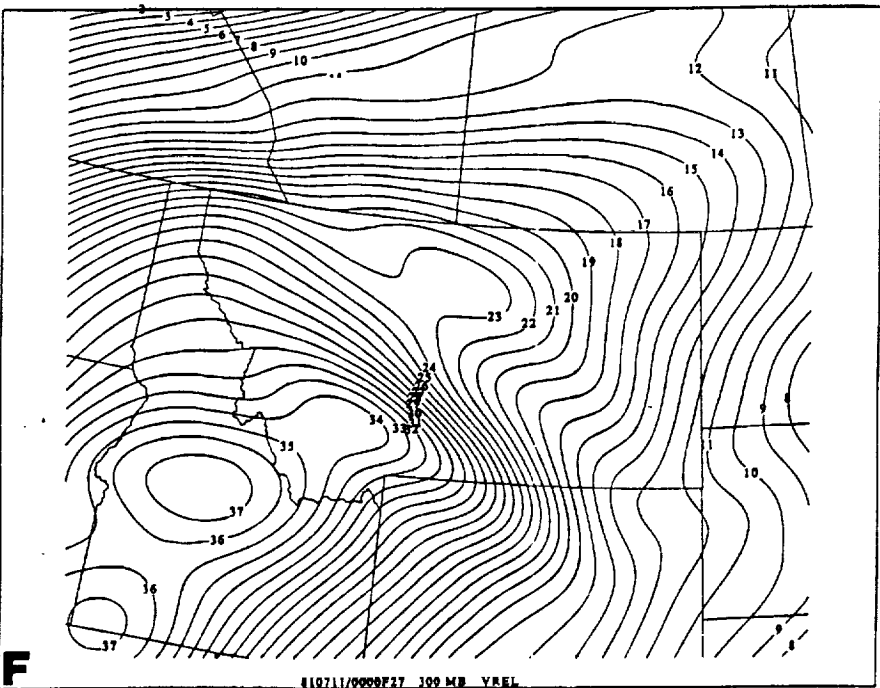








110711/0000F27 300 MB UREL



110711/0000F27 100 MB UREL